FEASIBILITY OF MORPHING AIRCRAFT PROPELLER BLADES

A Dissertation by

Johann Dorfling

Master of Science, Wichita State University, 2008

Bachelor of Science, University of Kentucky, 2007

Submitted to the Department of Aerospace Engineering
and the faculty of the Graduate School of
Wichita State University
in partial fulfillment of
the requirements for the degree of
Doctor of Philosophy

July 2014

FEASIBILITY OF MORPHING AIRCRAFT PROPELLER BLADES

The following faculty members have examined the final copy of this dissertation for form and content, and recommend that it be accepted in partial fulfillment of the requirement for the degree of Doctor of Philosophy with a major in Aerospace Engineering.

Kamran Rokhsaz, Committee Chair

Walter J. Horn, Committee Member

James E. Steck, Committee Member

L. Scott Miller, Committee Member

Ikramuddin Ahmed, Committee Member

Accepted for the College of Engineering

Royce Bowden, Dean

Accepted for the Graduate School

Abu Masud, Interim Dean

DEDICATION

To my dear wife Christin – Thank you for your constant support, encouragement, and love

Trust in the LORD with all your heart, and lean not on your own understanding;

In all your ways acknowledge Him, and He shall direct your paths.

Proverbs 3:5,6

ABSTRACT

The aim of this study is to assess the feasibility of variable geometry aircraft propeller blades, the main focus being on the aerodynamic performance. A number of objectives are established to reach this goal, with the development of an aerodynamic model and a blade optimization scheme being among these. The choice of the blade element method coupled with vortex theory and the use of calculus of variations for optimization is the result of an extensive literature review. This review also covers smart materials and their capabilities, and presents a number of structural morphing concepts. The propeller aerodynamic model is presented in detail along with the developed airfoil model and compressibility corrections. Predicted propeller performance parameters are compared with experimental data to validate the model. Both unconstrained and constrained twist optimization are considered and the derivations of the Euler-Lagrange equations are given. Unconstrained twist optimization results show that, regardless of the operating condition (takeoff, climb, or cruise), maximum efficiency occurs at lower thrust and power coefficients than required for those conditions. Constrained optimization supports this observation by showing that a constraint lowers the propeller efficiency. Twist distributions obtained from constrained optimization for the three operating conditions differ significantly but the effect on performance is insignificant. This leads to the conclusion that variable twist is not viable for a typical aircraft mission. Further analysis, however, reveals the possibility of variable twist for a loiter-dash type mission. A study of such a mission profile shows that a morphing propeller would offer a significant performance boost and is indeed feasible. Estimates of actuation power requirements show the required power to be less than the performance gain from a morphing propeller. A structural analysis of a variable camber concept shows the viability of shape memory alloys as an actuator material.

TABLE OF CONTENTS

Chapter Page

1. INTRODUCTION 1

1.1 Background 1
1.2 Research Objective 3
1.3 Document Layout 4

2. LITERATURE REVIEW 6

2.1 Introduction 6
2.2 Propeller Aerodynamics 6
2.3 Propeller Optimization 15
2.4 Smart Materials and Morphing Structures 21
2.4.1 Smart Materials 22
2.4.2 Morphing Structures 31
2.5 Chapter Summary 48

3. PROPELLER PERFORMANCE ANALYSIS 49

3.1 Introduction 49
3.2 Propeller Aerodynamic Model 49
3.2.1 Blade Element Method 49
3.2.2 Vortex Theory 55
3.2.3 Airfoil Model Description 62
3.3 Model Validation 77
3.3.1 NACA Technical Report 1309 77
3.3.2 NACA Technical Report 1375 87
3.4 Chapter Summary 91

4. PROPELLER TWIST OPTIMIZATION 93

4.1 Introduction 93
4.2 Calculus of Variations 93
4.3 Propeller Twist Optimization 97
4.3.1 Unconstrained Optimization 97
4.3.2 Constrained Optimization 99
4.3.3 Derivatives of the Performance Coefficient Integrands 101
4.3.4 Derivative of the Drag Coefficient 105
4.4 Implementation of Optimization 106
4.4.1 Method of Implementation 107
4.4.2 Validation of Method 110

TABLE OF CONTENTS (continued)

Chapter Page

4.5 Twist Optimization Results....113
4.5.1 Unconstrained Optimization Results....115
4.5.2 Constrained Optimization Results....117
4.5.3 Analysis of a Loiter-Dash Mission....122
4.6 Chapter Summary....127

5. STRUCTURAL AND POWER CONSIDERATIONS....128

5.1 Introduction....128
5.2 Structural Analysis....128
5.2.1 Entire Section Camber Morphing Analysis....129
5.2.2 Tension-Torsion Coupled Blades....137
5.3 Thermal Analysis....141
5.3.1 Method of Analysis....142
5.3.2 Results and Discussion....147
5.4 Chapter Summary....152

6. CONCLUSIONS AND FUTURE WORK....154

6.1 Conclusions....154
6.2 Future Work....157

REFERENCES....159

LIST OF TABLES

Table Page

3.1. Comparison of experimental data and XFOIL predictions 78

4.1. Comparison of problem 3 results with reference [44] 111

4.2. Definition of the propeller operating conditions 112

4.3. Unconstrained optimization results 114

4.4. Constrained optimization performance results 120

4.5. Daher-Socata TBM 850 specifications [132] 122

4.6. Definition of the Dash and Loiter operating conditions 122

4.7. Performance results of the loiter/dash mission analysis 124

5.1. Material properties 132

5.2. Comparison between analytical and finite element beam solutions 134

5.3. Published tension-torsion results 138

5.4. Morphing propeller performance comparison 151

LIST OF FIGURES

Figure Page

1.1. Fixed pitch and constant speed propeller efficiency. 2

2.1. Multi-element rib concept, from Ref. [95] 39

2.2. Actuated 14 element truss structure. From Ref. [101]. 41

2.3. Morphing trailing edge truss structure from Ref. [102] 42

2.4. Schematic of the active rib tested by Gandhi et al [103]. 43

2.5. Picture of the belt-rib prototype from Ref. [104] 44

2.6. Illustrations of chiral arrangements from Ref. [106]. 45

3.1. Front view of a two bladed propeller. 50

3.2. Schematic of the local flow 50

3.3. Axial and tangential components of induced velocity. 56

3.4. Effect of small angle approximation on α and α_i. 59

3.5. Effect of the small angle approximation on C_T, C_P, and η 60

3.6. Sketch of C_L as a function of α. 63

3.7. Experimental and modeled lift coefficient behavior. 66

3.8. Sketch of drag coefficient behavior with angle of attack. 68

3.9. Experimental and modeled drag coefficient behavior 71

3.10. Example of the drag divergence model. 73

3.11. Modeled lift coefficient behavior with Mach number. 74

3.12. Additive effect of each feature of the airfoil model. 75

3.13. Geometry of NACA 10-(10)(08)-03 propeller. 78

LIST OF FIGURES (continued)

Figure Page

3.14. Comparison of prediction with NACA TR-1309, 1140 RPM. 80

3.15. Comparison of prediction with NACA TR-1309, 1350 RPM. 83

3.16. Comparison of predictions with NACA TR-1309, 1600 RPM..... 85

3.17. Propeller geometry, NACA TR-1375. 88

3.18. Comparison of predictions with NACA TR-1375. 89

4.1. Flowchart of the solution procedure for the unconstrained problem. 108

4.2. Flowchart of the constrained problem solution procedure. 110

4.3. Chord and thickness distributions along the span. 114

4.4. Unconstrained twist distributions. 116

4.5. Plot showing the effect of λ_3 on $\beta(x)$. 118

4.6. Plot of the $\beta_{.75}$ pitch angle as a function of λ_3. 118

4.7. Constrained twist distributions. 120

4.8. Loiter and dash twist distributions. 126

5.1. Schematic of a trailing edge deflection for a twist change. 129

5.2. Desired flap angle and trailing edge displacement. 131

5.3. Propeller blade, plate, and plate cross section geometry. 132

5.4. Trailing edge displacement of flat plate..... 136

5.5. Sketch of plate geometry for heat transfer analysis. (Not to scale) 143

5.6. Altitude and SMA temperature effect on required power. 148

5.7. Freestream and SMA temperature effect on required power. 150

NOMENCLATURE

a	Speed of sound
A_f	Austenite finish temperature
A_s	Austenite start temperature
b	Inverse of $\partial C_L/\partial \alpha_i$ for the small angle approximation case
b_l	Inverse of $\partial C_L/\partial \alpha_i$
B	Number of blades
c	Chord length
C_D	Drag coefficient, $D/(½\rho V^2 cdr)$
$C_{D,\max}$	Drag coefficient at $\alpha = 90^\circ$
$C_{D,\min}$	Minimum drag coefficient
C_{Dc}	Compressible drag coefficient
C_{Di}	Incompressible drag coefficient
C_L	Lift coefficient, $L/(½\rho V^2 cdr)$
$C_{L,0}$	Lift coefficient at zero angle of attack
$C_{L,D}$	Airfoil design lift coefficient
$C_{L,\max}$	Lift coefficient at α_{stall}
$C_{L,\min CD}$	Lift coefficient coincident with the minimum drag coefficient
$C_{L,\alpha}$	Airfoil lift curve slope
C_{Lc}	Compressible lift coefficient
C_{Li}	Incompressible lift coefficient
C_P	Power coefficient, $P/\rho n^3 D^5$
C_{PL}	Power loss coefficient, $P_L/\rho n^3 D^5$

dC_{PL}	Elemental power loss coefficient
C_Q	Torque coefficient, $Q/\rho n^2 D^5$
dC_Q	Elemental torque coefficient
C_T	Thrust coefficient, $T/\rho n^2 D^4$
dC_T	Elemental thrust coefficient
D	Propeller diameter
dD	Elemental drag force
F	Prandtl tip loss factor
G	Goldstein tip loss factor
G_0	Goldstein tip loss factor based on φ_0 instead of φ
J	Advance ratio, v_∞/nD
L	Lift force
dL	Elemental lift force
M	Section relative Mach number, V/a
M_{DD}	Drag divergence Mach number
M_f	Martensite finish temperature
M_{ht}	Helical tip Mach number
M_s	Martensite start temperature
n	Propeller angular speed, rev/s
P	Power
dP	Elemental power
P_c	Power coefficient integrand

P_{Lc}	Power loss coefficient integrand
P_L	Power loss
$P_{L,D}$	Profile drag power loss
$P_{L,i}$	Induced power loss
Q	Torque
dQ	Elemental torque
Q_c	Torque coefficient integrand
r	Dimensional radial coordinate from center of propeller
dr	Dimensional differential width of a blade element
r_{hub}	Dimensional propeller hub radius
R	Propeller tip radius
RPM	Propeller angular speed, rev/min
t	Airfoil thickness
T	Thrust force
dT	Elemental thrust force
T_c	Thrust coefficient integrand
v_∞	Freestream velocity or aircraft airspeed
V	Relative velocity of a blade element
V_0	Helical speed of a blade element
w	Induced velocity
w_a	Axial component of the induced velocity
w_t	Tangential or rotational component of the induced velocity

x	Non-dimensional radial coordinate, r/R
x_{hub}	Non-dimensional hub radius

Greek Symbols

α	Angle of attack
α_i	Induced angle
α_{stall}	Stall angle of attack
α_{ZL}	Zero-lift angle of attack
β	Blade angle
$\beta_{.75}$	Blade angle at the $0.75R$ radial location
Γ	Vorticity, or circulation strength
γ	Ratio of specific heats, $\gamma = 1.4$ for air
ζ	Torque coefficient integrand multiplier (Ch.3, 4); chord-wise coordinate (Ch. 5)
η	Propeller efficiency, JC_T/C_P
κ	Airfoil technology factor in the Korn equation
μ_K	Kaplan compressibility correction to C_{Li}
μ_{PG}	Prandtl-Glauert compressibility correction
ξ	Power coefficient integrand multiplier (Ch. 3, 4); unheated length (Ch. 5)
ρ	Fluid density
σ	Solidity, $Bc/\pi r$
τ	Thrust coefficient integrand multiplier
φ	Angle between the propeller plane of rotation and V
φ_0	Helix angle of blade element

χ	Power loss coefficient integrand multiplier
ω	Propeller angular speed, rad/s

CHAPTER 1

INTRODUCTION

1.1 Background

In the design of propellers a choice has to be made as to where the design point should be. The mission of the intended application aircraft will usually define this point. A conventional aircraft, for example, spends the majority of its time in cruise and it would thus be desirable to design a propeller to have its maximum efficiency at this flight condition. But this may come at the cost of degraded takeoff or climb performance, and could potentially require a compromised solution. Perhaps an aircraft is designed for parachute operations where the propeller needs to perform well in the low-speed high-power climb configuration, or maybe the mission is one of extended periods of loitering where an efficient propeller would lengthen the loitering time. The compromise in either of these two cases may be a propeller that does not perform well at high speed cruise, or, for the loitering case, lacks sufficient takeoff thrust. The underlying point here is that once the design point is chosen, the propeller optimized for a flight condition, and the geometry established, other operating conditions may suffer from degraded propeller performance.

Before the introduction of the variable pitch propeller this design point limitation was much more severe. So much so that the Boeing model 247, an airliner introduced in 1933 and initially fitted with fixed pitch propellers, was barely able to climb to an altitude high enough to cross the Rockies [1]. The Hamilton Standard propeller company introduced a hydraulically actuated blade pitch change mechanism around the same time as the introduction of the Boeing 247. This initial variable pitch design allowed the blade angle to change between two settings: a fine pitch for takeoff, and a coarse pitch for cruise. When these propellers were mounted on the

247 its performance in takeoff, climb, and cruise was significantly enhanced. Not long after this variable pitch design was introduced, a constant speed propeller, also designed by Frank Caldwell of Hamilton Standard, appeared on the market [1]. A constant speed propeller uses engine oil as a hydraulic fluid to change the blade pitch angle, the pitch angle being controlled by a governor that attempts to keep the propeller rate of rotation constant. Constant speed propellers significantly boosted the performance of propellers and allowed them to operate efficiently over a wide range of advance ratios (advance ratio being a non-dimensional ratio between the aircraft forward speed and propeller tip speed). The success of this design is clearly visible today as the vast majority of propeller driven aircraft have constant speed propellers. Figure 1.1 is shown as a representative illustration of the performance benefit a constant speed propeller provides over a fixed pitch propeller. It can clearly be observed in this figure that the ability to vary the blade pitch angle greatly expands the operating envelope of a propeller.

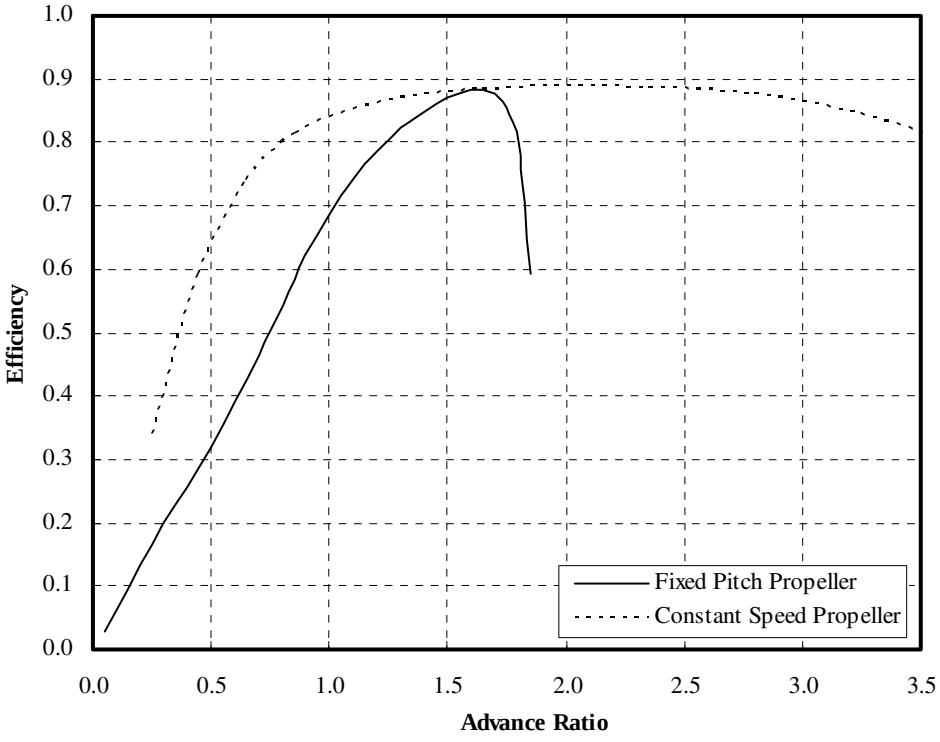

Figure 1.1. Fixed pitch and constant speed propeller efficiency.

However, when one looks at the maximum efficiency of a constant speed propeller as plotted in Figure 1.1, a peak still remains. The location of this peak is typically coincident with the advance ratio for which the propeller was designed. A cruise-optimized propeller would have its peak efficiency at the cruise advance ratio, and at any other operating condition the maximum possible efficiency would be less than this peak value. This raises the question as to whether a further refinement is possible. Would it be possible to vary the geometry of a propeller blade in flight, in addition to changing the blade pitch angle, so as to move the peak efficiency to a different advance ratio? This question leads into the purpose of the present research study.

1.2 Research Objective

This study is concerned with the concept of a variable twist propeller. For an already designed propeller its geometric parameters are fairly rigidly established, but it is conceivable that the blade twist and airfoil camber could be altered in flight. Changing the camber can be considered as a type of aerodynamic twist and, depending on the manner in which the camber is altered (i.e. trailing edge deflection), can also result in a change in the span-wise twist distribution. Thus the focus of this study is on variable twist, though both geometric twist and variable camber may be used in combination in order to obtain the desired performance gains.

The primary objective of this study is to assess the feasibility of the variable twist concept, with the main focus being on the aerodynamic performance of such a propeller. In order to satisfy this primary objective, a number of secondary objectives will be addressed in this document. These objectives are listed below.

- Develop and validate a computer program for the purpose of accurate, yet simple, propeller performance prediction.

- Optimize the twist of a propeller for a number of different flight conditions such as takeoff, climb, high speed cruise, and loiter.
- Evaluate the performance of each twist distribution obtained from optimization at flight conditions other than for which it was optimized.
- Identify the operating conditions and mission profiles where variable twist would offer an improvement in propeller efficiency as compared to a propeller blade of fixed geometry.
- Study the twist distributions obtained from optimization to assess whether the amount of required shape change could realistically be achieved through a combination of twist and camber variation.
- Perform an exploratory study into the manner by which shape change may be realized.
- Evaluate the feasibility of the use of smart materials as actuators for the purpose of shape change.
- Determine the power requirements for blade actuation in order to assess the system efficiency gains afforded by variable twist.

In meeting all the above listed objectives it is believed that it will be possible to accurately assess the feasibility of incorporating variable geometry into the design of propeller blades. The shape changing ability will give propeller designers much more flexibility in choosing the flight conditions for which to optimize a constant speed propeller.

1.3 Document Layout

In the following chapter a literature survey will be presented. This review will include discussions of past developments of propeller aerodynamic prediction methods, propeller

optimization schemes, and a review of morphing structures. In presenting the various aerodynamic prediction and blade optimization methods the goal will be to select the appropriate methods to use for analyzing and optimizing a conventional propeller. The need for an aerodynamic prediction method and an optimization approach is clear from the objectives listed above. Morphing structures are reviewed in order to find concepts introduced in the literature that may be adapted for the use of propeller blade morphing. Selection of an appropriate actuating smart material for blade actuation will also be considered.

The propeller aerodynamic prediction method chosen from the literature survey is discussed in Chapter 3 along with the details of the modeling method that was developed for predicting propeller performance. This model is validated against experimental propeller performance data. The optimization scheme is introduced in Chapter 4 and the full derivation of the method is presented. All the results from the optimization study are also presented in this chapter. The focus of Chapter 5 is on the practical aspects of a morphing propeller blade. In this chapter some of the proposed morphing concepts introduced in the literature review are evaluated, and actuation power estimates are obtained. The final chapter of the document is where the conclusions from this research study are presented. The proposed future continuation of this research is also presented in Chapter 6.

CHAPTER 2

LITERATURE REVIEW

2.1 Introduction

This chapter is devoted to a review of literature, and is broken into three main sections. The past developments in propeller aerodynamic prediction will be discussed in the first section. Different methods will be covered, their shortcomings and advantages addressed, all with the goal of selecting the appropriate performance prediction method to use in this analysis. The section thereafter will be focused on the review of propeller optimization methods with the same goal in mind of selecting the appropriate method for this present study. Past work performed in the field of morphing structures, specifically focusing on research performed on airfoil, wing, helicopter rotor blade, and propeller blade shape change is covered in the section following the optimization review. This section will also provide a brief introduction into a variety of smart materials and present their capabilities and limitations. A summary of the conclusions reached in the process of the review will be presented as a concluding section.

2.2 Propeller Aerodynamics

Modern propeller theory can be said to have initiated with the momentum analysis published by Rankine in 1865 [2] where he replaced the propeller by an actuator disk. This analysis was not complete and it also did not include any consideration of the rotation imparted to the flow by the propeller. Froude [3] considered the change in pressure across the actuator disk in 1889 whereby he completed Rankine's momentum analysis. The Rankine-Froude momentum theory of propellers is included in just about any textbook that deals with propeller theory as an introduction to the action of propellers. What this theory failed to address, in addition to its neglect of the slipstream rotation, is the geometric features of a propeller (other

than its diameter) necessary for the required thrust since it only treated a propeller as an actuator disk. In 1900 Drzewiecki [4] published a propeller theory that treated narrow strips of a propeller blade as lifting surfaces, i.e. the blade element method. This approach allowed him to place each element of the blade at an optimum angle, which he said was slightly less than three degrees angle of attack, and through this approach was able to design an "optimal" propeller. The work of Drzewiecki was the first appearance of the blade element method though he neglected to include the velocities induced at the blade elements.

Induced velocities appear to have first been included in the blade element theory by the Wright brothers in the process of designing their successful propeller. They combined momentum theory with the blade element method in order to estimate the induced velocities at the blade elements which allowed more accurate predictions of the angle of attack of each element [5]. Their method of propeller design allowed them to build propellers with impressive efficiencies, yet their work does not seem to have had any effect on later propeller theory development [6]. But still the momentum blade element theory has become perhaps one of the most commonly used methods for preliminary propeller design and analysis. This method has been in continuous use since early in the 20^{th} century and is still regularly used today. Two major considerations that the basic theory lacks are that, as already mentioned, it neglects slipstream rotation, and it does not account for any of the radial flow that causes the lift to go to zero at the blade tips. Both of these issues have been addressed over the years though. The inclusion of slipstream rotation in the momentum blade element theory has been done in one of two ways. The first is to assume the induced velocity to be perpendicular to the relative velocity of each blade element. Results from axial momentum theory applied to annular stream-tubes are then used to determine the axial component of the induced velocity at each blade element. From

the local flow geometry it is then possible to determine the angular component of the induced velocity. The induced velocity is typically assumed to be small compared to the flow velocity relative to each blade element, which leads to assuming small induced angles. This is the method described by McCormick [7]. Recently the small angle approximation of this approach has been removed [8], but this manner of including slipstream rotation is still somewhat artificial. A more exact manner of dealing with slipstream rotation is to include the conservation of angular momentum in the momentum theory analysis [9, 10]. When it comes to tip losses, the usual manner of including them in momentum theory is either to neglect the outboard 3 to 5% of the blade, or to artificially force the lift to zero at the tip. Glauert, in his comprehensive treatment of propellers published in 1935 [11], considered the radial component of momentum in order to deal with tip losses, though this method does not seem to be commonly used. In spite of the shortcomings of the momentum blade element theory, this method still gives surprisingly accurate performance prediction results [10] which is the reason for its continued regular use for propeller performance analysis.

Coming back to the historical developments of propeller theory, the next major leap after the momentum blade element theory came as a result of the lifting line theory of Prandtl. Lifting line theory showed than an ideal wing has an elliptical circulation distribution and a constant span-wise downwash. Applying this same idea to propellers, Betz [12] published a paper in 1919 (which was reprinted in 1927 [13]) that addressed the optimum induced velocity distribution of a propeller – a propeller with minimum induced losses. A wing with a constant span-wise downwash has a wake that descends behind the wing as a rigid surface (assuming a small enough circulation so that wake rollup does not occur). The equivalent of this wake behavior for a propeller wake would be a rigid helical surface. Each point along the radius of

this helical wake moves away from the propeller at an equal axial displacement velocity. Betz assumed that a propeller with such a wake would have to be lightly loaded otherwise wake rollup and slipstream contraction would occur. An approximate solution for the circulation of a propeller with a wake of constant displacement velocity was derived by Prandtl and included as an addendum to the Betz paper. This approximation of Prandtl is most accurate for low advance ratios and large blade counts, and is typically referred to as the Prandtl tip loss factor.

An exact solution to this problem was published by Goldstein in 1929 [14]. The Goldstein vortex theory is not really a method for determining the performance of a propeller, but is rather a method for determining the geometry of a propeller that would result in the ideal Betz wake. Application of Goldstein's solution to design was treated in 1930 by Lock [15]. Goldstein's tip loss factor, which is only found in tabular form, can, however, be used for the analysis of propeller performance. When this is done it is basically assumed that each individual blade element is part of a blade that is ideally shaped for the operating condition being considered [16]. Thus, away from the design condition, the induced velocities obtained from Goldstein's vortex theory are approximations. Lock, Pankhurst, and Conn used Goldstein's solution for the performance analysis of high speed aircraft propellers over a period from 1941 to 1945, all of this work being combined in a 1945 Aeronautical Research Council report [16].

The light loading assumptions of Betz, Prandtl, and Goldstein were made in order to ensure that the propeller wake would not contract. It was shown by Theodorsen in 1944 [17-20] that the light loading assumption could be removed and the wake allowed to contract. Instead of focusing on the wake immediately behind the propeller, Theodorsen considered the helical wake far downstream from the propeller and showed that Goldstein's solution for the potential field of the vortex system is still valid at this far downstream location. As in the case of Goldstein's

solution, Theodorsen's theory is also used to determine the geometry of a propeller that would produce the ideal wake with constant axial displacement velocity far downstream from the propeller. This work of Theodorsen, which also included the analysis of counter-rotating propellers, was compiled into a book published in 1948 [21].

Lifting line theory for a propeller with an ideal wake and circulation distribution had an exact solution at this point in time. Thus it was now only a matter of applying the theory to design optimum propellers. The first application of Theodorsen's theory to the problem of design was published by Crigler in 1949 [22] where he outlined a graphical design method. A simplified design approach was proposed by Larrabee in 1979 [23] where he made use of the Prandtl approximate solution, small angle approximations, and the light loading assumption. Larrabee's design procedure was refined by Adkins and Liebeck [24] by removing the light loading assumption and small angle approximation by making use of Theodorsen's solution. These methods require as input either power or thrust, the hub radius, propeller diameter, rate of rotation, freestream velocity, the number of span-wise blade elements, and the design lift coefficient of each blade element. The design procedures then give the twist and chord length of the propeller that would produce the ideal wake and thus have the smallest possible induced losses. It is also possible to invert the procedure by prescribing the chord length and then obtaining the lift coefficient of each blade element [25].

Lifting line theory is limited to blades with large aspect ratios, which is the case for most conventional propeller blades but not for the wide chord propfan blades introduced in the 1970s. Lifting line theory is also incompressible, and the only way to handle compressibility is to apply corrections to incompressible airfoil data, or to provide high speed airfoil data directly. Either way, it is an added correction that is not included in the basic theory. Another shortcoming of

lifting line theory is that the line of bound vorticity is assumed straight so that swept blades cannot be accurately analyzed. The advanced propellers introduced in the 1970s exhibited large amounts of sweep and were designed to operate with supersonic tip speeds. This, together with their wide chords, produced a need for more advanced methods of analysis. Thin wing theory adapted to propellers became a common method of analysis as it was possible to include linearized compressible flow equations in the analysis. Runyan presented such a lifting surface method for rotors and propellers based on the acceleration potential [26]. The acceleration potential method makes use of the wave equation for determining the propeller loading. The contribution of the individual blade elements to the pressure at the control point being considered are added together to determine the total pressure at that point. Since air is a compressible medium it takes a finite amount of time for a disturbance from one point to reach another, and during this time a moving object's position changes. Due to this causality principle it is thus necessary to determine the past time and location of a blade element that generated the pressure disturbance that reaches the control point at the current time. This is referred to as the retarded time approach which was the method used by Runyan. Hanson [27, 28] instead used a Fourier transformation to avoid the calculation of retarded times. Hanson did not include the finite thickness of the blades, and instead applied the no flow through condition to a reference plane as is done in thin wing theory. The finite blade hub was also neglected. Schulten in 1996 [29] introduced a lifting surface approach that included both the blade thickness, the finite hub, and the velocity displacement due to the spinner-hub assembly. Schulten's results showed a marked improvement over the results of Hanson, which showed relatively large discrepancies.

Runyan, Hanson, and Schulten all used the acceleration potential in their methods. The advantage of the acceleration potential approach over the velocity potential is that the wake need

not be considered [26]. Only the discontinuity across the lifting surface goes into the analysis. Velocity potential methods, such as the lifting line theory, need the wake to be modeled in some way. Prandtl, Goldstein, and Theodorsen considered only the ideal far-wake and managed to solve the velocity potential of such a flow. It is not uncommon to make use of the ideal rigid wake together with a velocity potential panel code, which was the approach chosen by Burger [30] and Palmiter and Katz [31]. When it comes to non-optimum wakes, two common methods for modeling the sheets are the prescribed wake model and the free-wake model [32, 33]. The prescribed wake model makes use of experimental data to model the locations of the vortex sheet and tip vortices; the ideal Betz wake can also be considered a prescribed wake. The obvious disadvantage of the prescribed wake method is that the analysis is limited to the operating condition where experimental data is available. In the free-wake models the wake is initialized to an approximate solution and is then allowed to deform with each time increment until an equilibrium, or specified tolerance between successive iterations, is reached [32].

Lifting surface methods based on either the velocity or the acceleration potential are computationally more expensive than a lifting line approach, and for conventional propellers do not seem to provide much improved performance prediction capability. Yet even more refined methods of propeller aerodynamic analysis are available in the form of numerical solutions of either the Euler or Navier-Stokes equations. Three-dimensional numerical solutions of the inviscid Euler equations applied to propellers appeared in the early 1980s [34]. The Euler equation approach removes the small perturbation assumption of the linearized potential flow equations. Thus the Euler method is able to predict nonlinear phenomena such as shockwaves that may be present in transonic flows. This capability does come at the cost of increased complexity and computer resources. Compared to full potential methods, the Euler equations are

about 3-5 times more computationally expensive to solve [33]. A further refinement comes in the form of viscous Navier-Stokes solvers. These methods are about ten times more computationally expensive than Euler methods [33], but have the capability of handling viscous phenomena such a flow separation and turbulence modeling. A great advantage of the computational fluid dynamics (CFD) solutions of propeller flow-fields is the incredible detail concerning the flow that can be obtained. This allows for in depth studies into propeller-wing interactions [35, 36], and also the flow around an aircraft fuselage in the presence of a propeller wake [37]. This detailed flow information is also used for propeller noise prediction [38, 39]. But as mentioned, CFD methods require a significant amount of computer time to obtain results, and though details concerning the flow may be obtained, the total power, thrust, and efficiency prediction may not necessarily be much better than what could be obtained from a lifting line [40] or lifting surface method. Computational fluid dynamic simulations are also plagued with a major difficulty in accurately resolving the wake of a propeller.

Accurate prediction of the propeller wake is very important as it has a strong influence on the flow at the propeller blades [31]. In order to capture enough detail concerning the wake, CFD solutions require large computational domains which add to the computational cost of solving for propeller flows. But an even bigger issue is numerical dissipation of the propeller wake structure [29, 33, 36, 41]. This problem requires that much attention be paid to the grid structure behind the propeller, and that high density grids be used. Though this reduces the dissipation, it does not remove it [36]. Another method to deal with the vortex wake dissipation is a method known as vorticity confinement [42]. The method essentially adds a force term to the Navier-Stokes equations that prevents the dissipation of vorticity. This term is defined in such way that only within the vortex wake structure will it be non-zero [33]. More recently, Wie

et al [43] published a method whereby the potential flow free-wake method was coupled to a CFD solver. The free-wake was connected to the blade trailing edge, and the flow induced by the wake was used to correct the boundary conditions on the edge of the computational domain. This method showed good results compared with experimental data of a hovering rotor, and required a smaller computational domain compared to other methods. Solutions based on the Navier-Stokes and Euler equations are very promising, but due to the computational cost involved their usefulness for conceptual and preliminary design purposes is somewhat limited.

In concluding this review, it is necessary to consider the intended application of a propeller analysis method in order to choose the appropriate technique. The purpose of the aerodynamic analysis to be performed here is to study the performance benefits that could be afforded by actively changing the twist of a conventional propeller. Overall propeller performance parameters are the desired output and not details concerning the propeller flow field. Since a conventional propeller is to be analyzed, the lifting surface approach would be unnecessary as it adds a level complexity without providing improved prediction capabilities. A CFD approach would also be superfluous as detailed flow information is not what is of interest here. Thus it is concluded that the lifting line/blade element theory is the appropriate method for this study. The wake model to be used along with the lifting line theory should also be considered, but it was shown by Gur and Rosen [10] that a free-wake model has no significant advantage over the Theodorsen theory. Accordingly, the vortex theory coupled with the blade element method is an appropriate model. The blade element method allows accurate prediction of propeller performance, and can capture changes in performance parameters due to varying blade angles. This method should thus be suitable for accurate evaluation of the effects of changes in the blade twist as well. A shortcoming of the lifting line theory is that compressibility

is not included, but this can be overcome by corrections applied to the two-dimensional airfoil data.

In Chapter 3, the blade element method will be presented in greater detail as well as its coupling with vortex theory to determine the local induced velocities along the blade. Airfoil data and compressibility corrections will also be discussed, as well as the aerodynamic model that is to be used along with an optimization method in order to determine the ideal twist distribution at different operating conditions. In the meantime, the following section is devoted to the review of past work in the field of propeller optimization and discusses the appropriate optimization tool for this study.

2.3 Propeller Optimization

Maximizing the performance of a propeller has been a concern since the inception of propellers. Drzewiecki [4] in 1900 claimed that placing blade elements at a certain angle of attack would result in an optimum propeller. Though his method lacked the inclusion of induced velocities and did not actually give optimum propellers, his contribution serves to show the desire of increasing the useful output from a propeller. Perhaps the first formal optimization of a propeller was introduced by Betz [12] who used a variational approach to arrive at the rigid wake result for minimum induced losses. The Betz wake, and the developments that stemmed from the ideal wake approach, was covered in the preceding section. The design methods outlined by Crigler [22], Larrabee [23], and Adkins and Liebeck [24] could be considered optimization methods since they are used to determine the propeller geometry that, at a specified operating condition, would have a circulation distribution which gives rise to an ideal wake. An ideal wake implies minimal induced losses and thus maximized efficiency. These approaches do not,

however, directly utilize optimization techniques but instead use the results of Goldstein and Theodorsen, who in turn used the Betz optimized wake, to arrive at a design.

A more direct optimization approach was introduced by Lock, Pankhurst, and Fowler [44] in 1942. These authors applied calculus of variations in order to determine the twist distribution that would minimize the power loss at a constant thrust. Morija [45] also presented a similar variational approach for determining the optimum twist. Compared to the methods of references [22-24], which output both the twist and chord length distributions, the method of references [44] and [45] takes the entire blade to be already designed, and then simply determines the optimum twist at a specified operating condition. The advantage of this variational approach is that the twist of an already designed propeller could be determined for a different flight condition, but this approach does require the entire propeller geometry to be already defined. Calculus of variations could also be used to determine the optimum chord-length distribution, as was done by Davidson for counter rotating propellers in 1981 [46].

Variational approaches for optimization are very effective, but may be tedious to apply as they involve determining either derivatives or integrals in the Euler-Lagrange equations. These methods are also not necessarily always the most efficient optimization tools. It is thus more common to make use of numerical optimization techniques. A large variety of methods have been developed and applied to the propeller design problem, with the choice of method for a particular optimization hinging on a number of factors, including the objective (or objectives), the number of design variables, and the constraints. Gradient based searches determine the gradient at an initial design point and then moves in the direction that decreases the objective function until a minimum along that direction is reached. A new gradient is then determined to define a new search direction towards the minimum. Shaw [47] developed a program in 1970

that used empirical data to optimize a propeller. He used a gradient based search called a pattern search technique which searches for the minimum in a direction of descent, but not necessarily in the steepest descent direction as is often done in gradient searches. Mendoza [48] also used a gradient search algorithm that was coupled with a propeller blade element code. The design variables were the blade chord, section thickness, and element angle of attack. The objective was to maximize the propeller efficiency without violating a blade bending stress constraint. A major disadvantage of the gradient techniques, especially with nonlinear problems, is the possibility of converging to a local minimum, as opposed to a globally optimized solution.

Another class of optimization schemes is known as penalty function methods where a constrained optimization problem is transformed into an unconstrained problem. The penalty function penalizes any solution that violates a constraint, and thus drives the solution towards a minimum within the design space. A penalty function optimization method was used by Chang and Sullivan [49]. They used a vortex lattice (curved lifting line) code for the propeller aerodynamics and optimized the twist distribution of a propeller in order to obtain a maximized efficiency while meeting an equality constraint for the power coefficient. It is not clear from their results what the efficiency gain due to the optimization was since they also added proplets (an addition to propeller blade tips similar to winglets) to the propeller blades. Chang and Stefko [50] used the exact same approach as Chang and Sullivan for the twist optimization of high speed propellers, except they included viscous drag, airfoil camber, and thickness in the analysis. The new twist obtained differed considerably from the baseline design and showed an efficiency increase of 1%. In these two papers (references [49, 50]) the blade twist distribution was considered as the only design variable. Cho and Lee [51] optimized both the twist and the chord length distributions by making use of penalty function methods along with a lifting line approach

for the aerodynamics. They separated the optimization problem into two sub problems, one for determining the optimum twist, the other for the optimum chord-length distribution. It is not clear, however, whether they simply optimized the twist and chord-length sequentially, one after the other, or whether there was some iteration between the two sub-problems.

In 1983, Rizk [52] introduced a numerical optimization approach, termed the single-cycle scheme. In a typical optimization procedure the design variables would be varied to move the design towards the objective. After this perturbation of the design variables, the aerodynamic tool has to be rerun to evaluate the new design. Thus the aerodynamic analysis is run for each optimization step. If the aerodynamic tool is an iterative type of flow solver, such as a potential flow solver, the computational cost can be very high due to the higher number of converged flow solutions that are necessary. What Rizk proposed was a single iterative process. After each step in the optimization routine, the design variables are updated in the flow solver and a single iteration is performed. The flow solution does not converge in this single iteration, but the flow variables from this run are fed back to the optimizer and a next step towards the optimum is made. As the design changes towards the optimum, the number of iterations of the flow solver increases so that by the end of the optimization process the flow solver would be at a converged solution using the optimized design variables. This method of Rizk was used along with a potential flow code of Jou [53] and an Euler code developed by Yamamoto [54] and proved to be significantly more efficient.

The cases discussed so far has all dealt with a single objective, typically that of maximizing the efficiency of a propeller, and for the most part only considered the aerodynamics in the analysis. But for many design cases this may not be sufficient because the propeller may have to meet certain noise constraints and the structural integrity and aeroelastic response of the

blade may also need to be taken into account. For such multidisciplinary optimizations the most common optimization approach appears to be Genetic Algorithms. This method is initialized by a population of feasible designs, and through an evolutionary process of reproduction, mutation, and crossover, the population evolves towards the desired optimum. Lee and Hajela [55] used a genetic algorithm for a multidisciplinary design optimization of a helicopter rotor blade. The disciplines considered were the aerodynamics, dynamics, and structure of the rotor blade. In a paper by Burger, Hartfield, and Burkalter [56], as well as in Burger's Ph. D dissertation [30], a genetic algorithm was used to optimize the performance of a propeller. The design variables were the number of blades, the airfoil shape (camber of a NACA 4-digit airfoil), twist distribution, chord distribution, and blade sweep. The optimization scheme was able to handle both aerodynamic and acoustic constraints, as well a being capable of performing two point optimizations (i.e. two advance ratios).

Gur and Rosen [57, 58] performed an extensive multidisciplinary design optimization of a conventional propeller wherein they considered structural, acoustic, and aerodynamic constraints. Their aerodynamic model was the simple momentum-blade element method. A genetic algorithm was only used as an initial search tool in order to get close to the global minimum. Once the solution was in the neighborhood of the global minimum, the simplex method was used to get closer to the minimum, and then finally the scheme was switched to the derivative based steepest-descent gradient search method to move the result even closer to the optimum. Their method could be applied to either minimize the noise while meeting aerodynamic and structural constraints, or to maximize efficiency subject to noise and structural constraints. Due to their choice of aerodynamic model the method of Gur and Rosen was limited

to conventional propellers, and their optimization scheme was not designed to handle multiple design points or multiple objectives.

A recent Ph. D. dissertation by Marinus [59] presented a genetic algorithm based multidisciplinary, multi-objective design optimization scheme. Three design points were considered, namely takeoff, cruise, and approach, and for each point the scheme was used to maximize the efficiency and minimize the sound pressure level all while meeting structural constraints. A Reynolds averaged Navier-Stokes (RANS) solution of the propeller flow field was used for the performance prediction and the aeroacoustic model used Farassat's Formulation 1A [60]. Since a large population made up the design space and RANS simulations are time consuming, an artificial neural network metamodel was trained to predict the performance of the different blade designs that made up the population. In order to ensure the accuracy of the neural network prediction it was progressively retrained during the optimization process using RANS simulation results of random individuals within the population [61]. Some interesting designs were obtained from this procedure which showed promising performance characteristics.

Coming now to the question of the appropriate optimization tool to use for the present study, it is again important to consider what the purpose of optimization is. The choice of optimization method hinges on the objective, the number of design variables, and the constraints. In the problem being addressed here the objective is a maximized efficiency using either a thrust or power equality constraint, and the only design variable is the twist distribution. It is assumed that a propeller will already have been designed to meet any structural constraints, and that noise is not an issue so that it need not be considered as a constraint. Accordingly, considering the methods discussed here, the candidate schemes are the calculus of variations approach or the penalty function method. These two methods are fundamentally the same and either would be

appropriate for the present study, but since Lock, Pankhurst, and Fowler [44] also used the lifting line/blade element method for aerodynamics, the calculus of variations method was chosen for the present study.

Chapter 4 contains the twist optimization of a propeller blade. In that chapter calculus of variations will be introduced and then applied to the blade element problem. Results from an optimization study will then be presented. The purpose of both the aerodynamic modeling and twist optimization is to assess the feasibility, from a performance standpoint, of a variable twist propeller. It is envisioned that such geometric morphing can be achieved through the use of smart materials embedded in the structure. Therefore, the following subsection is devoted to an introduction to these materials, their basic properties, and also the review of their past application to morphing structures.

2.4 Smart Materials and Morphing Structures

Shape change requires a means of actuation, and this actuation method needs to meet a number of constraints. Primary among these are the limitations of size and weight – size because the actuator has to fit within the geometry of the propeller blade, and weight because excessive actuator weight would generate the need for a strengthened blade structure which would result in a much heavier propeller. The deformation of the propeller blade, when actuated, should also be continuous. It is thought that smart materials embedded within the propeller blade structure could pose a viable solution to these requirements. This section of the literature review is thus devoted to a discussion of smart materials in the first subsection, followed by a review of the past application of these materials to morphing aerospace structures. By the end of this section the choice of actuation material will have been made and the review will bring to light some possible methods for achieving the desired shape change.

2.4.1 Smart Materials

The term smart material does not necessarily imply that a material possesses some form of intelligence. Instead it appears that this term resulted from what is referred to as smart material systems, or smart structures. Such smart structures have types of materials that are either mounted onto them, or embedded within them, that have the capability of performing sensory and actuating functions. With the combination of a computer processor the sensing and actuating capabilities of these materials are used to monitor and adjust the shape or characteristics of a structure to changing demands. Thus the system as a whole exhibits a type of intelligence. The actuating and sensing materials used within such smart structures or systems are what is typically referred to as smart materials. Some of these materials only have the capability of acting as sensors; an optical fiber is one such example. Other materials, such as shape memory alloys, can only be used as actuators. Piezoelectric ceramics is an example of a material capable of performing both sensing and actuating roles.

Within the context of this study, actuation from one shape to another is being considered. Thus materials that can only be used as sensors will be excluded from the discussion. Electro- and magneto-rheological fluids can have their viscosities changed by means of electrical or magnetic fields, respectively. These fluids do not, however, offer an ability of changing the shape of a structure and will also not be discussed here. The materials that are left to discuss are all solids that exhibit an induced strain response when exposed to the appropriate energy source. These materials, to be discussed in order, are piezoelectric, electrostrictive, magnetostrictive, and shape memory alloys.

Piezoelectric Materials

The piezoelectric effect was discovered by Pierre and Jacques Curie in the late 19th century when they observed that certain natural materials produced small electric fields when subjected to mechanical strains [62, 63]. Some years later the reciprocal effect of inducing a mechanical strain in response to an electric field was also demonstrated. These natural piezoelectric materials such as quartz crystals and Rochelle salt exhibited only weak electromechanical coupling and were thus not very useful as actuators or sensors. By the 1940s, synthetic piezoelectric materials were being developed with properties superior to those of quartz crystals, an example of which is barium titanate [62]. This material led to the development during the 1950s and 60s of the most commonly used piezoelectric material – lead-zirconate-titanate (PZT).

The electromechanical coupling of piezoelectric materials is due to the electrical polarization of individual crystal structures within the material. That is, each crystal within the material has a polar axis along which an electric dipole exists. When the material undergoes deformation, the orientation of the polar axis of each crystal also changes. This realignment of the polar axes results in a net charge that can be measured across the faces of the material [62]. Conversely, when an electric field is applied to these materials it causes the dipoles within the crystals to rotate so as to be more aligned with this field. The result of this domain structure change is a net strain of the material [63].

When a piezoelectric material is first manufactured it exhibits relatively weak electromechanical coupling because the electric dipoles point in random directions [62]. In order to improve this property of the material the dipoles need to be oriented in the same direction. This is done by first heating the material to beyond its Curie temperature. The Curie point, or

Curie temperature, is a characteristic temperature of a material where its magnetic properties changes drastically. Below the Curie point the magnetic domains of a permanent magnet are all aligned, but above the Curie point the domain directions become random and susceptible to magnetic induction by an external magnetic field. The same is also true for the electrical dipoles. Once the material is heated to above its Curie temperature, the dipoles can be re-oriented by applying a strong electrical field to the material. The material is then cooled to below its Curie point and the electrical field is removed. Below the Curie temperature the dipole orientations of the individual crystals become locked in the poling direction of the electric field, and the piezoelectric properties are much stronger [62-64]. A number of different PZT formulations exist and each has a different Curie temperature, but typically this point falls within the temperature range from 200 ºC to 350 ºC [63].

Piezoelectric materials can be used in both sensing and actuating functions. As an actuator PZT is capable of induced strains of about 0.1% at electrical fields in the range of 1000 V/mm [64]. At low excitation levels (about 200 V/mm) PZT exhibits a linear strain response to the applied electric field and not a significant amount of hysteresis [65]. Larger electric fields do, however, cause an increasingly hysteric response [64]. Piezoelectric materials respond rapidly to applied electric fields and it is thus possible to use these actuators for high frequency applications [65], but the frequency may be limited by the high electrical fields needed for actuation [64]. The response of PZT to electric fields is relatively insensitive to changes in temperature, but the performance does degrade as the temperature increases towards the Curie point. The Curie temperature of any piezoelectric material is a critical parameter since, as already mentioned, total depoling results if the temperature exceeds this value [64]. Once the material is depoled its electromechanical coupling is significantly weakened. Excessive

electrical field strengths and repeated cycling of large fields can also cause depoling. An advantage of piezoelectric ceramics is that they are manufactured by pressing and firing a powder which means that a large variety of shapes are possible. But at the same time, being a ceramic, this material is brittle and has poor tensile strength [65].

Electrostrictive Materials

Electrostriction is a phenomenon that occurs in dielectric (insulating) materials when exposed the an electric field [65]. The field induces charges within the material that attract one another resulting in a net compressive force [64]. For most dielectric materials the effect is insignificantly small, but for a class of materials known as relaxor ferroelectrics the electrostriction effect produces strains of around 0.1% [64, 65]. Applied electric field strengths required for such strains are the same as for piezo-ceramics [63]. Two common electrostrictive materials are lead-manganese-niobate (PMN) and lead-manganese-niobate enriched with lead-titanate (PMN-PT) [63, 65]. The response of electrostrictive materials to electric fields is nonlinear, typically modeled by a quadratic, but has much less hysteresis than piezoelectric materials. Electrostrictive materials are only capable of one way actuation whereas a piezoelectric material can produce both positive and negative strains with electric field reversal; an extensional strain can be achieved in electrostrictives, however, due to the Poisson effect if the electric field is applied in the transverse direction. An advantage of electrostrictives over piezoelectrics is that they are not polarized and thus their response properties cannot decay like it can for piezoelectrics [65]. On the other hand, electrostrictive materials are more temperature dependent and should ideally operate slightly above the Curie temperature [64, 65]. Electrostrictives such as PMN are also a ceramic manufactured by a similar process as a piezo-

ceramic, thus this material also offers a large variety of possible shapes. These materials also offer a wide frequency bandwidth for actuation.

Magnetostrictive Materials

Magnetostriction is a very similar phenomenon to electrostriction, but the field that drives this effect is magnetic instead of electric and the field causes the material to expand rather than contract [63, 65]. At the crystal structure level the domains possess a magnetic bias which, for a rod, is approximately perpendicular to the longitudinal axis. Applying a magnetic field causes these domains to rotate so as to align with the magnetic field lines resulting in a net expansion along the longitudinal axis [65]. Compressively pre-stressing the material causes more of the domains to be oriented perpendicular to the longitudinal axis resulting in larger possible strains.

The most commonly used magnetostrictive material is a compound known as Terfenol-D, the name being derived from the metals that compose this material as well as the lab in which it was developed: terbium (Ter), iron (Fe), Naval Ordinance Laboratory (NOL), and dysprosium (D). The strain response of this material due to a magnetic field is nonlinear and also significantly hysteretic. Strains up to about 0.17% are possible at a magnetic field strength of around 240 A/mm with a compressive pre-stress of about 27 MPa [66]. This material is capable of greater strains than either PMN or PZT and can also exert large forces, comparable in magnitude to that of much larger electromagnetic shakers. Magnetostrictives also have their drawbacks. Primary among these are the fact that for these materials to be used as actuators they have to be combined with an electromagnetic energizing coil [63]. This considerably increases the size and weight of such actuators as compared to an electrostrictive or piezoelectric actuator which, at a minimum, only needs to be connected to two electrodes to act as an actuator. Terfenol-D is also expensive as compared to piezoelectric and electrostrictive materials since the

rare earth elements that comprise this material are costly [64]. Terfenol-D is also limited in its available sizes and shapes which limits its application.

Shape Memory Alloys

A shape memory alloy (SMA) is a type of metal alloy that is characterized by its ability to sustain large amounts of strain without permanent plastic deformation. Recovery from strains of up to 8% is made possible by a metallurgical phase transformation within the material. The two phases are known as martensite and austenite, and it is the temperature and stress dependent transformation between these two phases that gives SMA its shape memory and pseudoelastic properties. In order to elucidate the behavior of SMAs the two phase transformation drivers (temperature and stress) will be discussed separately, and in doing so, both the shape memory and pseudoelastic effect will be described. In either case, however, the discussion will start with assuming the material to be in the high-temperature austenite phase and in an unloaded state. The material's memory state exists in the austenite phase, the memory shape being imposed through the process of annealing.

When the unloaded austenite is cooled, a phase transformation to the martensite phase begins upon reaching the martensite start temperature, M_s, and full transformation is realized upon reaching the martensite finish temperature, M_f. The martensite start temperature is higher than the martensite finish temperature ($M_s > M_f$), and the exact values of these two temperatures depend on the chemical composition of the particular alloy. The crystallographic structure of the martensite is known as a twin-related variant. The metal in this phase exhibits a linear stress-strain relationship up to a critical stress, beyond which detwinning of the crystal structure starts to take place with increasing loads. Large strains result from small increases in stress and the deformation appears to be plastic. This plastic-like deformation continues up to a point where

the martensite is fully detwinned, resulting in a single variant crystal structure that is aligned with the stress direction. If the material is unloaded at any point during the detwinning process some residual strain will remain, but this residual strain is fully recoverable by heating the material. Transition back to the austenite phase starts at the austenite start temperature, A_s. This point is typically higher than the martensite start temperature. Upon reaching the austenite finish temperature, A_f, the SMA is again fully austenite. During this phase transformation process the material reverts back to its memory shape and recovers the residual strain. This process describes the shape memory effect of SMA.

Phase transformation to martensite is also possible without any change in temperature. Consider the case when the temperature is maintained above the austenite finish temperature, and a load is applied to the material. At first the austenite exhibits a linear stress-strain relationship with an elastic modulus that is significantly higher than the elastic modulus of the martensite. Again at some critical stress point, different from the low-temperature critical stress, large deformations are observed with only slight increases in stress. The plastic-like behavior observed in this case is due to the material transforming into the single variant martensite phase. Unloading at any point during the phase transformation shows a linear reduction of strain initially. At some intermediate stress point the material will start to transition back into the austenite state. Large amounts of strain are recovered with small reductions in the applied load, and once the material is completely unloaded the memory shape is regained. This behavior illustrates the pseudoelastic property.

With the behavior described some of the mechanical and actuation properties of SMA materials need to be discussed. Perhaps the most commonly used shape memory alloy is a combination of nickel and titanium known as Nitinol, and the properties discussed here relates to

this material. Nitinol was also developed in the Naval Ordinance Laboratory and the name is thus due to a similar naming convention as used for Terfenol-D. It has already been mentioned that the Young's modulus of a SMA in the austenite phase is higher than in the martensite phase. The degree of change is considerable, and for Nitinol the elastic modulus changes from roughly 28-41 GPa in the martensite phase to about 83 GPa for the austenite phase [67]. The range of possible transformation temperatures span from –200 ºC to 110 ºC depending on the exact chemical composition. Excess nickel in the alloy, or the addition of iron or chromium, depresses the phase transformation temperatures. It was also illustrated earlier that the martensite-to-austenite transformation starts during heating at a higher temperature than the reverse process during cooling. This temperature hysteresis is typically on the order of about 30 ºC, but this can be reduce to around 10-15 ºC by the addition of copper to the alloy.

When it comes to actuation, strains of up to 8% are recoverable with recovery stresses of up to 700 MPa being possible. The strain capability of SMA is more than an order of magnitude greater than the other three smart materials discussed. This major advantage comes with some disadvantages as well. Due to the fact that SMAs are thermally actuated, their response times are slow and limited to actuation frequencies of a few hertz at most. Shape memory alloys also have a large amount of hysteresis in their heating and cooling cycles, and their responses are also highly nonlinear. Conversion of thermal energy into actuation work by these materials is also a very inefficient process, giving the SMA actuator an efficiency of about 10% [64]. An additional drawback is that the shape memory effect is generally a one-way process so that the material has to be forced back into a strained shape upon cooling and returning to the martensite phase. It is possible, though, by means of thermomechanical training, for these materials to exhibit a two-way shape memory effect, but during the reverse process only small stresses can be

exerted with much smaller strains than the one-way process [63, 67]. Thermal actuation, though being considered here as a disadvantage, does offer flexibility in the choice of heating method: electrical Joule heating, hot water, hot air, and perhaps even solar or environmental. Thus depending on the application, the activation energy source could be varied.

Perhaps the most appropriate application of a shape memory actuator, based on the mentioned advantages and disadvantages, is in the case where a one-way shape change, from one discrete shape to another, is desired. Controlling these actuators to intermediate shapes is complicated by their nonlinear response. Two-way shape change is another viable application as long as the base structure being actuated is stiff enough to return to its original shape without actuation, and upon return to this shape, exert enough force to strain the martensite.

Considering the properties of the materials discussed here it appears that shape memory alloys are the appropriate choice of actuator for changing the shape of a propeller blade. The main reason for choosing this material actuator is its large strain capability because it will likely be capable of providing the desired shape change without the need for a displacement amplification mechanism. Such a mechanism would likely be necessary for the other types of actuator materials leading to a weight increase. The second reason comes from considering the intended function of the material. It is desired to be able to change the shape of the propeller blade between two states. Shape memory alloys fit this role well as the structure could be manufactured into one of the desired shapes and then actuated to another. Upon cooling of the SMA the stiffness of the structure would cause it to revert back to the manufactured shape. The rate of actuation required is not high, and shape change only needs to occur within the time it takes the aircraft to change from one flight condition to another. Thus a high frequency actuator is not necessary, and the slow response of SMA will not be a problem. The last feature of SMA

that makes it a viable actuator material is the capability of embedding it within the blade structure. Shape memory wires or ribbons could be placed in between layers of composite laminates thus becoming part of the structure being actuated.

Evaluation of SMA as an actuator is presented in Chapter 5 in order to verify that the strain capability of this material is sufficient for the desired shape change. With the actuator material selected, discussion of shape changing structures will now proceed in the following subsection.

2.4.2 Morphing Structures

This section of the review is concerned with morphing structures. It was concluded in the preceding subsection that shape memory alloys are a viable material for shape actuation of a propeller blade. Accordingly, focus will be on previous work and concepts where SMA was also chosen as the actuating material, but the discussion will not be limited to SMA applications only. It may be possible to apply SMA to shape morphing concepts where other actuators were used. The geometric variables of a propeller considered for shape change are section camber and blade twist. Thus past work that involved other shape variables will be excluded from the review.

Very little past work was concerned with propeller morphing, with the majority of research focusing on two-dimensional airfoil sections, fixed wings, helicopter rotor blades, or wind-turbine blades. Only a single author was found to have considered changing the camber of a marine propeller, but the focus was primarily on the actuating materials, rather than on the mechanism by which to achieve the shape change [68, 69]. Some patents have been awarded for concepts that propose changing the camber of propeller blades in flight. The first of these patents [70], awarded in 1932, placed a trailing edge flap along the entire span of a fixed pitch propeller blade. The angle of the flap would be controlled by the pilot by means of mechanical

linkages that moved a control horn at the propeller hub. A similar type of trailing edge flap patent was awarded in 1965 [71], but in this case it would be applied to a variable pitch propeller with a more sophisticated mechanism employed for varying the flap angle. It is not known whether either of these two concepts flew on an aircraft. Another variable camber patent that did go into flight testing made use of two blade rows with the two blades spaced closely together so as to make a two element airfoil [72]. The pitch angle of the two blades would change in a way that would result in a change in the camber of the two element airfoil.

Since there are so few propeller morphing applications, the remainder of what is covered here concerns the other applications. These other applications could of course be adapted to a propeller blade. Twist change of wings and rotor blades will be covered first, followed by a presentation of the concepts proposed and tested to achieve airfoil and wing camber variation.

Variable Twist

Various morphing concepts have been proposed in the literature for varying wing or rotor twist. These different methods are grouped into four categories: integral twist actuation, trailing edge flap methods, tension-torsion coupling approaches, and spar modifications.

In the integral twist actuation method actuators are typically embedded within either the upper and lower skins, or the upper and lower parts of the main spar, oriented at 45 degrees relative to the span-wise axis. Upon actuation the actuators either contract or expand causing a torsional moment that twists the structure. Chen and Chopra [73] did exactly this by placing piezoelectric actuators on the inside of the upper skin of a rotor blade at 45 degrees, and on the lower skin placed the actuators at −45 degrees. In hover tests their scaled 6 ft diameter rotor achieved about half a degree twist change for most actuation frequencies, and close to one degree twist change when actuated at the torsional natural frequency of the blade (~5/rev at 900 rpm).

Generally the objective of rotor blade twist control is for vibration reduction, thus high frequency excitation is needed and twist changes of only about two degrees is required. For these reasons piezoelectric actuators are typically used.

A piezoelectric actuator configuration known as an active fiber composite was developed to improve the performance of the integral twist actuation concept. This actuator is easily embedded in a composite laminate structure as one of the plies in the layup. The active piezoelectric fibers can be oriented at any desired angle. Rogers, Hagood and Weems [74] embedded the active fiber composite sheets in the upper and lower laminates of the leading edge D-spar of a rotor blade at both plus and minus 45 degrees. Static tests of the rotor blade showed twist angles of 0.77 degrees/m. A similar design that also made use of active fiber composites, known as the NASA/ARMY/MIT Active Twist Rotor, was predicted to produce twist angles of around two degrees [75, 76]. Static tests of a 55 inch radius active twist rotor blade exhibited about one degree peak-to-peak excitation [77]. This same actuation concept was also seen in a paper by Park et al. [78] where they considered changing the twist in tilt-rotor blades, but instead made use of SMA wires oriented at 45 degrees relative to the longitudinal axis. Shape memory alloy was considered since these authors only sought twist variations from the high-twist hover state to the low twist airplane state.

In another variable twist concept, that fits within the integral twist actuation category yet very different from the above mentioned approaches, the skin of a rotor is warped by using a round threaded spar [79]. This spar is located near the trailing edge and attached to the lower blade surface by unthreaded sleeves and attached to the upper surface by means of threaded sleeves. Rotating the threaded spar causes the upper surfaces to move span-wise relative to the lower surface, warping the skin as a result. This induces a torsional moment in the blade and

causes it to twist. Another warping concept proposed by Mistry, Gandhi, and Chandra [80] involved applying Vlasov bi-moments to the ends of an I-beam to induce twist warping. The bi-moment force arrangement applies, for example, compressive forces to the left end of the upper flange and the right end of the lower flange, and tension forces to the left end of the lower flange and right end of the upper flange. This article contained only the results from a numerical and analytical investigation and suggested that a 62 inch long I-beam could be twisted by up to six degrees with 200 lb forces applied.

The next active twist category makes use of trailing edge flaps to twist a rotor blade. Deflection of the flap produces an aerodynamic moment about the elastic axis of the blade causing it to twist. Alternatively, the flap could also be used to control the lift on the blade by effectively increasing or decreasing the camber over the section of span where the flap is located. Though not considered to be a viable method for changing the twist in a propeller blade, the flaps are mostly actuated by smart materials and thus the reason for covering this twist actuation category. Trailing edge flaps could also be used to vary the camber of an airfoil. Ben-Zeev and Chopra [81] presented a trailing edge flap concept driven by a piezo-ceramic bimorph actuator. This is a type of bending actuator where a piezo-ceramic strip is bonded to either side of a thin brass shim. Applying equal but opposite electric fields to the piezo strips causes the actuator to bend. Straub [82] introduced a piezoelectric driven actuator tube concept for the control of a trailing edge flap. This actuator tube had piezoelectric strips placed circumferentially and along the length of the tube at plus/minus 45 degrees relative to the longitudinal axis. Actuation would cause the tube to twist, and with one end of the tube fixed to the blade and the other to the trailing edge flap would result in a deflection of the trailing edge flap.

Straub et al. [83] published a paper in which it was proposed to use two trailing edge flaps, one for the purpose of vibration reduction and the other for in-flight blade tracking. Vibration control would need a high frequency actuator, thus a linear piezoelectric stack actuator combined with an angular displacement amplification mechanism was proposed. In-flight blade tracking, on the other hand, did not require high frequency actuation so an actuator that made use of SMA torsion rods was developed. Two torsion rods were configured in an antagonistic arrangement, along with a braking mechanism so that the flap could be held in a set position without the need for further heating. An alternate trailing edge flap actuation concept that also made use of two actuators operating antagonistically was presented by Woods et al. [84]. The actuators used in this case were pneumatic artificial muscles.

A blade vibration control concept very closely related to the trailing edge flap is to adjust the angle of only the outboard section of the rotor blade. Bernhard and Chopra [85] introduced such a concept where the outboard 10% of the rotor would be separated from the rest of the blade so that its angle could be varied. The proposed mechanism for achieving these angle changes was to make use of a tension-torsion coupled composite beam placed inside the box spar of the main blade section. At one end this beam would be attached to the blade root and at the other end to the active tip. The fiber layup of the actuator beam was varied from one section to the next: one section had the fibers of the laminates oriented 45 degrees from the longitudinal axis, and the next section had the fibers oriented at −45 degrees. Piezoelectric elements were bonded to both the top and bottom surfaces of the beam, with the actuation direction aligned with the span-wise axis. In one section the actuators were actuated to cause bending in one direction (i.e. top actuators elongate while bottom actuators contract) which causes torsion in a certain direction. The next section was actuated to produce bending in the opposite direction, but since

the fiber direction was different the torsion was in the same direction as for the first section. This way, when all the sections along the span of the beam were actuated no net bending resulted, but a net twist at the end of the beam was effected. An alternate concept also proposed within this paper was to fix the bending-torsion beam to the tip of a regular blade. Actuating the beam would then cause the entire blade to twist. Prototypes of both these concepts were constructed and hover tested. The active tip deflected about two degrees for most excitation frequencies, whereas the active twist rotor only saw tip deflections of about a third of a degree.

Chandra [86] also presented a bending-torsion coupled beam actuated by shape memory alloy elements whose memory shape was that of a bending deformation. Two graphite-epoxy beams were constructed with sleeves where the SMA elements could be inserted. One beam was laid up with the fibers oriented at 15 degrees relative to the longitudinal axis. With the SMA bender elements activated, the 24 inch long graphite-epoxy beam twisted by approximately 1.9 degrees. This experimental result agreed very closely with the analytical prediction also presented in this paper. This same analysis also predicted a 6 degree twist in a 22.5 degree Kevlar-epoxy composite. Such a beam could potentially be used as the main spar in a rotor blade, a propeller, or a wing in order to vary the twist.

The final twist variation category is referred to here as spar modification methods. The idea is to move or adjust the spar of a wing or rotor blade so as to change the torsional stiffness of the structure or to move its shear center. By doing so, aerodynamic forces could cause twist deformations. The amount of twist would be controllable by adjusting the position or orientation of the spar. Amprikidis and Cooper [87] presented two concepts for changing the torsional stiffness of a wing: a chord-wise movable spar and a rotating spar. These concepts also appeared in a paper by Cooper a few years later [88].

Variable Camber

Shifting the focus now to variable camber concepts it is again possible to classify the various proposed methods. These classification categories are the entire section variation concepts, the multi-element rib concepts, truss configuration schemes, and the compliant structure methods. Past work will be discussed according to the category in which they are most suited, and these categories will be covered in the order mentioned.

As the name implies, entire section variable camber concepts forces the entire airfoil to change shape without a rib structure that is designed to allow for the camber change. For example, Ott [89] considered a variable camber fan blade for a turbofan engine. The proposed approach was to mount an SMA strip onto either the top or bottom surface of the thin solid blade cross section. For the case of the SMA strip attached to the bottom surface, the memory shape was a highly cambered arc that would increase the camber when activated. The strip mounted to the upper surface would have the opposite effect of flattening out the blade section when heated. Analytical and numerical predictions suggested that it would be possible to cause both the leading and trailing edge of the fan blade to deflect by about three to four degrees. Bilgen et al [90] also considered camber change of a solid thin airfoil but here the application was intended for the wing of a ducted fan UAV. Actuation was achieved using a piezoelectric bi-morph. Another concept also related to that of Ott for increasing the camber of wind-turbine blades was found in a patent awarded to Beauchamp and Nedderman [91]. The idea in this case was to have an SMA wire running in the chord-wise direction embedded in the structure. Upon activation the wire would contract and cause an increase in the blade camber.

Büter, Ehlert, and Breitbach [92] proposed a variable camber rotor blade that made use of tension-torsion coupling. The composite fiber orientation of the rotor skin forward of the main

spar would be at an angle relative to the span-wise axis, and the fibers aft of the main spar would be angled in the opposite direction. Inducing a bending moment through the use of piezoelectric stack actuators would cause opposite torsional moments forward and aft of the main spar resulting in a change of camber. Finite element analysis of this concept applied to a section with a 270 mm span that was fixed at one end showed that an increase in camber of slightly less than half a percent chord would result at a section located at about 2/3 span.

Actuating the skin of an airfoil was a concept also considered by Strelec et al. [93] and Bil, Massey, and Abdullah [94]. In both cases SMA wires were attached to the upper surface of the airfoil skin slightly aft of the leading edge and anchored to the bottom of the spar. In the paper by Strelec et al SMA wires were also run to the upper surface slightly forward of the trailing edge. Wind tunnel models were fabricated with skins made out of acrylonitrile butadiene stryrene (ABS) plastic. Both papers showed a trailing edge deflection of about six millimeters. Lift coefficient measurements by Bil et al. showed an increase in the lift coefficient of about 0.02 at zero degrees angle of attack, dropping to an increase of only about 0.007 at 10 degrees angle of attack.

The remaining three camber variation categories are set apart from the entire section methods in that the wing or rib structure is designed for the purpose of morphing. A multi-element rib is one that is constructed from a number of elements that are able to rotate relative to one another. A traditional wing with a flap could be considered as having a multi-element rib architecture, but what sets this category apart from the regular wing flap is that the concepts to be discussed achieve continuous shape changes without gaps in the outer surface.

Monner, Sachau and Beitbach [95] considered a variable geometry flap for a large civil transport aircraft. The trailing edge of the flap was designed so that it could be deflected either

up or down by making use of multiple rib segments. The main fixed rib segment would be the section that attaches to the flap spars, and the trailing edge segments would attach to one another and the main segment by means of revolute and prismatic joints. These joints were arranged in such a way that by only actuating the first movable rib segment all the other rib segments would also rotate relative to the segment to which it is attached. The flap skin was attached to the ribs by means of linear slider joints. At the trailing edge the skin would be allowed to slide over the rib as well. A demonstrator of the flexible rib was constructed to show that the multi-element concept worked, but a wing section with a skin was not built. This finger like trailing edge design is shown in Figure 2.1.

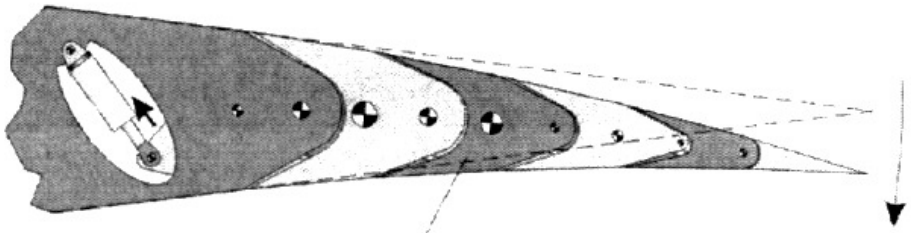

Figure 2.1. Multi-element rib concept, from Ref. [95].

Poonsong [96] constructed and tested a multiple section variable camber wing section. The ribs were composed of six elements that were free to rotate relative to each other. Flexible music wires were used to keep the wing section in the low camber configuration, and pneumatic linear actuators increased the camber of the structure. Barbarino, Pecora et al. in 2009 [97] proposed a multi-element trailing edge where the segments would be attached using elastic hinges. Shape memory alloy wires would run between segments along the top and bottom of the rib. Actuating the upper SMA wires would cause an upward deflection while contraction of the bottom wires would cause downward deflection. In this paper [97] the authors determined the appropriate geometry for the elastic hinges and performed a numerical simulation of a four-hinge

trailing edge configuration. In the presence of aerodynamic loads the results indicated that a trailing edge deflection of almost 30 degrees might be possible.

Pecora, Barbarino et al. [98] also examined a multi-section trailing edge with revolute joints to be used instead of flaps on a regional commuter aircraft. The kinematics of the joint configuration was also such that only the first element had to be actuated in order for all of the elements to rotate in the same direction. The proposed actuator was an SMA ribbon that was attached to an arc spring configuration that forced the SMA and the trailing edge back to the un-deflected state. A three element prototype of this rib configuration was built and static tests showed deflections of up to 15.5 cm. Wang, Xu and Zhu [99] also constructed a three element trailing edge, but in this case two SMA wires along with a pin joint held each segment in place. One of the SMA wires was near the upper surface and the other near the lower surface so that the wires would work antagonistically. Trialing edge deflection angles of up to seven degrees were reported.

Moving now to schemes incorporating truss-like structures for the rib geometry, it will be seen that the distinguishing feature of these concepts is the use of pin-connected truss elements. These elements are arranged so as to allow for chord-wise camber changes but are still capable of supporting aerodynamic forces. The first truss structure concept was the Parker variable camber wing introduced in 1920 [100]. The ribs of this wing would deform from a low speed high camber shape to low camber at high speed. These camber changes would occur passively by changing aerodynamic forces with increasing airspeeds. The base structure of the rib was an outer skin segment attached to vertical pin-jointed trusses that would maintain the section thickness but allow for camber change. In between the vertical trusses diagonal steel ribbons were placed in such a way that some of these elements would be bent in the high camber

configuration while the other elements would be loaded in tension so as to limit the maximum camber. In the low camber configuration the steel ribbons that were in tension before would be bent and the bent ribbons would be straight, limiting the minimum camber. Wind tunnel tests of low and high camber airfoils were performed and a prototype for static load tests was constructed, but it does not appear that the concept was tested in a wind tunnel.

A different truss structure was studied by Baker and Friswell [101] in which the truss elements were pin connected and arranged in a triangular shape. Only the portion of the rib aft of the main spar would have this configuration. The idea was that some of the truss elements would be active elements that could either contract or expand upon actuation. With the pin joint configuration the active truss element would be the only members that experience a strain upon actuation. Thus the actuators do not need to overcome the stiffness of the rib structure in order to be able to change the camber. Figure 2.2 shows a 14 element arrangement of this truss structure in the actuated state where three of the elements were active members.

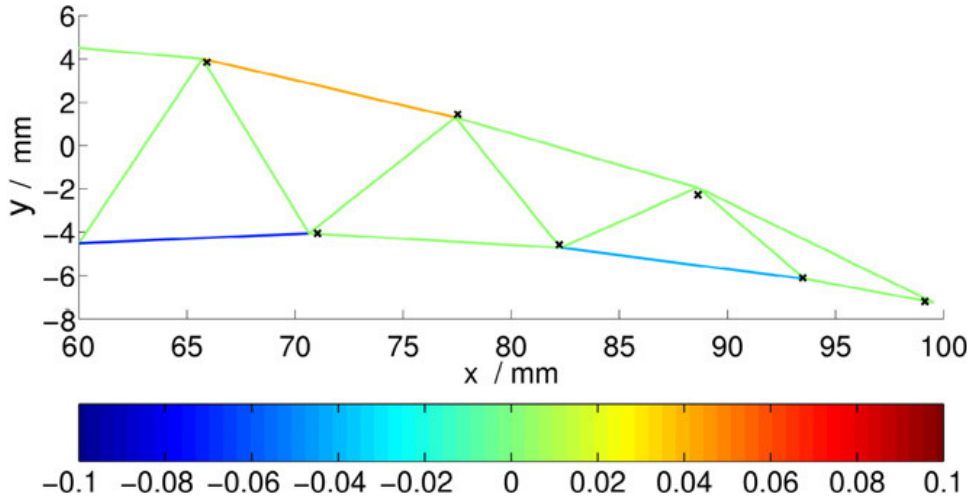

Figure 2.2. Actuated 14 element truss structure. From Ref. [101][*].

[*] © IOP Publishing. Reproduced by permission of IOP Publishing. All rights reserved.

It can be seen in this figure that the two lower surface actuators were contracted, the upper surface actuator was elongated, and the inactive members are unstrained. This idea was extended to a truss structure with 1752 elements of which 88 elements were active elements.

A related trailing edge truss structure actuated by SMA was introduced by Barbarino, Dettmer, and Friswell [102]. The basic structural element consisted of two rigid elements attached to one another at one end, and together with a shape memory alloy element would form a triangular shape. This SMA element could either be attached to the ends of the two rigid elements, or perhaps to the end of one and somewhere in between the end and the hinge on the other. This latter arrangement can be seen in Figure 2.3 where the actuated red SMA elements are attached to the end of one of the rigid elements and close to the hinge on the other rigid element. The truss concepts introduced in references [101] and [102] were both only studied as an optimization problem to determine either, in the case of reference [101], the optimum actuator placements, or, in reference [102], the optimum truss configuration and actuator attachment points. In neither case was there a prototype built.

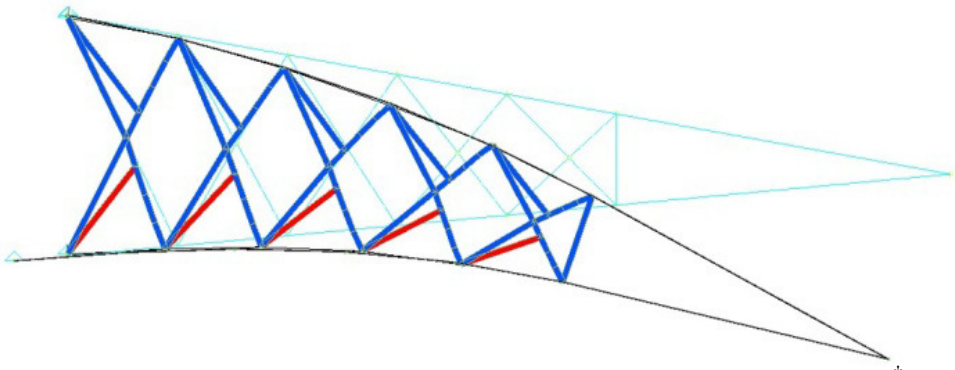

Figure 2.3. Morphing trailing edge truss structure from Ref. [102][†].

The following paper to be discussed fits into both the compliant structure category and the truss structure category. A compliant wing or rib structure is very similar to the truss

[†] Reproduced with permission from authors.

structure concepts in that the structure is designed to allow for camber variations while being resistant to other types of deformation, but the distinguishing feature is that all the structural elements are compliant (either completely or at the junctures) and deform elastically to allow for camber variations. Gandhi, Frecker and Nissly [103] proposed an active truss structure where the basic shape consisted of two vertical members and two diagonal members in an X-configuration attached to the end of the vertical members. The diagonal members, in the initial concept, were pin-connected at the location that they crossed and at their connections the vertical elements. The vertical elements would be the active members, capable of either contracting or expanding. Within the airfoil structure the basic shape of two vertical and two diagonal elements were repeated along the chord and stacked two layers high. Camber increase was achieved when the lower piezo stacks were elongated and the upper stacks were shortened. The pin joints were done away with in favor of a single X-shaped truss with compliant joints. A schematic of this truss rib arrangement is shown in Figure 2.4. A prototype with five vertical elements (as shown in Figure 2.4) was fabricated with a 560 mm chord length. Bench-top tests showed a static trailing edge deflection of up to 3.6 mm.

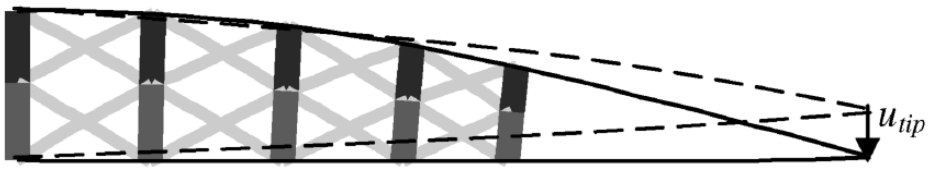

Figure 2.4. Schematic of the active rib tested by Gandhi et al [103][‡].

The belt-rib concept (Figure 2.5) is a compliant structure approach in which a continuous layer (the "belt") forms the outer airfoil shape [104]. Internally, spokes connect the upper and lower airfoil surfaces. These spokes are attached to the airfoil surfaces by means of soft joints

[‡] © American Institute of Aeronautics and Astronautics. Reproduced with permission. All rights reserved.

that allow flexing so that the primary function of the spokes is to carry tension and compression loads. Actuating the upper airfoil surface relative to the bottom surface causes a change in camber since the spoke-belt juncture allows for this type of flexing. The authors of reference [104] suggested that SMA wires running diagonally between the upper and lower airfoil surfaces would be feasible, but their prototype was built only for the purpose of proving the structural integrity of the concept and to show that trailing edge deflections were possible. In a paper published in 2012 [105], Previtali and Ermanni also considered the belt-rib concept and performed a two dimensional finite element and aerodynamic analysis of the concept, as well as a three dimensional analysis. Their results suggested that the actuation forces required to increase the aerodynamic efficiency (lift-to-drag ratio) of a wing would be low.

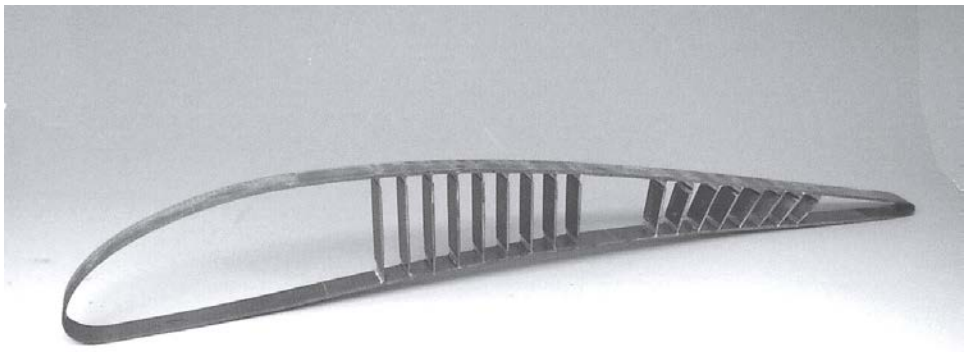

Figure 2.5. Picture of the belt-rib prototype from Ref. [104][§].

Chiral-core airfoils are a different compliant structural arrangement that has a large in-plane shear stiffness and a high chord-wise compliance to allow for camber changes [106]. The basic truss structure is a triangular arrangement with circular elements at the vertices. The elements that form the sides of the triangle, referred to as the ligaments, meet the circular

elements tangent to their outside surfaces. This arrangement is shown in Figure 2.6. Spadoni and Ruzzene [106, 107] performed numerical and experimental evaluations of airfoils with chiral truss structures like that shown in Figure 2.6 (b). The idea was that the airfoil should be highly cambered in the un-deformed state and then with increasing flow velocities the camber would passively decrease.

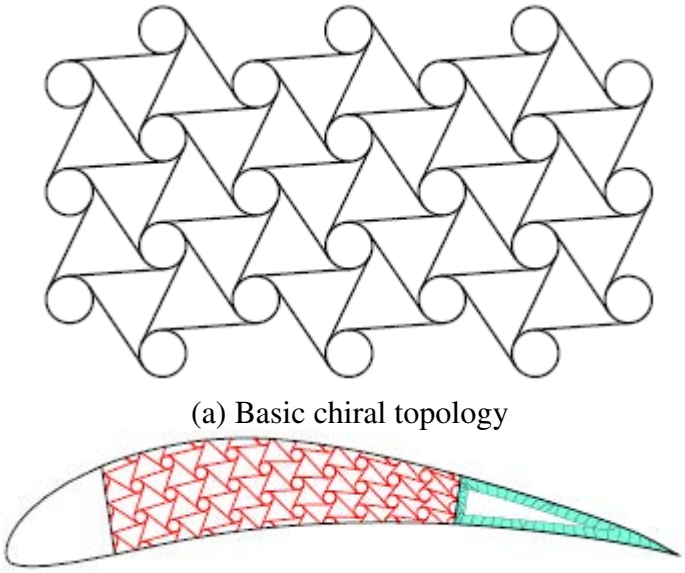

(a) Basic chiral topology

(b) Example of chiral-core airfoil

Figure 2.6. Illustrations of chiral arrangements from Ref. [106]**.

Three parameters that define the chiral topology within the airfoil, namely the ligament length, the distance between circular node centers, and the number of cells across the airfoil thickness, were varied in order to study the effect of aerodynamic loading on the structure. Lower values of the ratio between the ligament length and the node center distance reduced the stiffness of the structure resulting in larger trailing edge deflections [107]. Static load experiments with a point load applied near the trailing edge of three different prototype ribs were also performed. These tests showed that increasing the number of cells across the thickness from two to three resulted in

a higher force being required for an equal trailing edge displacement [106]. Airoldi et al. [108] also considered a chiral-core topology for a morphing sail. Aeroelastic effects alone caused the camber of the sail to increase with the angle of attack from a symmetrical shape at zero angle of attack. A numerical evaluation and optimization of the chiral structure was performed in order to maximize the lift-curve slope at zero degrees angle of attack. The resulting geometry was predicted to have a chord-wise continuous camber increase up to an angle of attack of 10 degrees.

In closing this section of the review the concepts presented here are evaluated in terms of their viability as solutions for propeller blade shape change. It has already been mentioned that the trailing edge flap approach for effecting twist changes is not considered feasible. The reason for this is that concepts that add additional elements and hinges also add a level of dynamical complexity that may cause undesirable instabilities. Only solutions that provide solid, continuous blade structures are thus considered feasible. This immediately eliminates the spar modification, multi-element, and truss structure solutions. For twist actuation this leaves the integral twist and tension-torsion coupling concepts.

Propeller blade structures that exhibit a degree of tension-torsion coupling are seen as a viable concept, although those methods discussed in the review are not necessarily directly applicable. A propeller blade is not large enough to house a separate bending torsion beam, and bending out of the plane of rotation is undesirable. Instead it is thought that the entire blade structure should exhibit tension-torsion coupling. An important thing to consider with such a design is the centrifugal loading on the blade which causes a large amount of span-wise tensile loading. A tension-torsion coupled blade structure will thus twist with increasing angular velocity. It may be possible, however, to design the blade structure so that one of the desired

twist distributions is reached when the blade is at its operating rate of rotation. Shape memory alloys embedded span-wise within the structure could then be actuated to contract, and, in doing so, reduce the amount of tensile load carried by the blade structure. Reducing the tension in the structure will result in a change in twist. Integral twist actuation, with SMA wires embedded in the blade skin at 45 degree angles relative to the longitudinal axis is also seen as a viable concept. With both of these concepts, however, a significant challenge will be to tailor the twist changes so that not only the desired amount of twist change is achieved, but also the desired span-wise distribution of the twist.

In terms of camber morphing concepts, the entire section approach is perhaps the simplest to implement. A number of configurations are possible with this approach. For example, SMA elements trained to contract could be placed near the bottom airfoil surface. Or alternatively, an SMA ribbon that assumes a bending shape when heated could be mounted inside the blade cross section on the chord-wise neutral axis. A compliant internal structural configuration could be combined with the whole section actuation method to reduce the required actuation force. Thus both the entire section morphing and compliant structure approaches are seen as viable solutions.

From the literature review presented here it does appear that propeller blade morphing is physically possible, though the concepts introduced here still require some analysis in order to verify this claim. A simplified structural analysis and evaluation of two of the concepts discussed here, namely the camber morphing and tension-torsion coupled blade, is presented in Chapter 5 in order to examine the feasibility of structural morphing. These analyses make use of the propeller optimization results presented in Chapter 4 as the benchmark for the required shape changes, and the measure for determining feasibility.

2.5 Chapter Summary

This chapter provided a literature review of propeller aerodynamic prediction methods, propeller optimization schemes, and morphing structures, as well as introducing a number of smart materials. The purpose of the aerodynamic prediction and optimization reviews was to choose the appropriate methods for this study. It was concluded that the blade element method along with vortex theory is a sufficiently accurate and efficient method for analyzing conventional propellers. Calculus of variations was chosen as the propeller twist optimization scheme after considering the objective, number of design variables, and the constraints. The third section of this review was devoted to smart materials and concepts for twist and camber change. The objective of this section of the review was to select an appropriate actuator material and to consider concepts that are viable for propeller blade morphing. A number of possible concepts were discussed, and it was also concluded that shape memory alloys should be able to provide the necessary actuation force and stroke.

The following chapter is devoted to discussing the propeller performance prediction method that was chosen in this chapter.

CHAPTER 3

PROPELLER PERFORMANCE ANALYSIS

3.1 Introduction

In this chapter a detailed discussion of the aerodynamic model used for the purpose of propeller performance prediction will be given. Emphasis will be placed on the description of the airfoil model as accurate modeling of the aerodynamic characteristics greatly affects the accuracy of the propeller performance predictions. The chapter will close with a section devoted to comparing prediction results with experimental data in order to validate the model developed here.

3.2 Propeller Aerodynamic Model

As was discussed in the preceding chapter the blade element method was chosen for the purpose of performance predictions. This formulation will be derived in the following section, followed by a discussion of the vortex theory of Goldstein which is used here to determine the induced velocity for each blade element. The airfoil model description will conclude this section.

3.2.1 Blade Element Method

In the blade element method a propeller is analyzed by dividing a blade into strips along the span of the blade (Figure 3.1). Each strip is then considered to be a two-dimensional airfoil with the performance of each strip determined from knowledge of the airfoil characteristics and the local flow experienced by each element. The local flow at an element is composed of a rotational velocity component, ωr, a forward velocity component, v_∞, and an induced velocity, w. These velocities are illustrated in Figure 3.2.

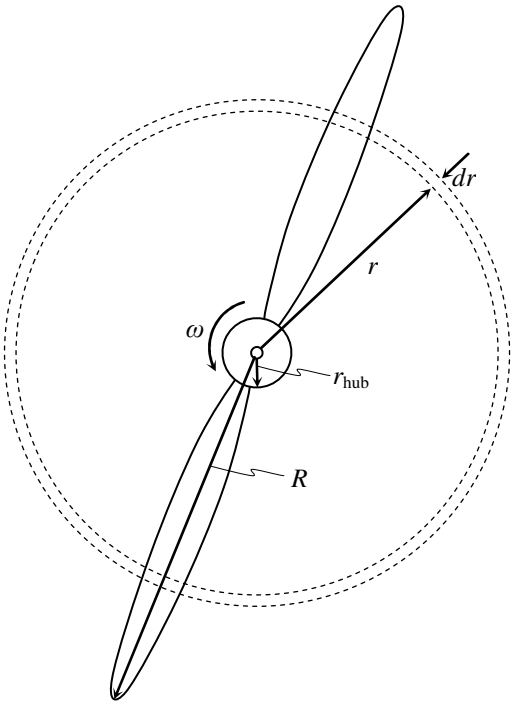

Figure 3.1. Front view of a two bladed propeller.

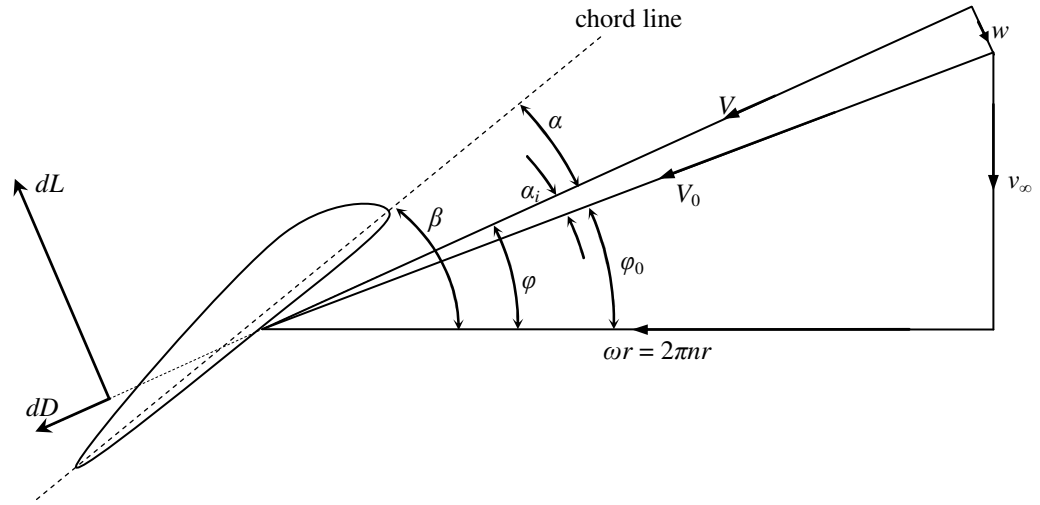

Figure 3.2. Schematic of the local flow.

The rotational and forward velocity components are perpendicular to one another and together define the advance helix velocity, V_0, and angle, φ_0, of this blade element. The advance helix is the helical path traced out by a single blade element in an earth fixed coordinate system. In order to determine the true flow velocity relative to the blade element, V, the induced velocity (which

is assumed to be normal to the relative velocity) needs to be determined. Different methods exist for determining the induced velocity but here the vortex theory, to be discussed in the following sub-section, is used. Once the induced velocity is known parameters such as the induced angle, α_i, the angle of attack, α, and the wake helix angle, φ, is determined. A propeller wake is also a helix but because of the flow induced by the propeller the wake helix angle is different from the advance helix angle. The last remaining angle in Figure 3.2 is the blade angle, β, between the plane of rotation and the section chord line. This angle is typically known in performance analysis.

With the flow geometry of a blade element defined the process of determining the thrust and the torque of the propeller is now undertaken. Thrust is defined to be the force component in the direction of flight; torque is the product of the force component acting in the plane of rotation and the radial distance, r, to the element from the center of the propeller. The width of each element, dr, is assumed to be of differential size so that the thrust and torque contribution of each element may be written as dT and dQ, respectively. From Figure 3.2 the differential thrust and torque are written as shown in equations (3.1) and (3.2), where the factor B is the number of blades in the propeller.

$$dT = B\left(dL\cos\varphi - dD\sin\varphi\right) \tag{3.1}$$

$$dQ = Br\left(dL\sin\varphi + dD\cos\varphi\right) \tag{3.2}$$

The thrust and torque coefficients are defined by equations (3.3) and (3.4), where ρ is the air density, n the propeller rate of rotation in revolutions per second, and D the propeller diameter.

$$C_T = \frac{T}{\rho n^2 D^4} \tag{3.3}$$

$$C_Q = \frac{Q}{\rho n^2 D^5} \tag{3.4}$$

Applying the thrust and torque coefficient definitions to equations (3.1) and (3.2) and also writing the lift and drag forces in coefficient form, equations (3.5) and (3.6) are obtained.

$$dC_T = \frac{B}{\rho n^2 D^4}\left[\left(\frac{1}{2}\rho V^2 c C_L dr\right)\cos\varphi - \left(\frac{1}{2}\rho V^2 c C_D dr\right)\sin\varphi\right] \tag{3.5}$$

$$dC_Q = \frac{Br}{\rho n^2 D^5}\left[\left(\frac{1}{2}\rho V^2 c C_L dr\right)\sin\varphi + \left(\frac{1}{2}\rho V^2 c C_D dr\right)\cos\varphi\right] \tag{3.6}$$

These two equations are simplified by making use of the solidity, σ, the advance ratio, J, and a non-dimensional radial coordinate, x, defined in equations (3.7) to (3.9), respectively. The chord length of each element is given by c.

$$\sigma = \frac{Bc}{\pi R} \tag{3.7}$$

$$J = \frac{v_\infty}{nD} \tag{3.8}$$

$$x = \frac{r}{R} \tag{3.9}$$

The result of the simplification is shown in equations (3.10) and (3.11).

$$dC_T = \frac{\sigma\pi}{8}\left(J^2 + \pi^2 x^2\right)\cos^2\alpha_i\left(C_L\cos\varphi - C_D\sin\varphi\right)dx \tag{3.10}$$

$$dC_Q = \frac{\sigma\pi x}{16}\left(J^2 + \pi^2 x^2\right)\cos^2\alpha_i\left(C_L\sin\varphi + C_D\cos\varphi\right)dx \tag{3.11}$$

The thrust and torque coefficients for the entire propeller can now be determined by summing the contribution of each individual element. Since the width of each element is considered to be infinitesimally small, this sum can be written as the integral over the entire blade span. Any real propeller, however, has a hub in the center to which the blades attach, and the blade thus only begins some distance, r_{hub}, away from the center. Accordingly, integration over the entire span implies integration from the non-dimensional hub radius, x_{hub}, to 1. The

total propeller thrust coefficient is now determined from the integral in equation (3.12), with the thrust coefficient integrand, T_c, being defined by equation (3.13), and the thrust coefficient integrand multiplier, τ, by equation (3.14).

$$C_T = \int_{x_{\text{hub}}}^{1} T_c \, dx \tag{3.12}$$

$$T_c = \tau \cos^2 \alpha_i \left(C_L \cos \varphi - C_D \sin \varphi \right) \tag{3.13}$$

$$\tau = \frac{\sigma \pi}{8} \left(J^2 + \pi^2 x^2 \right) \tag{3.14}$$

Similarly the torque coefficient, torque coefficient integrand, Q_c, and torque coefficient integrand multiplier, ζ, are defined by equations (3.15) to (3.17), respectively.

$$C_Q = \int_{x_{\text{hub}}}^{1} Q_c \, dx \tag{3.15}$$

$$Q_c = \zeta \cos^2 \alpha_i \left(C_L \sin \varphi + C_D \cos \varphi \right) \tag{3.16}$$

$$\zeta = \frac{\sigma \pi x}{16} \left(J^2 + \pi^2 x^2 \right) \tag{3.17}$$

Power is simply the product of the propeller angular velocity, ω, with the torque. Therefore, power coefficient can be defined as in equation (3.18).

$$C_P = \frac{P}{\rho n^3 D^5} = 2\pi C_Q \tag{3.18}$$

So now the total power coefficient, power coefficient integrand, P_c, and power coefficient integrand multiplier, ξ, is obtained as shown in equations (3.19) to (3.21), respectively.

$$C_P = \int_{x_{\text{hub}}}^{1} P_c \, dx \tag{3.19}$$

$$P_c = \xi \cos^2 \alpha_i \left(C_L \sin \varphi + C_D \cos \varphi \right) \tag{3.20}$$

$$\xi = 2\pi\zeta = \frac{\sigma \pi^2 x}{8} \left(J^2 + \pi^2 x^2 \right) \tag{3.21}$$

The final parameter needed for a complete performance analysis is the propeller efficiency, η. The typical definition for efficiency is a ratio of useful energy output to the amount of energy input. Or, similarly, since power is energy per unit time, efficiency can be written as the useful power output divided by the power input. A propeller's "usefulness" is in the thrust it produces. Therefore, power output (also referred to as power available or thrust power) is defined as the product of the aircraft forward velocity and the thrust. Thus efficiency of a propeller is defined by the left hand part of equation (3.22), which can also be cast in terms of the thrust and power coefficients as shown by the right hand part of this equation.

$$\eta = \frac{Tv_\infty}{P} = \frac{C_T J}{C_P} \tag{3.22}$$

Although thrust, power, and efficiency are all that is needed for a full propeller performance analysis, it is worthwhile to also consider the power loss. Power loss, P_L, is simply the difference between the input and output power, as shown in equation (3.23). Writing this equation in elemental form and substituting equations (3.1) and (3.2) results in equation (3.24). By considering the geometry of Figure 3.2, Equation (3.24) is simplified into equation (3.25) where two sources of power loss are shown, namely the induced power loss, $P_{L,i}$, and the drag power loss, $P_{L,D}$.

$$P_L = P - Tv_\infty \tag{3.23}$$

$$dP_L = B\left[\omega r\left(dL\sin\varphi + dD\cos\varphi\right) - v_\infty\left(dL\cos\varphi - dD\sin\varphi\right)\right] \tag{3.24}$$

$$dP_L = dP_{L,i} + dP_{L,D} = B\left(wdL + VdD\right) \tag{3.25}$$

Writing equation (3.25) in coefficient form and simplifying using equations (3.7) through (3.9) results in equation (3.26).

$$dC_{PL} = \frac{\sigma\pi}{8}\left(J^2 + \pi^2 x^2\right)^{3/2} \cos^2\alpha_i \left(C_L \sin\alpha_i + C_D \cos\alpha_i\right) dx \tag{3.26}$$

The full propeller power loss coefficient is given by the integral of equation (3.26) from the hub to the blade tip. The result of this operation is given by equation (3.27), along with the definitions of the power loss coefficient integrand, P_{Lc}, and the power loss coefficient integrand multiplier, χ (equations (3.28) and (3.29)).

$$C_{PL} = \int_{x_{\text{hub}}}^{1} P_{Lc}\, dx \tag{3.27}$$

$$P_{Lc} = \chi \cos\alpha_i \left(C_L \sin\alpha_i + C_D \cos\alpha_i\right) \tag{3.28}$$

$$\chi = \frac{\sigma\pi}{8}\left(J^2 + \pi^2 x^2\right)^{3/2} \tag{3.29}$$

The thrust, torque, power, and power loss coefficients are all defined in terms of the lift and drag coefficients, the induced angle, and the wake helix angle. All these variables are dependent on the induced velocity. So in order to evaluate the performance of a propeller this parameter needs to be determined.

3.2.2 Vortex Theory

Two of the most common methods for determining the induced velocity are momentum theory and vortex theory. In momentum theory the flow through the propeller disc is assumed to be two-dimensional, and therefore, three-dimensional effects such as losses due to the finite blade tip are neglected. Vortex theory, on the other hand, is a lifting line theory similar to that for wings where the trailing vortex sheet is used to determine the induced velocity at the section being considered; the only effect of the induced velocity considered is the change in angle of attack. A sketch of the induced flow geometry is shown in Figure 3.3. For the case of a propeller the trailing vortex sheet forms a helical surface that, relative to the fluid medium, moves perpendicular to itself at the induced velocity. In this theory the distribution of vorticity

along the blade span is assumed to be such that the induced power loss would be a minimum [14]. This is the same as assuming a wing to have an elliptical lift distribution, but instead of a constant span-wise downwash a propeller has a constant span-wise vortex displacement velocity. In the case of a wing, each element operates at the same speed so that constant downwash results in a rigidly moving trailing vortex sheet behind the wing. But for a propeller to have a rigidly moving trailing helical vortex sheet, the downwash at the blade root needs to be much stronger than at the tip due to the large variation in the flow velocity from root to tip. Due to the rigid wake assumption, however, vortex theory does not give an exact solution for the induced velocity because a propeller does not always operate at its design point. For the purpose of off-design performance predictions it is basically assumed that each blade element is part of an ideally shaped blade that produces an ideal rigid wake. The approximations obtained from vortex theory have been shown to be very good [10], and at the very least vortex theory is a method for determining the induced velocity that includes the tip loss phenomenon.

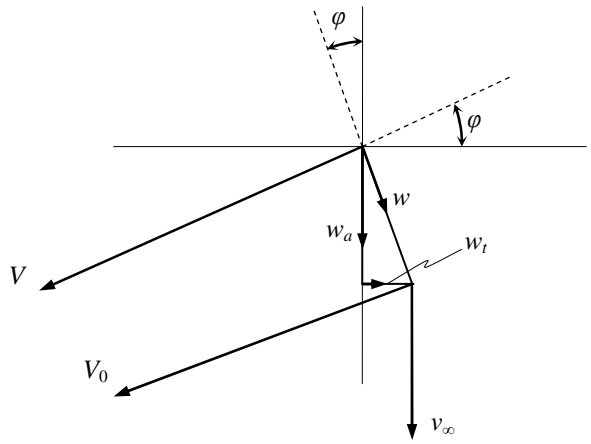

Figure 3.3. Axial and tangential components of induced velocity.

The usable form of the vortex theory is given by equation (3.30) and gives the circulation strength, Γ, about an element at radius, *r*, in terms of the induced velocity, the wake helix angle, and a tip loss factor, *G*.

$$\Gamma = \frac{4\pi rG}{B} w \sin\varphi \tag{3.30}$$

Two commonly used solutions for the tip loss factor are an approximation introduced by Prandtl in 1919 [12], and an exact result later published by Goldstein in 1929 [14]. The Prandtl tip loss factor, G_P, given by equation (3.31), is an approximation that is asymptotic in the large blade count limit and assumes lightly loaded blades [7]. Thus the accuracy of the approximation decreases with decreasing blade counts, or increased blade loading.

$$G_P = \frac{2}{\pi} \arccos\left[\exp\left(\frac{B(x-1)}{2\sin\varphi_T} \right) \right] \tag{3.31}$$

Goldstein's tip loss factor, G, on the other hand, is an exact solution for the case of ideal span-wise blade loading, but the solution does not have a convenient equation form and is typically found in table form. The value of the tip loss factor depends on the wake helix angle, the non-dimensional radial location, and the number of blades. Multiple tables are needed to cover the full range of these parameters. Examples of such tables are published in reference [16].

Once the circulation strength about a blade element is found, the lift per unit span can be determined from the Kutta-Joukowski theorem, equation (3.32). Combining equations (3.30) and (3.32) results in equation (3.33).

$$L' = \rho V \Gamma = \frac{1}{2} \rho V^2 c C_L \tag{3.32}$$

$$C_L = \frac{8x}{\sigma} G \tan\alpha_i \sin\varphi \tag{3.33}$$

For the case of incompressible flow, as is assumed in the derivation of the vortex theory, the lift coefficient only depends on the angle of attack. In the linear range of the lift coefficient curve plotted as a function of angle of attack this dependence can be written as in equation

(3.34). From Figure 3.2 equations (3.35) and (3.36) are written to complete the system of equations needed to solve for the induced velocity.

$$C_L = C_{L,\alpha}(\alpha + \alpha_{ZL}) \tag{3.34}$$

$$\varphi = \varphi_0 + \alpha_i \tag{3.35}$$

$$\beta = \varphi + \alpha \tag{3.36}$$

Equations (3.33) through (3.36) represent a system of four equations with four unknowns and are iteratively solved for the induced angle. Once this step is completed for each element along the blade span, the integration of equations (3.12), (3.15), (3.19), and (3.27) can be carried out to calculate the propeller performance parameters.

Even though the iterative solution of equations (3.33) through (3.36) executes rapidly on a desktop computer, an analytical solution for the induced angle is possible if it is assumed to be small. With this small angle approximation, equation (3.33) reduces to equation (3.37), where G_0 is used to indicate that the Goldstein factor is now determined based on the advance helix angle instead of the wake helix angle.

$$C_L = \frac{8xG_0 \sin\varphi_0}{\sigma}\alpha_i = \frac{\alpha_i}{b} \tag{3.37}$$

Since the non-dimensional radial coordinate, tip loss factor, advance helix angle, and solidity are all independent of the induced angle they are lumped into a single variable b for convenience. Note that b is the inverse of the derivative of equation (3.37) with respect to the induced angle. An additional effect of the small angle approximation is that the $\cos^2\alpha_i$ factor in equations (3.13), (3.16), (3.20), and (3.28) disappear since the cosine of a small angle is approximate equal to one.

In order to assess the accuracy and validity of the small angle approximation comparative results from both the iterative solution and the small angle approximation are presented in Figure 3.4 and Figure 3.5. In the first of the two figures the predicted induced angle and angle of attack

as a function of the advance ratio for a single blade element located at 75% radius at a blade angle of 30 degrees are shown. Above an advance ratio of approximately 0.9, the difference between the two approaches becomes almost negligible. In fact, for this particular case, the percent error in the induced angle prediction between the small angle approximation and the iterative solution becomes less than 5 percent. In the low advance ratio range the small angle approximation results in a grossly over-predicted induced angle and a significantly under-predicted angle of attack. Thus the drop-off in the thrust and power coefficients at low values of advance ratio, seen in Figure 3.5 (a) and (b), for the small angle case is expected from what is observed in Figure 3.4.

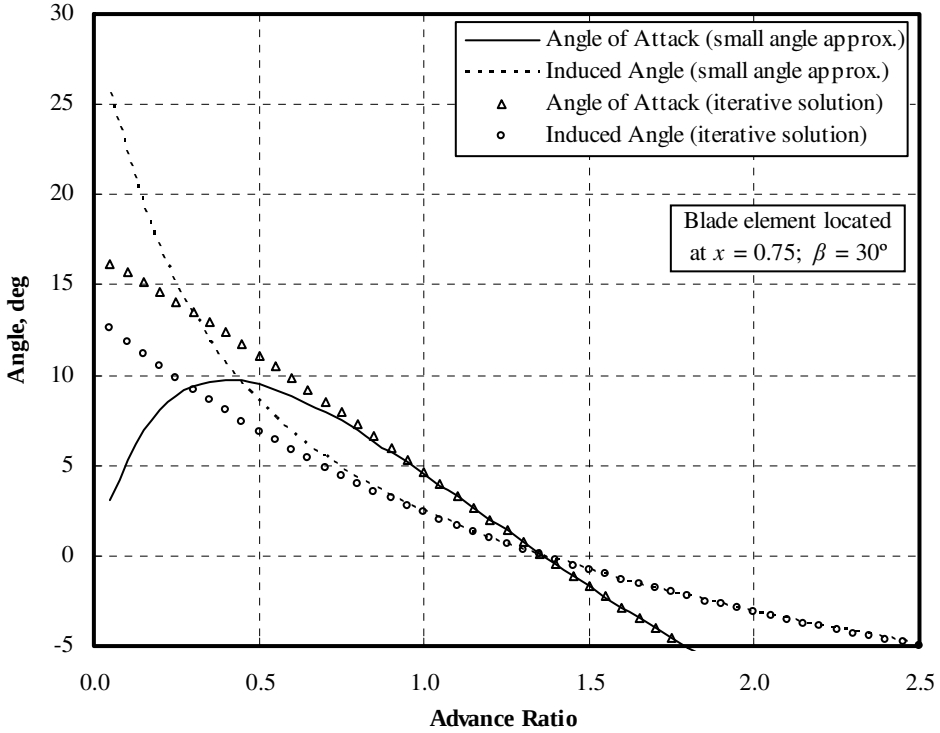

Figure 3.4. Effect of small angle approximation on α and α_i.

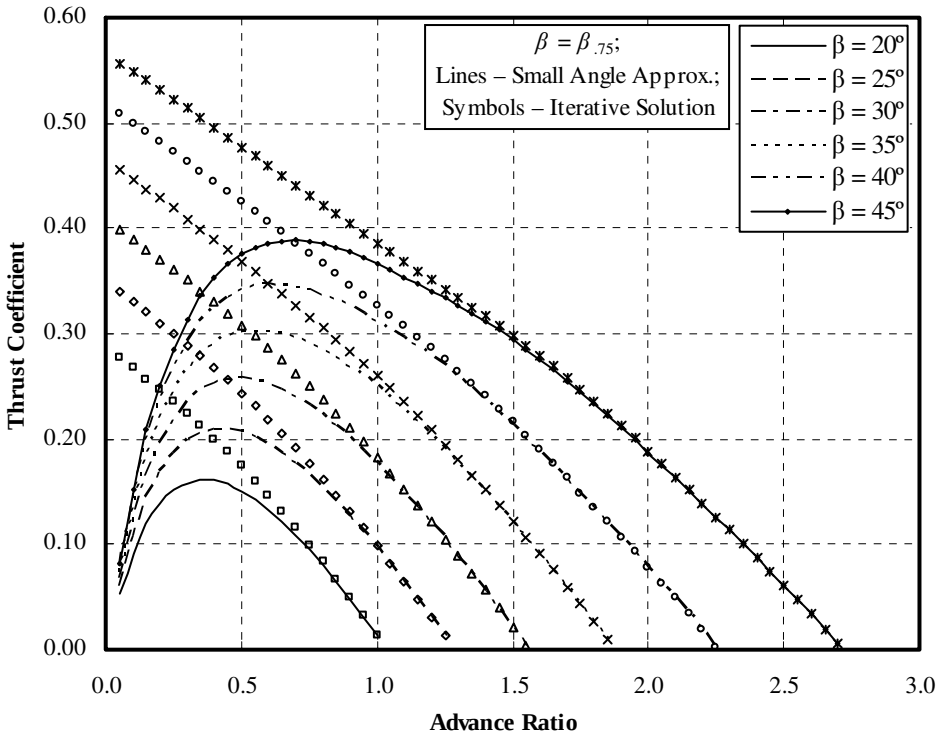

(a) C_T vs J

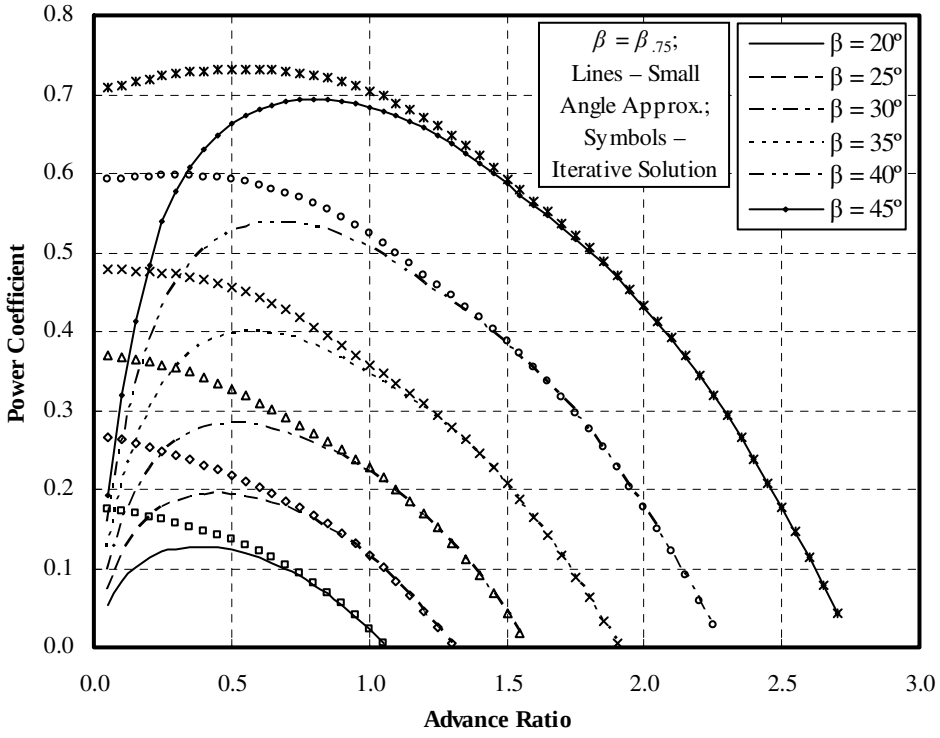

(b) C_P vs J

Figure 3.5. Effect of the small angle approximation on C_T, C_P, and η. (continued)

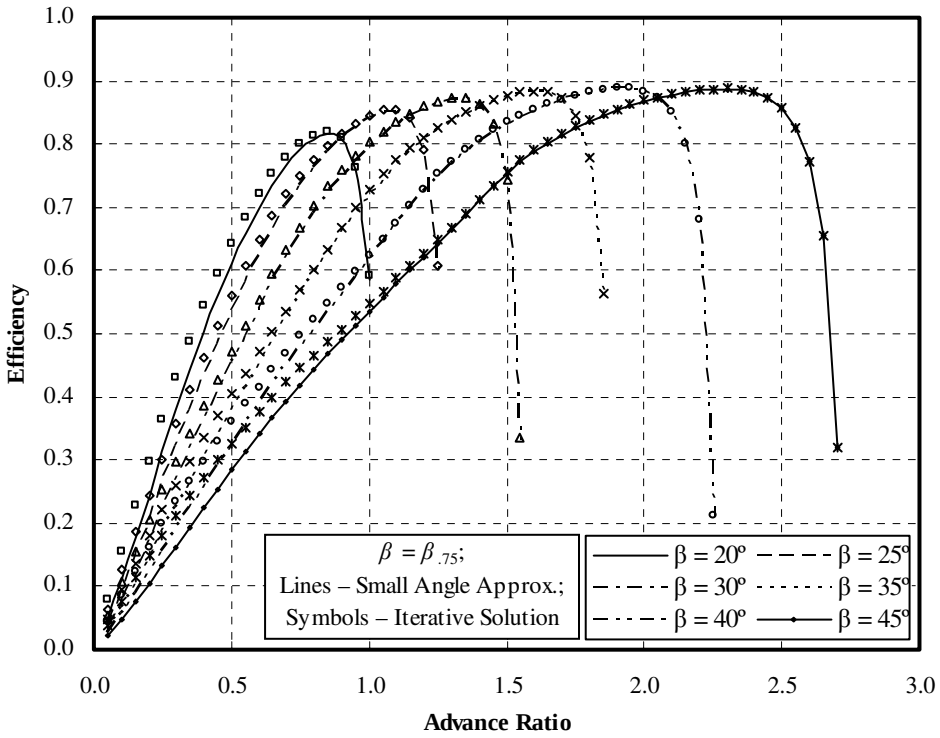

(c) η vs J

Figure 3.5. Effect of the small angle approximation on C_T, C_P, and η. (concluded)

Considering the case in Figure 3.5 (a) and (b) where $\beta_{.75}$ = 30 degrees it can again be observed that the difference between the two methods becomes negligible above an advance ratio of 0.9. This is the range of advance ratio in which peak efficiency lies. This is likely also the range in which a propeller will mostly be operating and suggests that the small angle approximation is valid for the majority of the operating envelope. Additionally, when optimizing a propeller, the small angle approximation will likely also be valid for the majority of cases since the goal is to increase efficiency. Something else to note in Figure 3.5 is the relative insensitivity of efficiency to differences or errors in the thrust and power coefficient predictions. This insensitivity will be seen again in the upcoming sections, but a conclusion that can be drawn already is that when a propeller performance prediction method is being validated the efficiency parameter should not be given as much weight as the power and thrust coefficients.

At this point the blade element method is described and a method for determining the induced velocity has been presented. What remains are details concerning the aerodynamic characteristics of each blade element.

3.2.3 Airfoil Model Description

In this section the development of the airfoil aerodynamic model used in the propeller predictions is discussed. The stall model and corrections made to the incompressible airfoil data to account for the effects of compressibility are also covered. The methods and corrections used here are generally applicable to any airfoil as long as certain airfoil specific experimental data are available. Certain parameters that go into the aerodynamic model can be predicted from an airfoil analysis program such as XFOIL. This still requires knowledge of either the exact airfoil coordinates, or enough information to generate coordinates at each span-wise blade station.

Lift Model

Figure 3.6 is a sketch of the typical behavior of the lift coefficient with angle of attack. Note that Figure 3.6 is a sketch so the values of both the lift coefficient and angle of attack in this plot are only illustrative. The lift coefficient of an airfoil of moderate thickness at low angles of attack is known to vary linearly with the angle of attack. This line is customarily defined by the lift coefficient slope, $C_{L,\alpha}$, and either the ordinate intercept, $C_{L,0}$, or the zero lift angle of attack, α_{zl}. At a certain angle of attack, α_1, the lift coefficient curve departs linear behavior with a decreasing slope. The slope continues to decrease through zero where a local maximum, referred to as the maximum lift coefficient, $C_{L,max}$, is reached at the stall angle of attack, α_{stall}. Both the angle at which the lift coefficient departs linear behavior and the stall angle of attack are dependent on a number of factors such as the Reynolds number, Mach number, airfoil camber, and thickness.

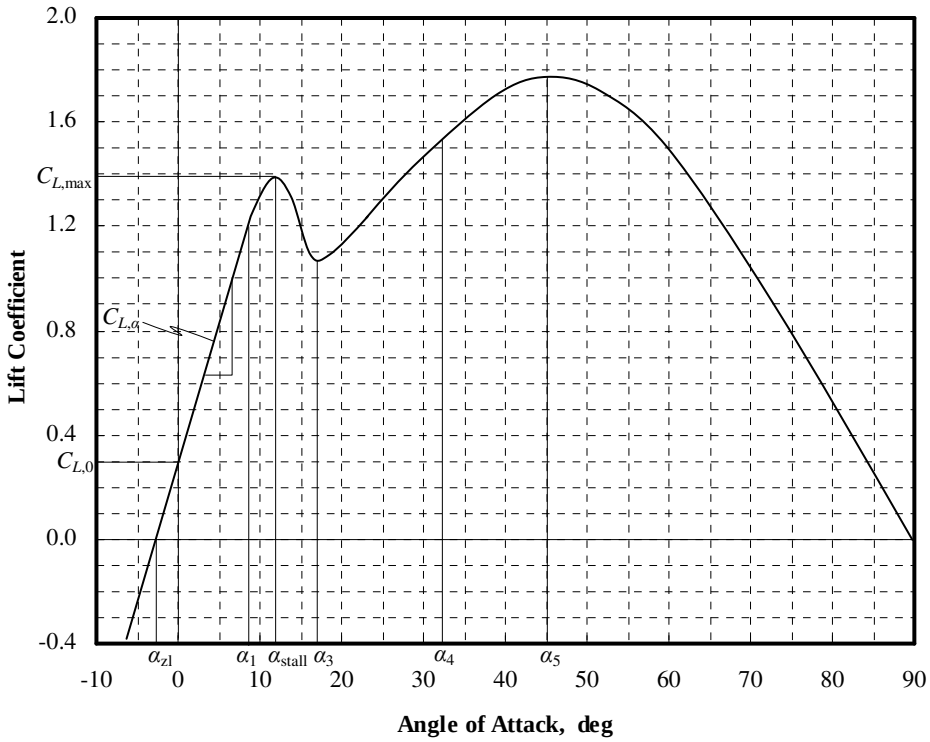

Figure 3.6. Sketch of C_L as a function of α.

Beyond the stall angle of attack the lift coefficient decreases towards the post stall minimum lift coefficient, which has a value that is anywhere from about 0.1 to 0.6 less than the maximum lift coefficient. Figure 3.6 shows the decrease from the maximum lift coefficient towards the post stall minimum to occur smoothly, but for some airfoils the onset of stall is rather abrupt with a rapid drop in the lift coefficient. Either way, the post stall minimum lift coefficient occurs at an angle of attack, α_3, that is approximately six degrees larger than the stall angle of attack. As the angle of attack continues to increase beyond the post stall minimum, the lift coefficient increases with a increasing slope up to some intermediate angle of attack, α_4, where the concavity of the curve changes. The lift coefficient continues to increase but with a declining slope up to a secondary maximum value at an angle of attack, α_5, of about 45 degrees. This second maximum is usually of equal or greater magnitude than the maximum lift

coefficient. From the maximum at 45 degrees the lift coefficient curve decreases to a value of about zero at an incidence angle of 90 degrees.

The above described lift coefficient behavior is modeled by dividing the curve into a number of segments. The first segment is the linear portion which is defined by the lift-curve slope and ordinate intercept. These parameters can be obtained from published experimental data such as in reference [109] if standard airfoils are used in the propeller. If non-standard airfoils, or airfoils for which published experimental data are not available, are used an airfoil analysis program (such as XFOIL [110]) can be used to predict these two values. This would, however, require airfoil coordinates at each radial blade station. If airfoil coordinates are not available, they could be generated from information such as airfoil family, airfoil thickness, t/c, and design lift coefficient, $C_{L,D}$. With the slope and ordinate intercept determined, the linear portion segment up to the linear departure angle of attack, α_1, is fully defined.

The next segment of the model is the stall regime from the linear departure angle of attack to the post stall minimum, α_3. In order to model this segment the three angles, α_1, α_{stall}, and α_3, need to be determined. Airfoil analysis software typically fails at accurately predicting boundary layer separation and cannot be used for determining the stall angle of attack. Experimental data is thus the best resource for defining this regime. Now it was mentioned that the linear departure and stall angles of attack depend on the Reynolds number and airfoil camber. Reynolds numbers of propeller airfoil sections on a full scale aircraft are typically on the order of 10^6 so that the stall angle of attack is not very sensitive to this parameter. Airfoil camber on the other hand primarily shifts the linear curve and maximum lift coefficient either up or down. The lift coefficient model thus does not include these two parameters in determining the linear departure and stall angles of attack and only includes the airfoil thickness and Mach number.

The Mach number effect will be discussed along with the compressibility corrections below. Thickness is accounted for by tabulating the linear departure angle, the stall angle of attack, and the change in the lift coefficient between these two angles for a variety of airfoil thicknesses. Ideally airfoil data that closely matches the airfoil family used in the propeller should be used. The stall angle of attack table is interpolated based on the thickness of the blade element under consideration to determine the approximate values of the linear departure angle, the stall angle, and the change in lift coefficient. The effect of camber on the maximum lift coefficient is inherently included here since the linear curve defines the lift coefficient at the linear departure angle of attack. The angle of attack of the post stall minimum lift coefficient typically occurs about six degrees beyond the stall angle of attack where the lift coefficient is from about 0.1 to 0.6 lower than the maximum lift coefficient depending on the type and thickness of the airfoil [111, 112]. Limited high angle of attack experimental data is available, but an attempt should be made to make use of data that comes close to the type and thickness of airfoil used in the propeller blade.

After determining the three angles that define the stall regime and the corresponding lift coefficients the modeling of the behavior observed in Figure 3.6 can commence. The model needs to behave like a cubic function that: a) matches the slope and lift coefficient value at the linear departure angle of attack, b) have a zero slope and lift coefficient equal to the maximum lift coefficient at the stall angle of attack, and c) have a zero slope and matching lift coefficient at the post stall minimum point. Thus six constraints are placed on the model curve. In order to define a function that meets the six constraints a 5^{th} order polynomial is used. Using a quintic equation does bring about the possibility that the curve may not behave like a cubic function, exhibiting oscillations in between the constrained points. This issue can be circumvented though

if the switchover from the linear curve to the quintic occurs at least five degrees before the stall angle of attack. Switching to the quintic earlier than the actual linear departure angle does not affect the accuracy of the model as can be seen in Figure 3.7. The full lift coefficient model applied to different airfoils is shown in this figure along with experimental data. Examining the plot for the NACA 0009 airfoil a slight steepening of the slope can be seen to occur five degrees before the stall angle of attack, but the experimental data is still matched very closely.

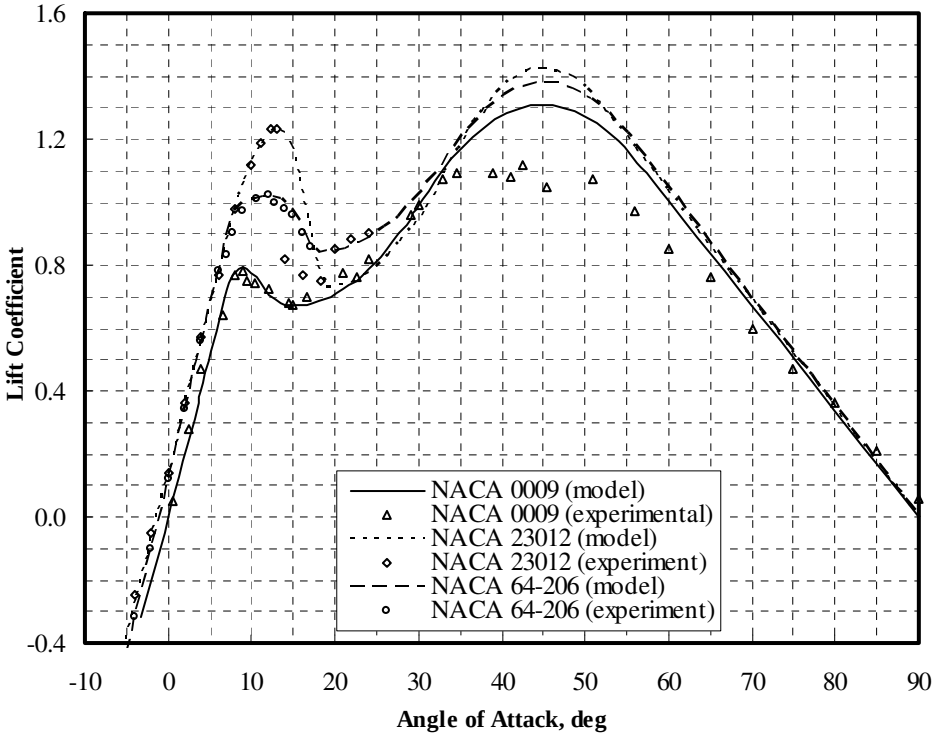

Figure 3.7. Experimental and modeled lift coefficient behavior.

The third segment of the model goes from the post stall minimum up to the inflection point at α_4 and is modeled by a quadratic curve. This curve matches the slope and lift coefficient at the post stall minimum and a prescribed lift coefficient value at the inflection point. Generally the inflection point occurs between 30 to 35 degrees angle of attack. The lift coefficient associated with this point is determined from high angle of attack experimental data. However, the exact lift coefficient value in the experimental data is not used but rather the increase in the

lift coefficient from the post stall minimum. This makes the model adaptable to airfoils of different camber. A second quadratic curve fits the behavior around the secondary maximum. This curve is defined so that it matches the slope and value of the preceding quadratic curve at the inflection point and has a zero slope at a 45 degree angle of attack. This second quadratic curve does not match the lift coefficient value at 45 degrees. The reason is that propeller elements do not regularly operate at such high angles of attack and modeling of the behavior is therefore considered to be of greater importance than matching the exact values. The final segment of the model is a straight line that passes through the abscissa at 90 degrees. The angle at which the switchover occurs is a variable that is determined so that the final straight line segment is tangent to the preceding quadratic curve.

Examples of this model applied to NACA 0009, NACA 23012, and NACA 64-206 airfoils are shown in Figure 3.7 along with experimental data. The data shown for the NACA 0009 airfoil was taken from reference [111], and those for the other two airfoils from reference [109].

Drag Model

The drag coefficient of an airfoil is highly dependent on the nature of the boundary layer and the chord-wise location where it transitions from laminar to turbulent. NACA data typically shows the drag polar of a smooth airfoil, as well as for one where the boundary layer is tripped near the leading edge [109]. The difference in drag coefficient between these two cases is significant and raises the question as to how to treat the boundary layer on a propeller blade? Propeller blades operate in an unsteady loading environment due to angular inflow and could experience rather large variations in the angle of attack during a single revolution. The blades are also exposed to vibrations from the aircraft engine and gearbox which causes the blades

themselves to vibrate. These two factors will likely cause a laminar boundary layer to transition near the leading edge, so it is therefore assumed here that the boundary layer on a propeller blade is predominantly turbulent. When it comes to modeling, drag coefficient data for the cases of a tripped boundary layer would thus be most suitable. In the case where an airfoil analysis program is used to predict parameters, the boundary layer can be tripped at the leading edge.

Typical behavior of the drag coefficient with angle of attack is sketched in Figure 3.8. Around an angle of attack of zero degrees the drag coefficient is at its minimum, $C_{D,\min}$, and a maximum, $C_{D,\max}$, occurs at 90 degrees. The value of the minimum drag coefficient depends on the airfoil shape as well as the nature of the boundary layer; the maximum depends on the type of airfoil. Reference [112] gives a table of the drag coefficients for a number of different airfoils at 90 degrees angle of attack.

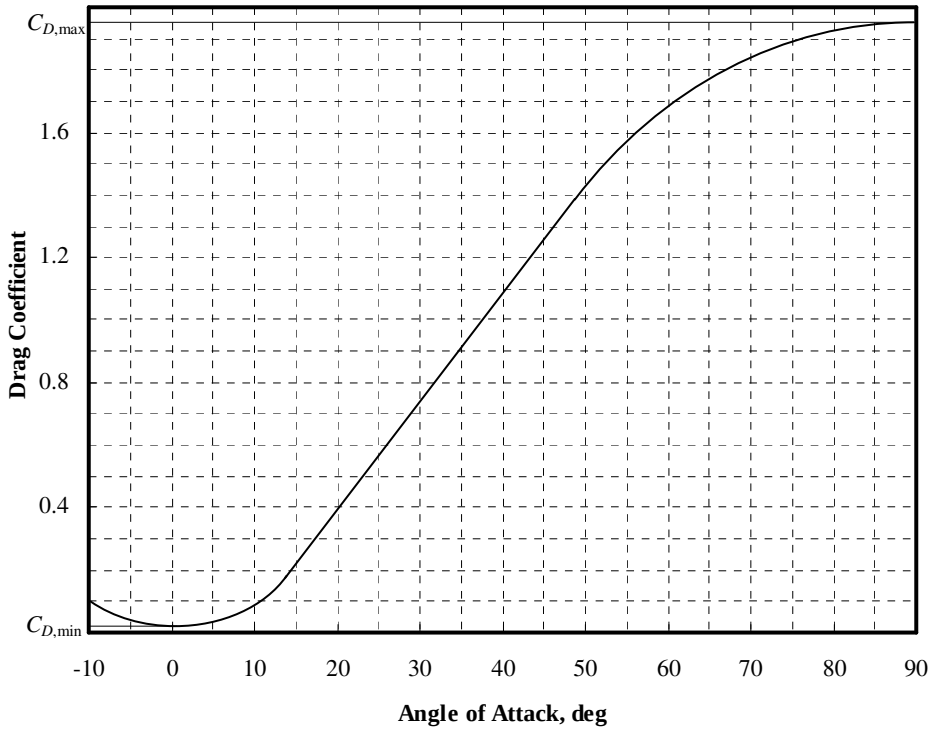

Figure 3.8. Sketch of drag coefficient behavior with angle of attack.

The drag coefficient curve has a parabolic shape in the neighborhood of both the minimum and maximum drag coefficients which suggests that two quadratic curves could be used to model the observed behavior. For low angles of attack, however, the 4th order equation given by equation (3.38) is used instead of a quadratic because it was found to model experimental drag data more closely.

$$C_D = 0.1\left[C_{L,\min C_D} - \left(A_1\alpha + A_2\right)\right]^4 + C_{D,\min} \tag{3.38}$$

The two constants, A_1 and A_2, are equal to the airfoil linear lift curve slope, $C_{L,\alpha}$, and ordinate intercept lift coefficient, $C_{L,0}$, respectively. These two constant are denoted by A_1 and A_2 because only at angles of attack below the linear departure angle can they be considered as the lift curve slope and zero angle of attack lift coefficient. At larger angles they are simply just constants that have no relation to the lift coefficient. The minimum drag coefficient and the minimum drag lift coefficient, $C_{L,\min CD}$, can be determined from experimental data or predicted by an airfoil analysis program. The minimum drag lift coefficient is typically equal to the coefficient of lift at zero degrees angle of attack [109]. Thus another possibility is to use the ordinate intercept lift coefficient for the minimum drag lift coefficient in equation (3.38).

With the low angle of attack drag coefficient accurately modeled, a quadratic equation may be used to model the remainder of the drag coefficient curve. The form of the suggested quadratic equation is as given by equation (3.39) which is a parabola centered at 90 degrees angle of attack with a value equal to the maximum drag coefficient.

$$C_D = A_3\left(\alpha - \frac{\pi}{2}\right)^2 + C_{D,\max} \tag{3.39}$$

This quadratic curve should transition smoothly from the low angle of attack 4th order model, thus the slopes and values of the two equations need to match at the transition point. This requirement gives two equations in terms of two unknowns, namely the angle of attack where the

model switches from the 4th order to the quadratic model, and the coefficient, A_3, in equation (3.39).

Examples of the drag coefficient model for the NACA 0009 and NACA 64-206 airfoils are shown in Figure 3.9. The full drag coefficient model for both airfoils is shown in Figure 3.9 (a) but, due to limited availability of high angle of attack data, only experimental results for the NACA 0009 airfoil is shown. In Figure 3.9 (b) the low angle of attack model for the NACA 64-206 airfoil is shown along with experimental data. The experimental data in this case comes from NACA airfoil data [109].

Compressibility Corrections to Incompressible Airfoil Data

Blade sections propeller tips operate at high subsonic Mach numbers, thus it is necessary to add corrections to the incompressible airfoil model to account for compressibility effects. Two of the most significant effects of compressibility are an increase in the lift coefficient with Mach number, and drag divergence. An additional effect related to drag divergence is a reduction in the stall angle of attack at higher subsonic Mach numbers; this is the Mach number effect on the stall angle of attack mentioned earlier. Even though shock-stall and drag divergence are related phenomena they can be treated separately. The reduction in the stall angle of attack at higher Mach numbers can be determined from experimental data such as published in references [113-116]. These references plot the lift coefficient as a function of the angle of attack for a variety of subsonic Mach numbers. From this data it is possible to tabulate the amount by which the stall angle of attack decreases at certain Mach numbers. In application then, this table can simply be interpolated to determine the amount by which the stall angle of attack decreases for each blade element. Since the shock-stall correction changes the stall angle of attack, it needs to be applied before generating the lift coefficient model described earlier.

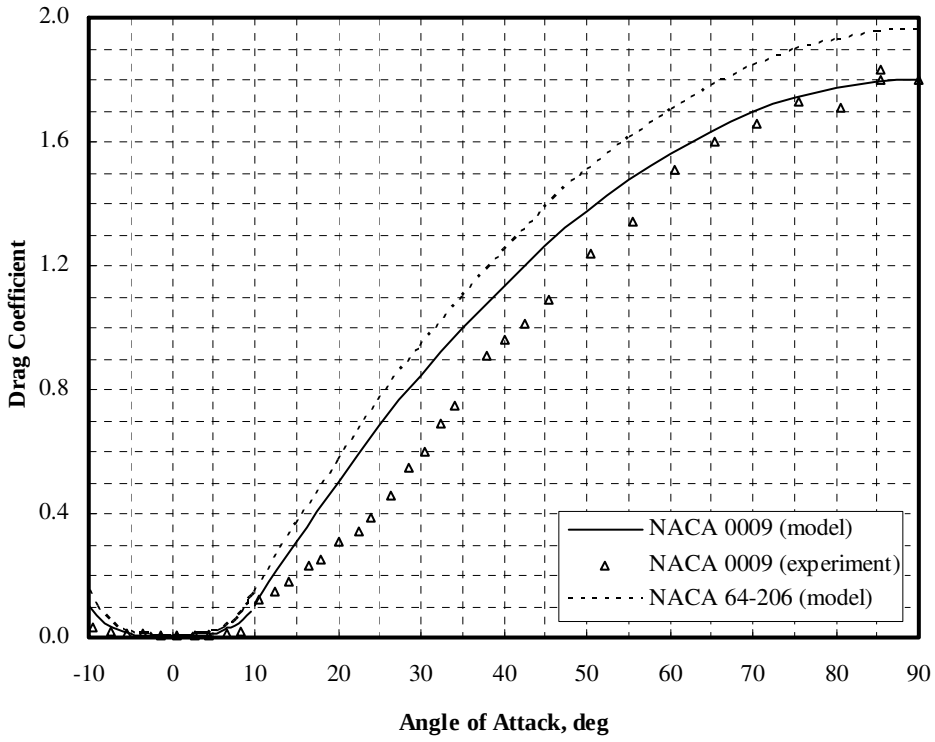

(a) Full model

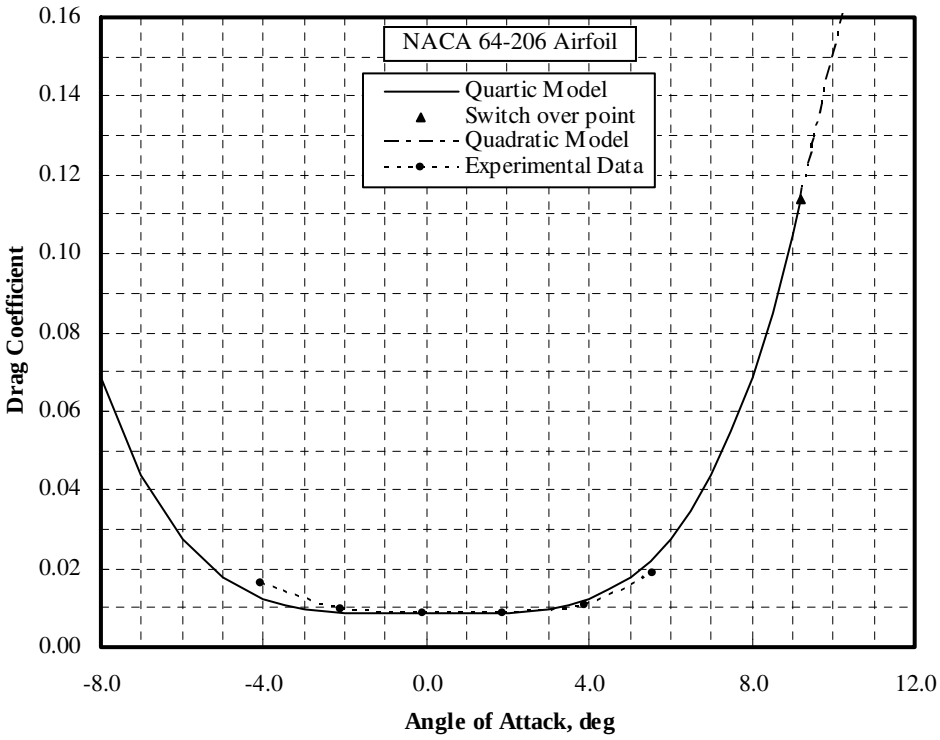

(b) Low α model

Figure 3.9. Experimental and modeled drag coefficient behavior

In order to account for drag divergence, it is necessary to first determine the drag divergence Mach number, M_{DD}. Equation (3.40), known as the Korn equation, predicts this value.

$$M_{DD} + \frac{C_L}{10} + \frac{t}{c} = \kappa \tag{3.40}$$

The factor κ is known as the airfoil technology factor. For advanced supercritical airfoils the technology factor value is $\kappa = 0.95$, and for NACA 6-series airfoils the value is $\kappa = 0.87$ [117, 118]. The drag divergence Mach number also depends on the thickness of the airfoil, t/c, and the lift coefficient. Thinner airfoils have higher drag divergence Mach numbers; a lower lift coefficient (i.e. lower angle of attack) also raises the drag divergence Mach number. The lift coefficient that appears in this equation is the compressibility corrected lift coefficient, C_{Lc}, which will be discussed below.

Equation (3.41) is a model for the increase in the drag coefficient beyond the drag divergence Mach number [119, 120].

$$C_{Dc} = C_{Di} + \nu\left(\frac{M - M_{DD}}{1 - M_{DD}}\right)^3 \tag{3.41}$$

This equation is only valid up to a Mach number of about one because beyond this Mach number the drag coefficient starts to decrease again. The factor ν in equation (3.41) has a value of 1.1 [120]. Figure 3.10 is a plot of the modeled behavior of the drag coefficient of a NACA 65-206 airfoil with Mach number at three different lift coefficients. Up to the drag divergence Mach number the drag coefficient is insensitive to the freestream velocity, but beyond the Mach number the drag coefficient increases by a significant amount.

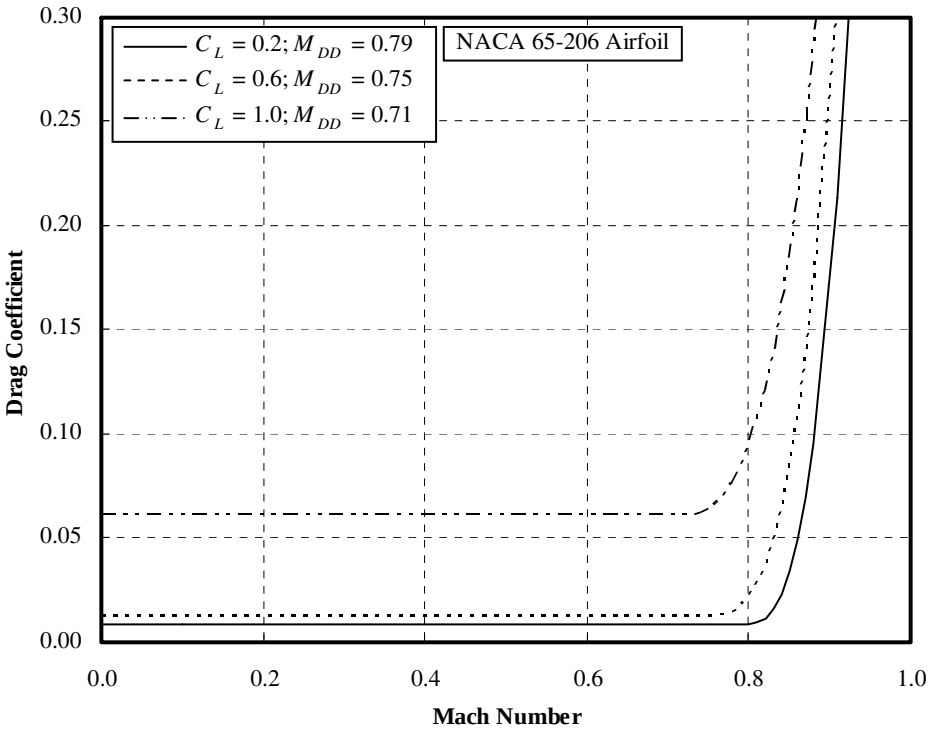

Figure 3.10. Example of the drag divergence model.

The final compressibility effect that should be added to an incompressible airfoil model is the increase in the lift coefficient with increasing Mach number. Two models are typically used for this, namely the Prandtl-Glauert correction, equation (3.42), or the Kaplan compressibility correction [121], equation (3.43).

$$\frac{C_{Lc}}{C_{Li}} = \frac{1}{\sqrt{1-M^2}} = \mu_{PG} \tag{3.42}$$

$$\frac{C_{Lc}}{C_{Li}} = \mu_{PG} + \frac{t/c}{1+t/c}\left[\mu_{PG}\left(\mu_{PG}-1\right) + \frac{1}{4}\left(\gamma+1\right)\left(\mu_{PG}^2-1\right)^2\right] = \mu_K \tag{3.43}$$

The Prandtl-Glauert correction does not account for the thickness of an airfoil and this is thus the extension introduced by Kaplan [121]. Both the Prandtl-Glauert and Kaplan correction have the effect of multiplying the incompressible lift curve slope by a factor, which is the recommended manner of implementation. This allows for the generating of the full lift coefficient model based on the increased lift curve slope predicted by either of the corrections.

Modeled behavior of the lift coefficient is plotted in Figure 3.11. The lift coefficient increases up to the drag divergence Mach number where, due to flow separation, the lift coefficient starts to decrease. This decrease in the lift coefficient beyond the drag divergence Mach number is given by equation (3.44). Here the Kaplan compressibility correction is shown in the equation, but if the Prandtl-Glauert correction is used, μ_K should simply be replaced by μ_{PG} in equation (3.44).

$$\frac{C_{Lc}}{C_{Li}} = \mu_K \frac{1 - M^2}{1 - M_{DD}^2} \tag{3.44}$$

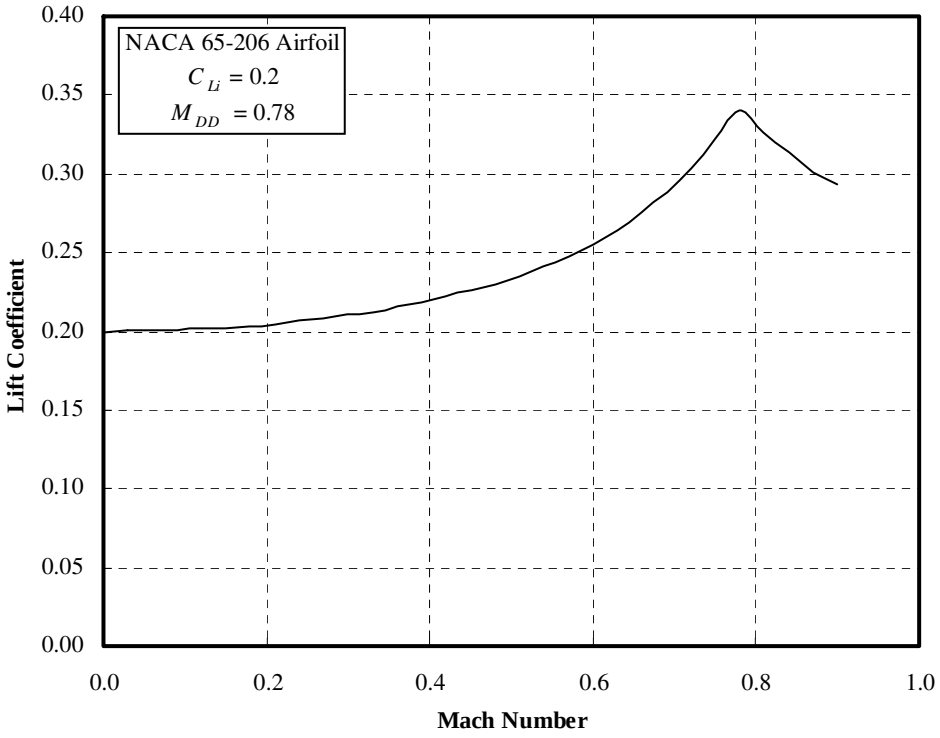

Figure 3.11. Modeled lift coefficient behavior with Mach number.

Airfoil Model Analysis

In concluding the discussion of the airfoil model, the effect of each additive element of the airfoil model on the performance results of a generic propeller will be considered. The case presented in Figure 3.12 is for a propeller that is operating at a helical tip Mach number, M_{ht}, of

0.8 with a blade angle at the 75% radial station equal to 30 degrees. Initially only a linear lift model was used in the performance prediction. This resulted in over-prediction of static thrust and an unrealistically high efficiency. Adding drag to the model brought the peak efficiency down considerably. It also had the clear effect of increasing the power coefficient at low advance ratios where the sections were operating at high angles of attack resulting in high drag values. Adding the stall model significantly altered the behavior of both the thrust and power coefficients at low advance ratios due to the reduced lift coefficient beyond the stall angle of attack. The reduction in stalling angle of attack due to shock-stall increased the advance ratio at which the thrust and power coefficient curves peaked and also decreased the magnitude of the peaks. The most significant effect of adding the Kaplan correction was a change in the slope of the thrust and power coefficient curves at advance ratios above their peak locations.

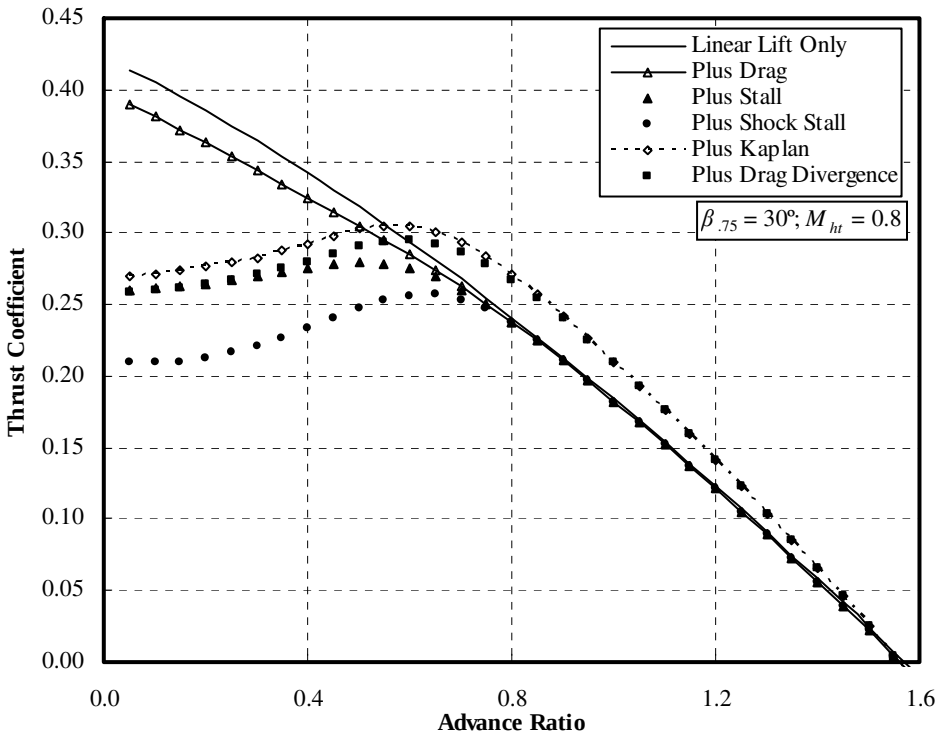

(a) C_T vs J

Figure 3.12. Additive effect of each feature of the airfoil model. (continued)

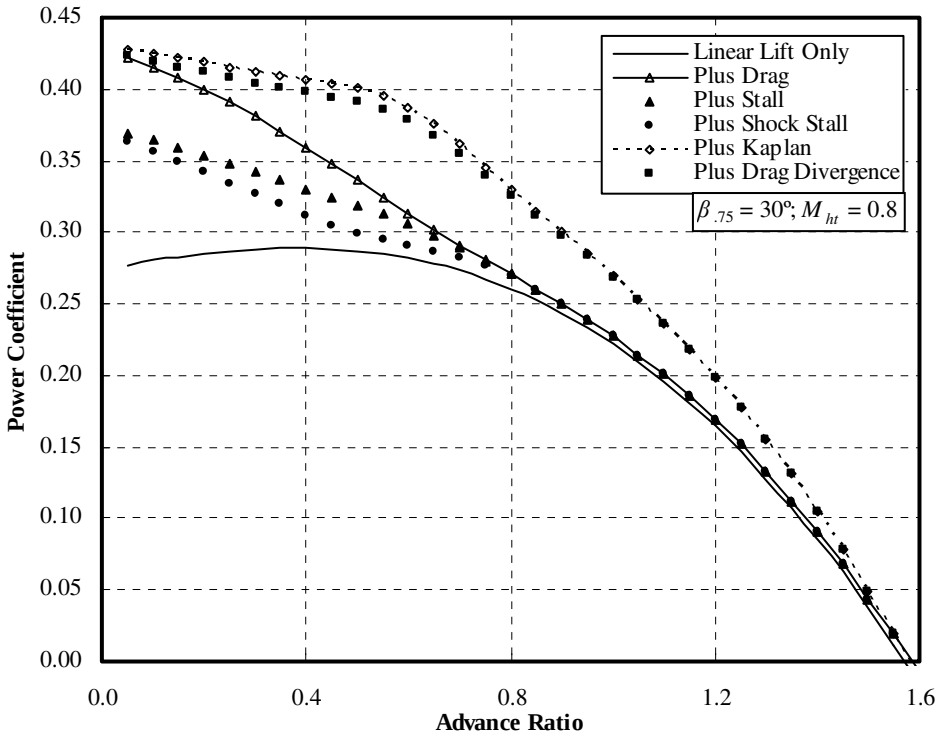

(b) C_P vs J

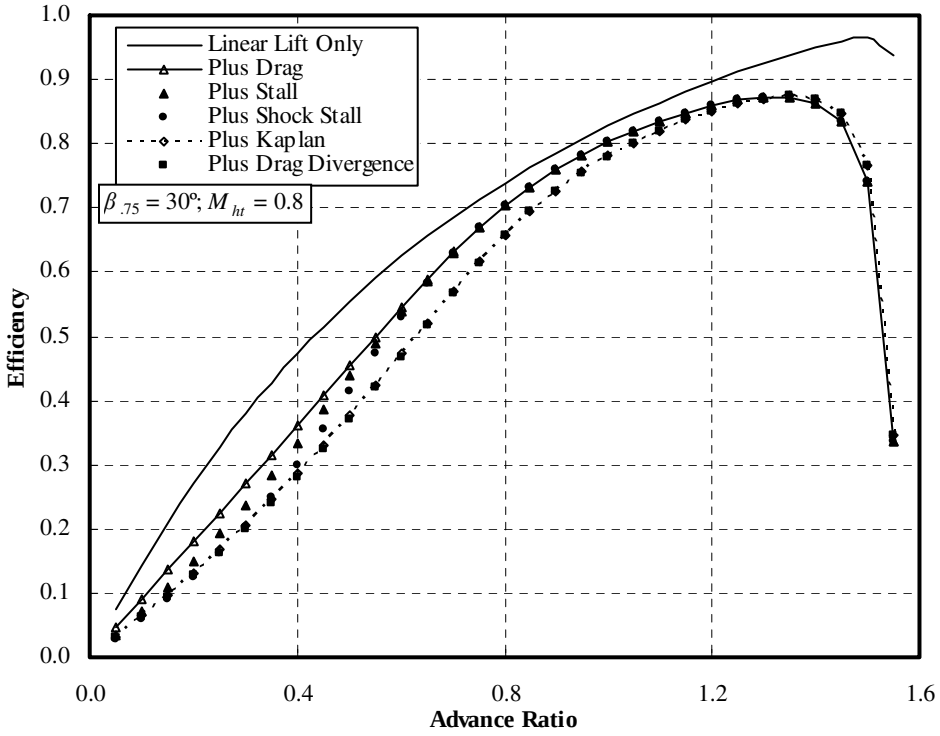

(c) η vs J

Figure 3.12. Additive effect of each feature of the airfoil model. (concluded)

This correction also increased the value of the peak thrust and power coefficients. Other than the addition of drag to the airfoil model, the Kaplan correction was the only effect that showed a clear influence on the efficiency. At low advance ratios this correction caused a reduction in the efficiency, but it did not significantly affect the peak efficiency. The final effect to add was the drag divergence, which resulted in a slight decrease in thrust and power, with no observable change in the efficiency plot. Again it is seen that efficiency is not very sensitive to errors or changes in the propeller model.

3.3 Model Validation

In this section results from the described propeller performance model will be compared against experimental data in order to validate the model. The experimental data used for the validation was published in NACA technical reports 1309 [122] and 1375 [123]. This section is thus divided into two subsections, one for each report. In each of the subsections the propeller geometry and available data will be described along with brief discussions of the application of the airfoil model for each case. A presentation and discussion of the results will close each subsection.

3.3.1 NACA Technical Report 1309

This report was published in 1957 with the objective of comparing the performances of propellers that were identical except for the blade camber (section design lift coefficients). Three different cambers were compared but detailed performance data for only one propeller was given in the report. This 10-ft diameter two-bladed propeller, the NACA 10-(10)(08)-03, was used for the comparison. Figure 3.13 is a plot of the radial distribution of the blade thickness, chord length, design lift coefficient, and blade twist angle for this propeller. This information was included in TR-1309. In this plot one-tenth of the design lift coefficient was plotted, the

blade thickness was normalized with the chord length, *t*/*c*, and the chord length was normalized with the propeller diameter, *c*/*D*.

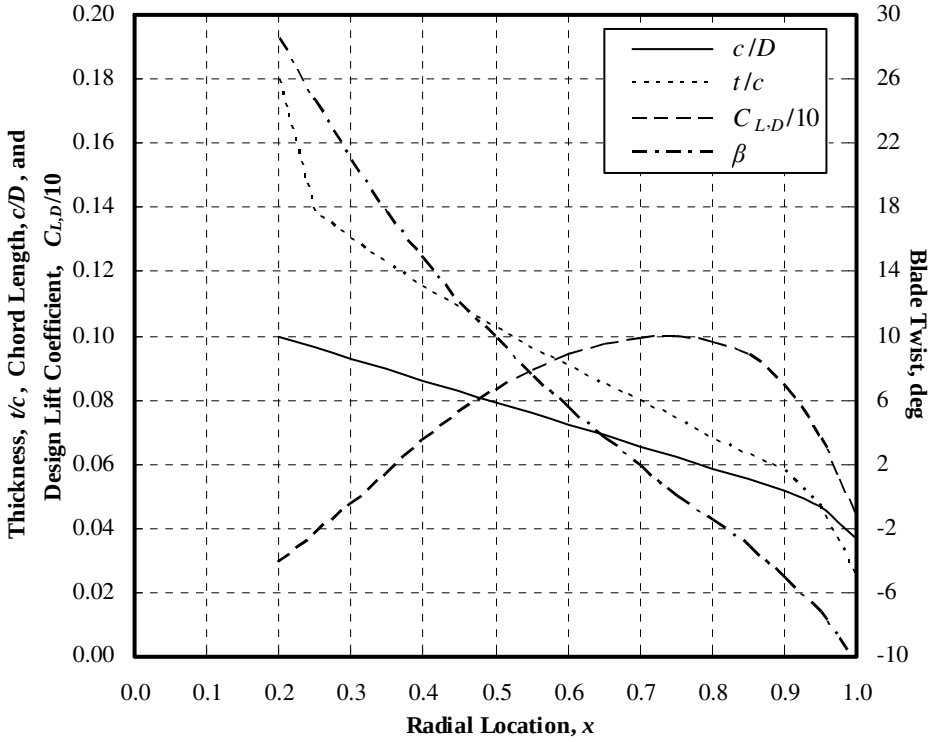

Figure 3.13. Geometry of NACA 10-(10)(08)-03 propeller.

The airfoil used in this propeller was the NACA 16-series airfoil. The thickness and camber of the 16-series airfoil is defined by equations (3.45) and (3.46) [124].

$$y_t = \begin{cases} \pm\dfrac{t}{c}\left(0.989665\sqrt{x} - 0.23925x - 0.041x^2 - 0.5594x^3\right), & x \le 0.5 \\ \pm\dfrac{t}{c}\left[0.01 + 2.325(1-x) - 3.42(1-x)^2 + 1.46(1-x)^3\right], & x \ge 0.5 \end{cases} \tag{3.45}$$

$$y_c = -0.079577 C_{L,D}\left[x\ln x + (1-x)\ln(1-x)\right] \tag{3.46}$$

In these equations y_t represents the non-dimensional coordinate perpendicular to the airfoil chord, x is the non-dimensional chord-wise coordinate, and y_c is the offset of the camber line from the chord-line in fractions of the section chord. By using the thickness and design lift coefficient from Figure 3.13 along with Equations (3.45) and (3.46) airfoil coordinates were

generated at a number of stations along the blade. The linear portion of the described lift coefficient model was generated by making use of XFOIL to predict the lift curve slope and ordinate intercept. XFOIL was also used to obtain the minimum drag coefficient and the lift coefficient coincident with the minimum drag. In order to justify the use of XFOIL, Table 3.1 was generated to compare its results to experimentally determined values. The results were reasonably close, and since no experimental airfoil data exactly matched the thickness and camber of the airfoils used in the propeller, XFOIL results had to be used.

TABLE 3.1

COMPARISON OF EXPERIMENTAL DATA AND XFOIL PREDICTIONS

Airfoil	$C_{L,\alpha}$ (1/rad)		$C_{L,0}$		$C_{D,\min}$	
	NACA	XFOIL	NACA	XFOIL	NACA	XFOIL
NACA 65-206	6.1	6.3	0.15	0.17	0.0085	0.0078
NACA 65-210	6.2	6.4	0.19	0.16	0.0091	0.0085
NACA 23012	6.1	6.4	0.13	0.13	0.0099	0.0092
NACA 23018	6.0	6.2	0.12	0.10	0.0105	0.0106

Performance data for the NACA 16-series airfoil published in references [124] and [125] were used to assemble a table of stalling angles of attack as a function of airfoil thickness. These documents were also used to tabulate shock-stall data for the 16-series airfoil. Data published in references [111] and [112] was used to define the critical points beyond the stall angle of attack as described in the previous section. The Kaplan compressibility correction to the lift coefficient was used for this case.

The propeller performance data published in NACA Technical Report 1309 [122] included the thrust and power coefficients and the efficiency in graphical form plotted as functions of the advance ratio and the blade pitch angle at the $0.75R$ radial location, $\beta_{.75}$. The data was generated by setting the blade pitch to a desired angle and running the propeller at a fixed angular speed over a range of forward speeds. Tests were done at three different angular

speeds, namely 1140 RPM, 1350 RPM, and 1600 RPM. For each forward speed/RPM combination (advance ratio) the thrust and power were recorded. This was done over a range of forward speeds until the thrust and power dropped below zero. The blade pitch angle was then adjusted to a different value and the test was repeated. The blade angles were varied from 20 to 55 degrees in 5 degree increments, and the propeller was run at wind tunnel speeds of up to 500 mph (223.5 m/s).

The validation results are shown in three figure groups, one group for each angular speed. In Figure 3.14 the thrust coefficient, power coefficient, and efficiency for the 1140 RPM case are shown. The lines show the predicted results whereas the symbols are the experimental values.

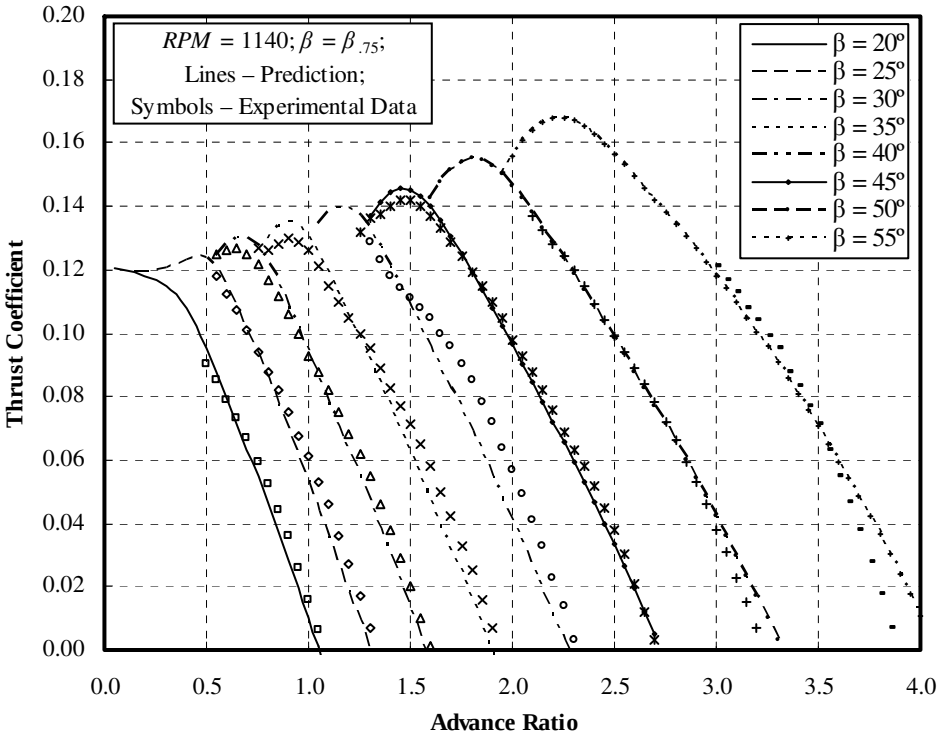

(a) C_T vs J

Figure 3.14. Comparison of prediction with NACA TR-1309, 1140 RPM. (continued)

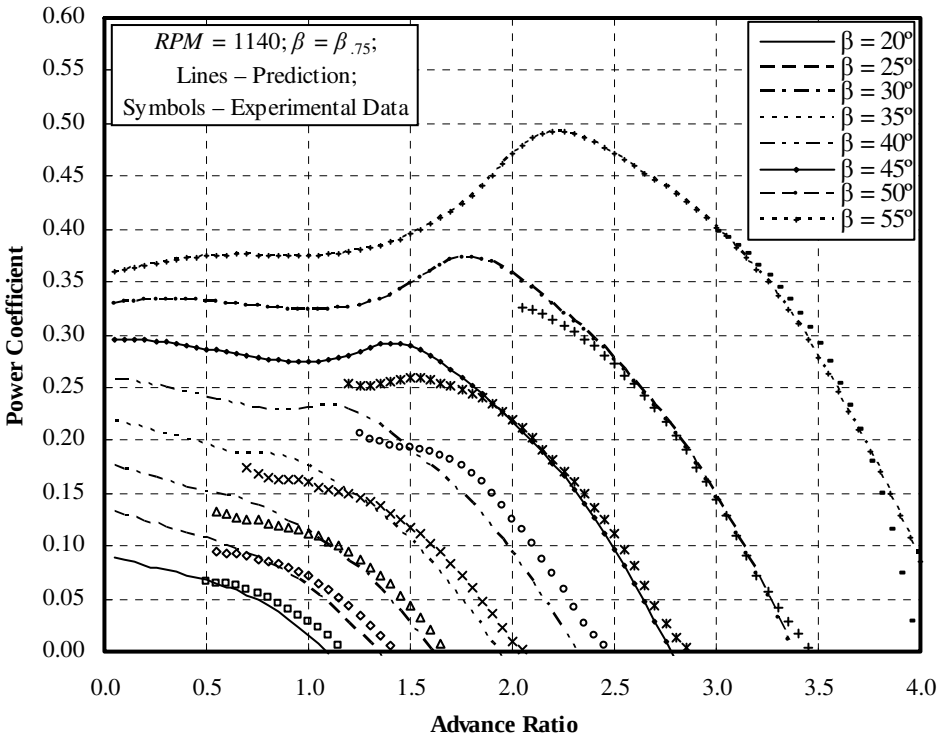

(b) C_P vs J

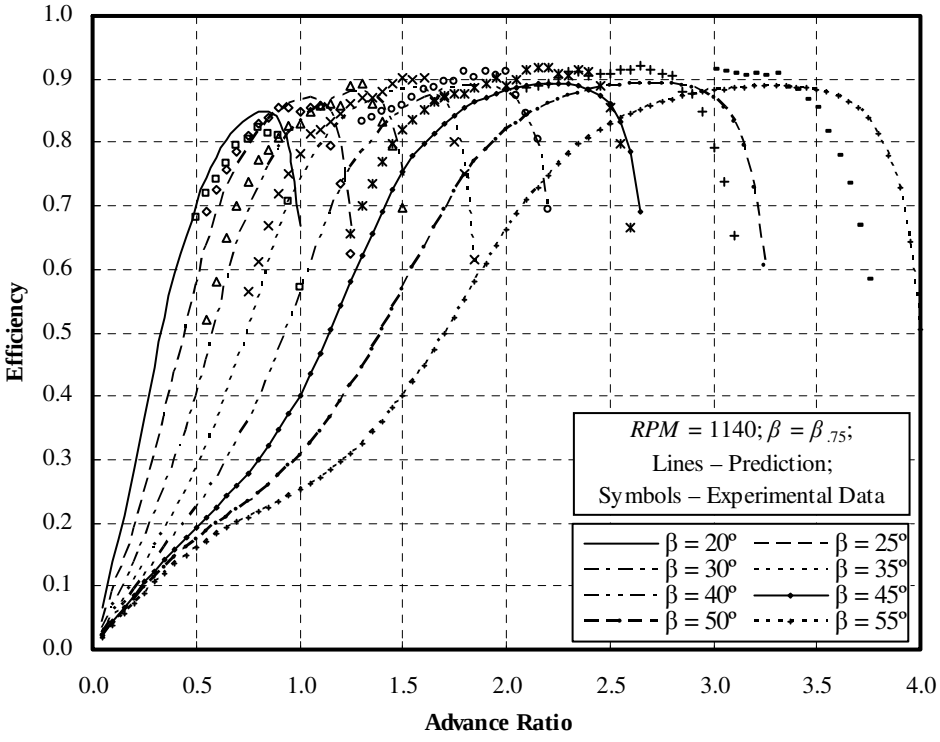

(c) η vs J

Figure 3.14. Comparison of prediction with NACA TR-1309, 1140 RPM. (concluded)

Overall the agreement of the predictions with the experimental data was very good. The predictions captured the trends exhibited by the experimental data and also agreed closely with the values. Examining the thrust coefficient, Figure 3.14 (a), it can be seen that the advance ratios at which the respective curves for each blade angle peaked were well predicted. This suggests that the stall model accurately represented the actual stall behavior of the airfoil.

For some blade angles the experimental data showed a slight sway from the continuous decrease in the predicted thrust coefficient with increasing advance ratio. This can be seen for the 35 and 40 degree blade pitch angle cases. The reason for this is believed to be an observed nonlinear behavior of the lift coefficient of the 16-series airfoil below the stall angle of attack [125]. This nonlinear behavior was not present for all combinations of airfoil thickness and flow condition and so it was not captured by the general airfoil model presented in this chapter.

The power coefficient, Figure 3.14 (b), showed the same qualitative agreements between the predictions and experiment as was seen for the thrust coefficient. The model captured the trends, locations of peaks, and actual values with acceptable accuracy. Another important observation from the thrust and power coefficient plots was that the change in the dependent variable due to changes in blade angle was well captured. Since the performance model is to be used in a twist optimization study it has to be sensitive to changes in the blade twist. Capturing the effect of changes in the blade pitch angle is thus an important consideration in evaluating the validation results.

Finally the efficiency, presented in Figure 3.14 (c), showed that the trends were well captured again. The predicted peak efficiency was consistently below the experimental values and did not match the location of the peak for every case. It needs to be noted, however, that efficiency is a combination of the thrust and power coefficient, and as such, often exaggerates

errors in the thrust and power predictions. Still, the efficiency predictions were close to the true experimental values.

For the next angular speed case of 1350 RPM, the results of which are shown in Figure 3.15, much the same trends and close agreement with the experimental data was observed. In fact, for the majority of the blade pitch angles the agreement was better than for the previous case. At high advance ratios for the 50 degree blade pitch angle case it can be seen that the predictions started to diverge from the experimental results. This departure started at an advance ratio of about 2.85 where the helical tip Mach number was roughly equal to 0.85. Many of the compressibility corrections are asymptotic at sonic speeds and become invalid as the Mach number approaches unity.

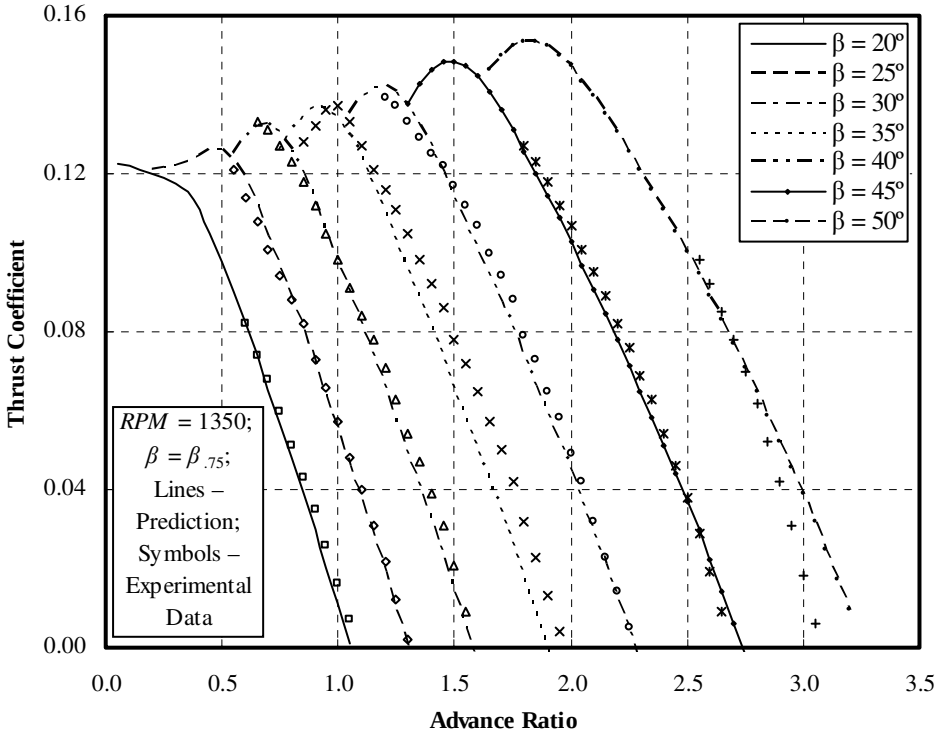

(a) C_T vs J

Figure 3.15. Comparison of prediction with NACA TR-1309, 1350 RPM. (continued)

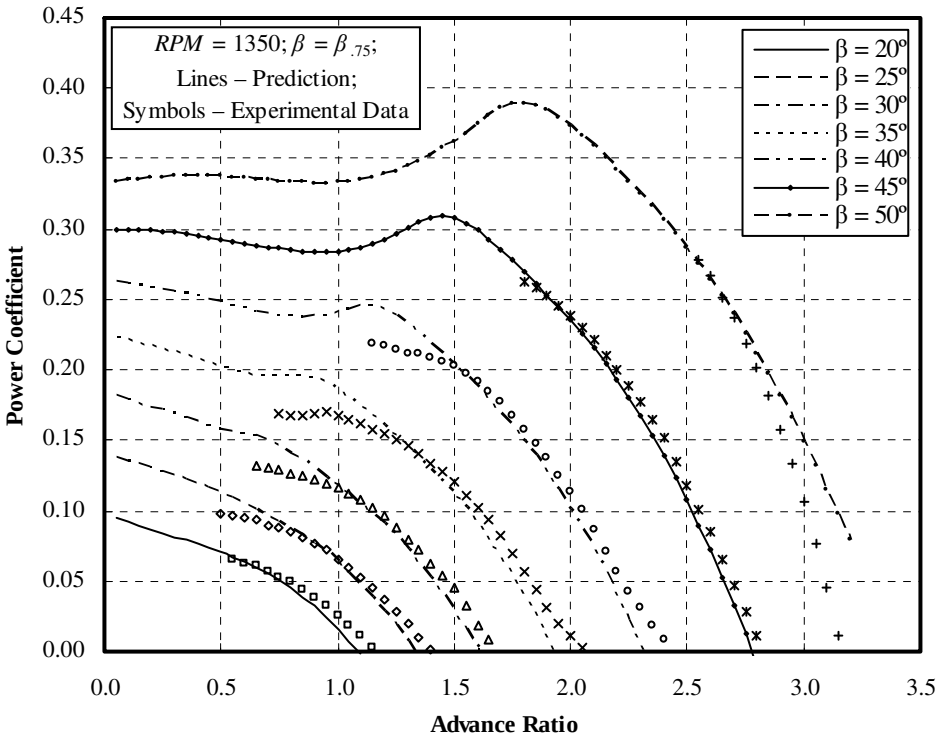

(b) C_P vs J

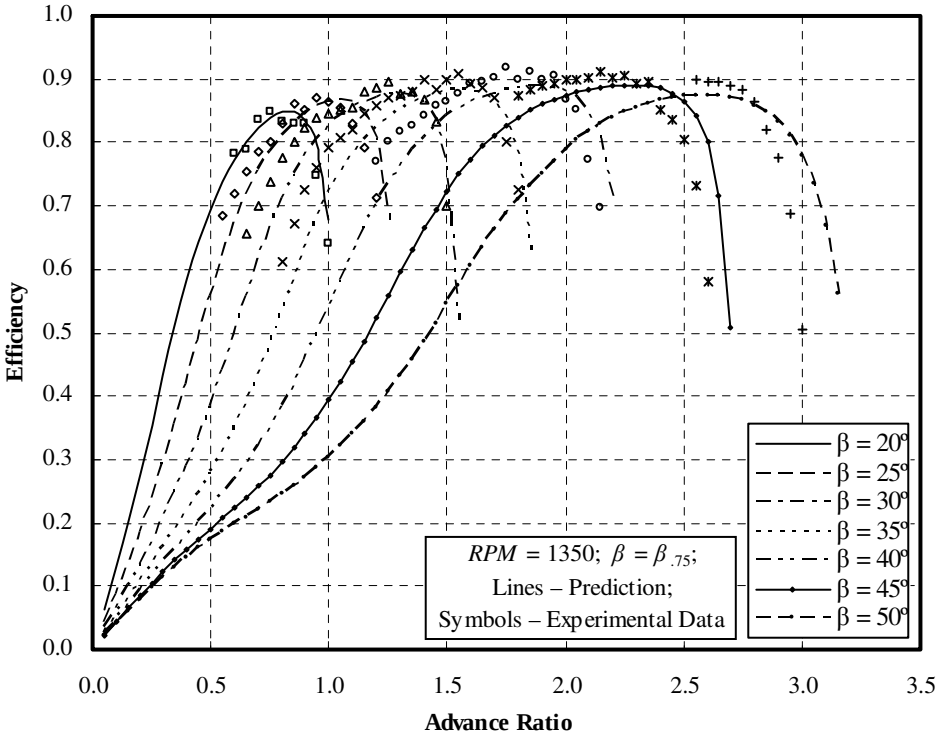

(c) η vs J

Figure 3.15. Comparison of prediction with NACA TR-1309, 1350 RPM. (concluded)

Though the exact Mach number at which the corrections become invalid is not clear, it is believed that the increasing disagreement between prediction and experiment at higher advance ratios was a result of the compressibility corrections being used beyond the valid Mach number ranges.

The final group of plots is for the 1600 RPM case. Excellent agreement between experiment and prediction at the lower advance ratios is observed in Figure 3.16. For the 30-degree blade angle case the predicted advance ratio at which the thrust coefficient peaked did not agree with the experimental data. The reason for this is not clear since the model accurately captured the blade stall angle when it was operated at lower angular speeds. At high advance ratios it can again be seen that the predictions became worse.

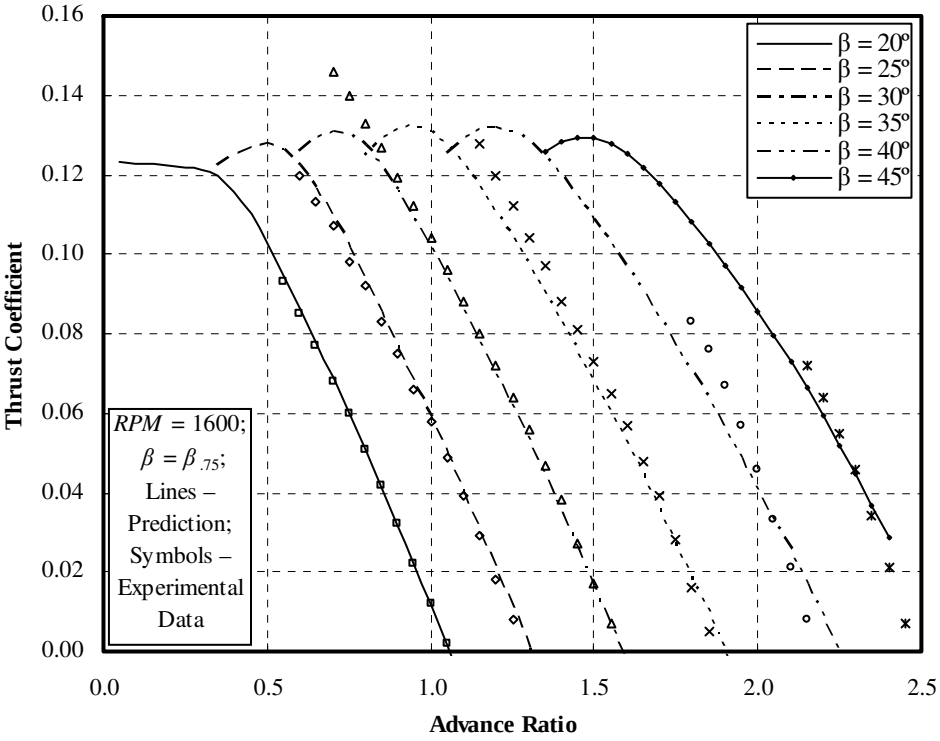

(a) C_T vs J

Figure 3.16. Comparison of predictions with NACA TR-1309, 1600 RPM. (continued)

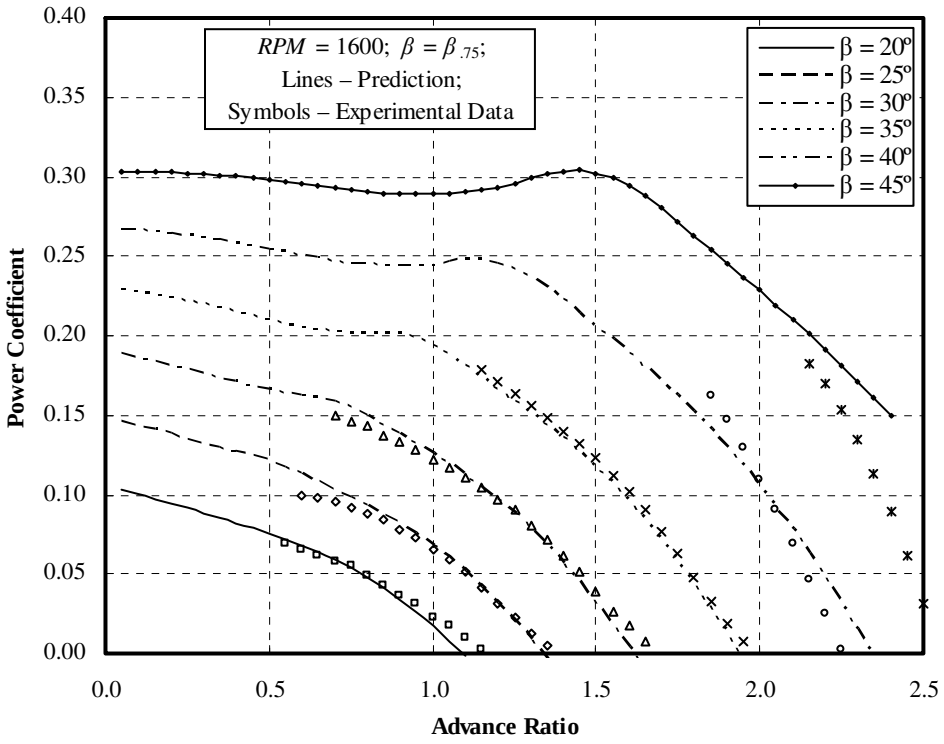

(b) C_P vs J

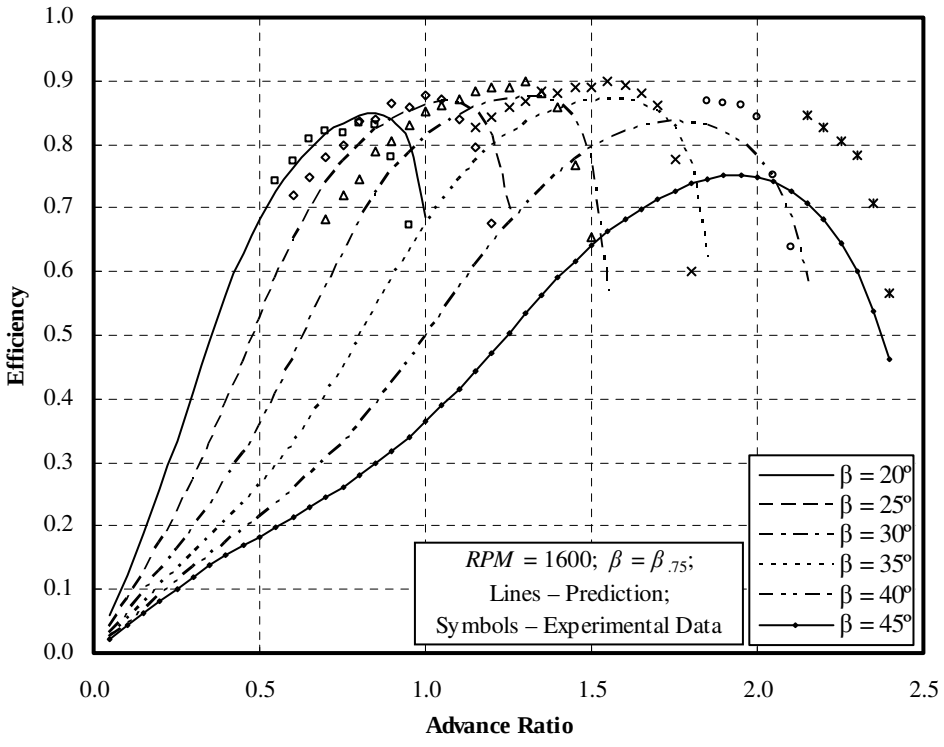

(c) η vs J

Figure 3.16. Comparison of predictions with NACA TR-1309, 1600 RPM. (concluded)

At 1600 RPM the helical tip Mach number was greater than 0.85 at advance ratios greater than 1.7. The disagreement in the 40 and 45 degree pitch angle cases is thus believed to be due to the breakdown of the compressibility corrections. The errors in the thrust and power coefficients at higher advance ratios are clearly visible in the efficiency plot where the errors are amplified.

3.3.2 NACA Technical Report 1375

The propeller performance data in TR-1375 was generated in order to investigate the aerodynamic characteristics of a full scale propeller at forward speeds of up to Mach number of 0.96. At such high Mach numbers the propeller tip speeds would be supersonic and the predictions would thus be invalid. However, this report included performance maps over a full range of advance ratios. Therefore, comparisons were made for the cases where the helical tip Mach numbers were less than one.

The propeller investigated in TR-1375 was 3-bladed with a 9.75 ft diameter and constant chord blades. The thickness, chord length, and blade twist distributions are shown in Figure 3.17. The propeller blade airfoil was again the NACA 16-series, except these airfoils were all symmetrical. Using the thicknesses shown in Figure 3.17 along with equation (3.45) the airfoil coordinates at a number of radial stations were generated. XFOIL was again used to define the linear portion of the lift coefficient model as well as to determine the minimum drag and coincident lift coefficient. The stall angle and shock stall tables discussed in the previous subsection for the 16-series airfoil were reused for this propeller.

The performance data in TR-1375 was generated at a single angular speed of 1600 RPM, and the blade pitch angle was varied from 20.2 to 50.8 degrees. The prediction results plotted along with the experimental performance numbers are shown in Figure 3.18.

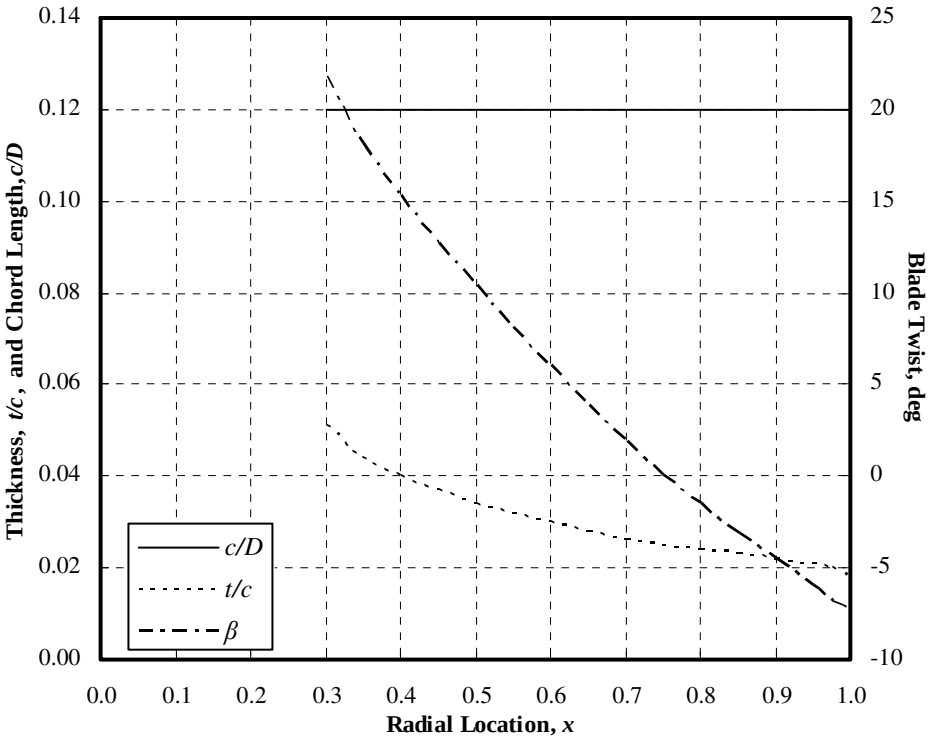

Figure 3.17. Propeller geometry, NACA TR-1375.

For blade angles of 40.2 degrees and below, and advance ratios of less than 2.0, the thrust coefficient predictions matched the experimental data very closely. The 45.4 degree pitch angle case also agreed well with the experimental data except for some over-predicted thrust coefficient values at lower advance ratios. The power coefficients were also accurately predicted for blade pitch angles of 45.4 degrees and below. The slightly over-predicted thrust and power coefficients for the 45.4 degree case resulted in a significant under prediction of efficiencies, but for smaller blade angles the results matched the experimental efficiencies closely.

For the largest blade angle the experimental data was not well predicted. The thrust of the largest blade angle case was under-predicted, and the slope of the power coefficient curve at high advance ratios was shallower than that seen in the experimental data. Again, the reason for this poor prediction is believed to be the compressibility corrections being used beyond their valid Mach number ranges.

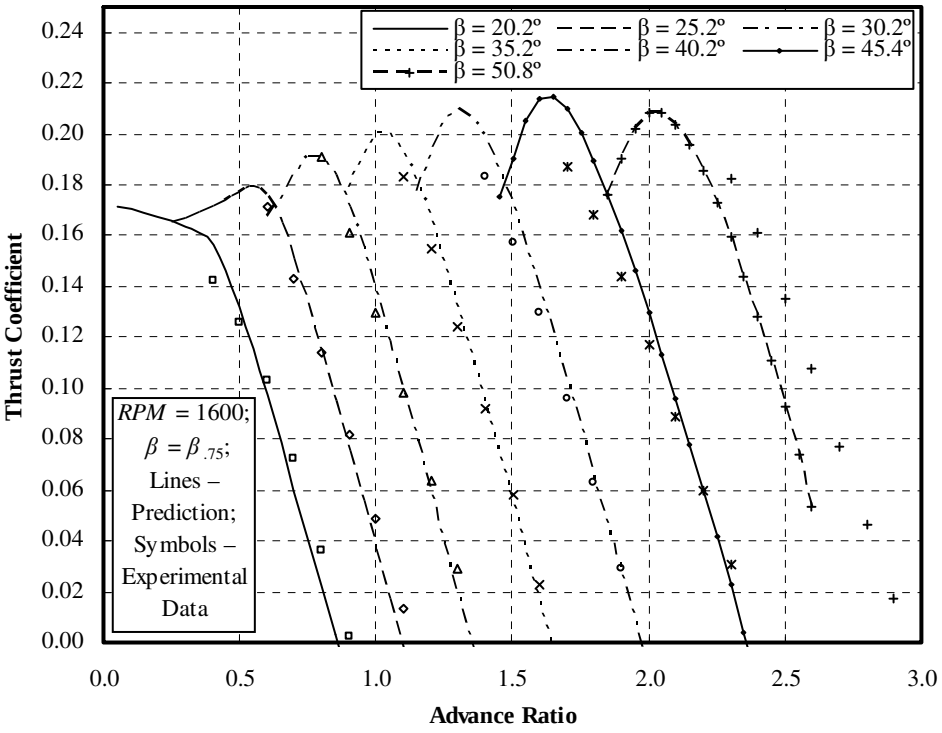

(a) C_T vs J

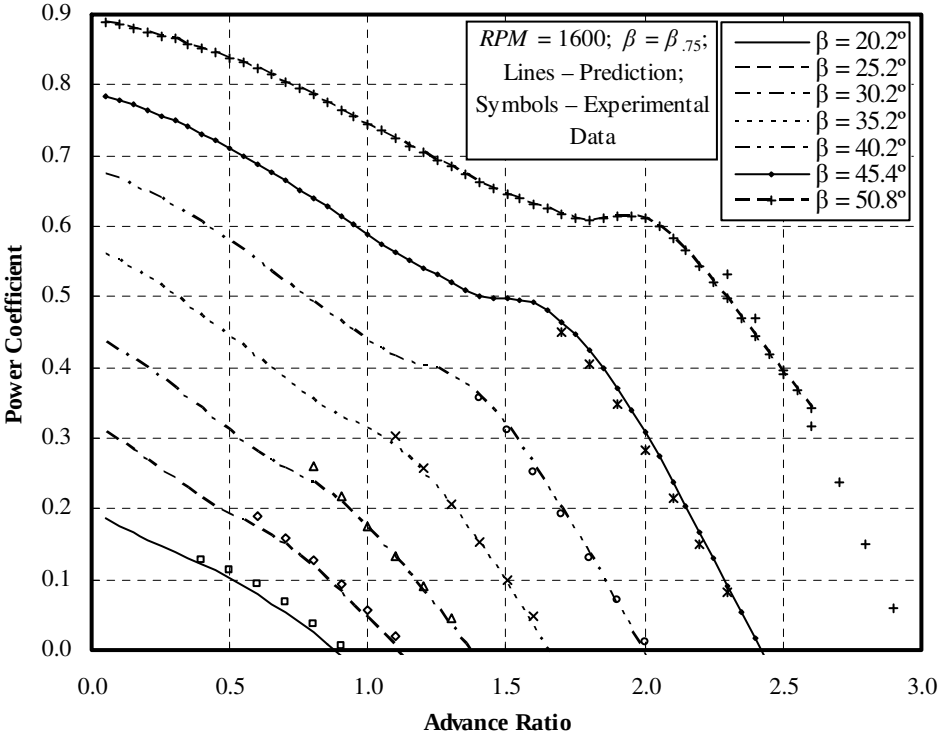

(b) C_P vs J

Figure 3.18. Comparison of predictions with NACA TR-1375. (continued)

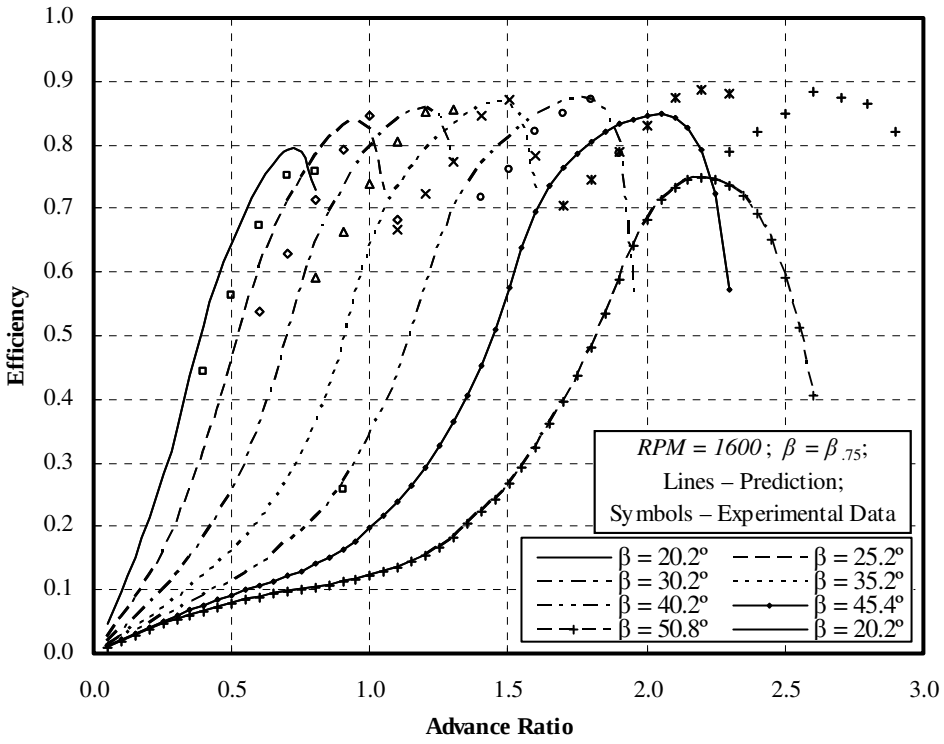

(c) η vs J

Figure 3.18. Comparison of predictions with NACA TR-1375. (concluded)

This can also explain the error in the 45.4 degree case. Considering this result as well as those presented in the previous subsection, it has to be concluded that the model presented here is limited to helical tip Mach numbers of less than 0.9.

In reviewing all the results presented here, it can be concluded that the propeller aerodynamic model has been validated. Over the majority of advance ratios the predictions agreed very closely with the experimental data. However, a limitation of the model has been discovered. The limitation is due to the breakdown of the compressibility corrections at high subsonic Mach numbers. The validity of this model is thus limited to helical tip Mach numbers of less than 0.9.

Another important consideration in reviewing the results is the intended application of the performance model. This model is to be used in a blade twist optimization study. The

performance predictions therefore need to be sensitive to changes in the blade twist. One way to assess this sensitivity is to look at the accuracy with which changes in the blade pitch angle was predicted. This was already discussed in the previous subsection where it was concluded that the model does capture these changes. The other way to assess the sensitivity is to compare the results between the two different propellers since each propeller had a different twist distribution. Again, the model predicted the experimental data closely for both propellers, so it can be concluded that the model is indeed sensitive to changes in blade twist and is thus valid for twist optimization.

A final point to consider is the small amount of error that was present in the prediction results as compared to experiment. The efficiency prediction, for example, differed by more than 5% from experiment for many cases and raises the question as to whether the aerodynamic model would be able to capture differences in efficiency between different propellers of less than 5%. Upon closer investigation of the prediction results it is observed that the error offset is consistent for the various blade pitch angles. It should be reiterated that the change in thrust or power coefficient, or efficiency, due to a change in blade pitch angle or advance ratio is accurately predicted. Thus the point that is of greater importance is that, though the model is not exactly precise, the error is consistent and therefore the differences between propellers can be accurately predicted.

3.4 Chapter Summary

This chapter dealt with the propeller aerodynamic model. The blade element method was introduced in the first part of this chapter along with the vortex theory which is needed to determine the induced velocities at each blade element. In using the blade element method it was found that the accuracy of performance calculations was highly dependent on the accuracy

of the airfoil characteristics. Thus much time was devoted to developing an airfoil model that included a variety of features. These attributes included a full stall model that included variations in stall angle of attack due to thickness and section Mach number, post stall behavior up to 90 degrees angle of attack, compressibility effects on lift coefficient, drag divergence, section specific lift curve slopes and ordinate intercepts, and a full drag model. It was attempted to make the model as accurate as possible using published experimental airfoil data. Good agreement between the results and experimental data validated the model and showed it to be suitable for an optimization study.

CHAPTER 4

PROPELLER TWIST OPTIMIZATION

4.1 Introduction

The derivation and implementation of propeller twist optimization routines are covered in this chapter. Calculus of variations is used to arrive at expressions that give an optimized blade twist at specific operating conditions. The first section of this chapter is devoted to some of the basic concepts of calculus of variations in order to apply the method in the following section where expressions for the optimum blade twist are derived. Careful attention is given to the various derivatives that appear in the calculus of variations result. Once the optimization formulas are obtained, the method of implementation on a desktop computer is discussed and validated. The results presented in the final section of this chapter include both unconstrained and constrained twist optimization. The ultimate purpose for performing the twist optimization study on propeller blades is to gauge the feasibility of a variable blade twist, and identify a mission profile that would suit such a technology. It will be shown that an aircraft that has a mission profile of prolonged loitering intermixed with high speed dash phases could benefit from a variable twist propeller. An analysis of such a mission profile concludes this chapter.

4.2 Calculus of Variations

The fundamental problem of calculus of variations is to determine the function, $y(x)$, that will cause the functional, F, to be an extremum (maximum or minimum) [126, 127]. A general definition of the functional is given by equation (4.1), where the prime denotes differentiation with respect to the independent variable, x.

$$F = \int_{x_1}^{x_2} f\left[x, y(x), y'(x)\right]dx \tag{4.1}$$

The function, $y(x)$, is subject to the end boundary conditions given by equation (4.2).

$$\begin{aligned} y(x_1) &= y_1 \\ y(x_2) &= y_2 \end{aligned} \tag{4.2}$$

In order to derive the necessary condition for the function, $y(x)$, that will cause the functional, F, to be an extremum, it will be assumed that the function does extremize the functional. Now, if this function results in an extremum, any variation of this function should cause the functional to move away from the extremum. A new function, $Y(x)$, is thus introduced (equations (4.3) and (4.4)).

$$Y(x) = y(x) + \varepsilon\mu(x) \tag{4.3}$$

$$Y'(x) = y'(x) + \varepsilon\mu'(x) \tag{4.4}$$

The arbitrary auxiliary function, $\mu(x)$, which appears in equations (4.3) and (4.4) is defined so that it goes to zero at the end points (equation (4.5)), giving the new function, $Y(x)$, the same boundary conditions as the original function, $y(x)$.

$$\mu(x_1) = \mu(x_2) = 0 \tag{4.5}$$

The functional, $F(\varepsilon)$, written in terms of the new function, Y, is now as shown in equation (4.6).

$$F(\varepsilon) = \int_{x_1}^{x_2} f[x, Y(x), Y'(x)]dx \tag{4.6}$$

The extremum of this functional is obtained when the condition of equation (4.7) is met.

$$\left.\frac{\partial F(\varepsilon)}{\partial \varepsilon}\right|_{\varepsilon=0} = 0 \tag{4.7}$$

Differentiating equation (4.6) gives equation (4.8).

$$\left.\frac{\partial F(\varepsilon)}{\partial \varepsilon}\right|_{\varepsilon=0} = \int_{x_1}^{x_2} \left(\frac{\partial f}{\partial Y}\mu + \frac{\partial f}{\partial Y'}\mu' \right) dx = 0 \tag{4.8}$$

Equation (4.9) shows the result of integrating the second term of equation (4.8) by parts.

$$\int_{x_1}^{x_2} \frac{\partial f}{\partial Y'} \mu' \, dx = \frac{\partial f}{\partial Y'} \mu \Big|_{x_1}^{x_2} - \int_{x_1}^{x_2} \left(\frac{d}{dx} \frac{\partial f}{\partial Y'} \right) \mu dx \tag{4.9}$$

Since the arbitrary auxiliary function, $\mu(x)$, is equal to zero at the end points, the first term on the right hand side of equation (4.9) will be zero, and, subsequently, equation (4.10) is obtained.

$$\frac{\partial F(0)}{\partial \varepsilon} = \int_{x_1}^{x_2} \left(\frac{\partial f}{\partial y} - \frac{d}{dx} \frac{\partial f}{\partial y'} \right) \mu dx = 0 \tag{4.10}$$

Note that in equation (4.10) the perturbation parameter, ε, is set equal to zero, which is the reason for the new function, Y, being replaced by the original function, y. Since the auxiliary function, $\mu(x)$, is an arbitrary function of the independent variable, x, equation (4.10) only holds if the quantity within the parentheses under the integral sign equals zero. Thus the necessary condition for the functional to reach an extreme value is for the extemizing function, $y(x)$, to satisfy the Euler-Lagrange equation, equation (4.11).

$$\frac{\partial f}{\partial y} - \frac{d}{dx} \frac{\partial f}{\partial y'} = 0 \tag{4.11}$$

The Euler-Lagrange (E-L) equation derived above is for the case of a single dependent and independent variable with no constraint placed on the extremization. For the case where multiple dependent variables are present, it can easily be shown that for each additional dependent variable, an additional E-L equation has to be written. Thus each dependent variable needs to satisfy an E-L equation independently for the functional, F, to reach an extreme value.

The case of multiple independent variables requires slightly more discussion than the multiple dependent variable case. Consider, as an example, the case of three independent variables (x, y, z) with a single dependent variable, v. The functional is now defined as in equation (4.12) where v_x, v_y, and v_z are the derivatives of the dependent variable, v, with respect to x, y, and z, respectively.

$$F = \int_{x_1}^{x_2} f\left[x, y, z, v, v_x, v_y, v_z\right] dx \tag{4.12}$$

Following the same approach as for the single independent variable case, the E-L equation for this problem, equation (4.13), is obtained.

$$\frac{\partial f}{\partial v} - \frac{\partial}{\partial x}\frac{\partial f}{\partial v_x} - \frac{\partial}{\partial y}\frac{\partial f}{\partial v_y} - \frac{\partial}{\partial z}\frac{\partial f}{\partial v_z} = 0 \tag{4.13}$$

A constrained variational problem requires the extremizing function, $y(x)$ or $v(x,y,z)$, to satisfy some constraint equation. So it will likely be the case, depending on the nature of the constraint and the problem, that the constrained extremal will not be the absolute extreme value as would be determined by the unconstrained problem. The constrained extremal problem is defined as follows:

Determine the function, $y(x)$, that causes the functional,

$$F = \int_{x_1}^{x_2} f\left[x, y, y'\right] dx, \tag{4.14}$$

to be an extremum subject to the constraint that $y(x)$ also satisfy the condition,

$$H = \int_{x_1}^{x_2} h\left[x, y, y'\right] dx, \tag{4.15}$$

where H is a constant.

This problem is solved by making use of a Lagrange multiplier to form a new function, f_L, equation (4.16).

$$f_L = f - \lambda h \tag{4.16}$$

Thus the new functional, F_L, given by equation (4.17) is obtained for which the unconstrained extremum is to be determined, only now the solution of the E-L equation will give a function, $y(x)$, in terms of the Lagrange multiplier, λ.

$$F_L = \int_{x_1}^{x_2} f_L[x, y, y']dx \tag{4.17}$$

This Lagrange multiplier is solved so that the constraint equation (4.15) is satisfied.

4.3 Propeller Twist Optimization

In this section Calculus of Variations is applied to the equations for the thrust coefficient, power coefficient, and efficiency in order to derive equations that would give the optimum twist of a propeller blade. In the cases treated here the problem is to determine the twist function, $\beta(x)$, that will extremize either of the functionals, namely the thrust coefficient, the power coefficient, or the efficiency. The independent variable, x, is the non-dimensional radial position.

4.3.1 Unconstrained Optimization

The problem statement for the unconstrained twist optimization problem is as follows: Determine the propeller twist distribution, $\beta(x)$, that maximizes the efficiency, η, defined by equation (4.18).

$$\eta = \frac{JC_T}{C_P} = \frac{J\int_{x_{hub}}^{1} T_c(x, \beta(x))dx}{\int_{x_{hub}}^{1} P_c(x, \beta(x))dx} \tag{4.18}$$

Note that neither the thrust nor the power coefficient, defined by equations (3.12) and (3.19) respectively, depends on the derivative of the twist function, β. This simplifies the problem considerably. In order to derive the Euler-Lagrange equation for this problem a new function, $\beta_\varepsilon(x)$, defined in equation (4.19), is introduced to arrive at equation (4.20).The arbitrary auxiliary function, $\mu(x)$, is again defined to be zero at the end points.

$$\beta_\varepsilon(x) = \beta(x) + \varepsilon\mu(x) \tag{4.19}$$

$$N(\varepsilon) = \frac{J\int_{x_{hub}}^{1} T_c(x,\beta_\varepsilon)dx}{\int_{x_{hub}}^{1} P_c(x,\beta_\varepsilon)dx} \tag{4.20}$$

The extremum of equation (4.20) is obtained by first differentiating it with respect to the perturbation parameter, ε. Equation (4.21) shows the result of this operation.

$$\left.\frac{\partial N(\varepsilon)}{\partial \varepsilon}\right|_{\varepsilon=0} = \frac{\left(\int_{x_{hub}}^{1} P_c dx\right) J \frac{\partial}{\partial \varepsilon}\left(\int_{x_{hub}}^{1} T_c dx\right) - J\left(\int_{x_{hub}}^{1} T_c dx\right)\frac{\partial}{\partial \varepsilon}\left(\int_{x_{hub}}^{1} P_c dx\right)}{\left(\int_{x_{hub}}^{1} P_c dx\right)^2} = 0 \tag{4.21}$$

Making use of the chain rule of differentiation and simplifying using equations (3.12) and (3.19), equation (4.22) is obtained.

$$\left.\frac{\partial N(\varepsilon)}{\partial \varepsilon}\right|_{\varepsilon=0} = \frac{JC_P\int_{x_{hub}}^{1}\frac{\partial T_c}{\partial \beta_\varepsilon}\frac{\partial \beta_\varepsilon}{\partial \varepsilon}dx - JC_T\int_{x_{hub}}^{1}\frac{\partial P_c}{\partial \beta_\varepsilon}\frac{\partial \beta_\varepsilon}{\partial \varepsilon}dx}{{C_P}^2} = 0 \tag{4.22}$$

Taking the derivatives of the function, $\beta_\varepsilon(x)$, with respect to the perturbation parameter and then setting this parameter equal to zero results in equation (4.23).

$$\frac{\partial N(0)}{\partial \varepsilon} = \frac{J\int_{x_{hub}}^{1}\left(C_P\frac{\partial T_c}{\partial \beta} - C_T\frac{\partial P_c}{\partial \beta}\right)\mu(x)dx}{C_P^2} = 0 \tag{4.23}$$

Again, since the auxiliary function, $\mu(x)$, is arbitrary, this equation only holds if the term within the parentheses under the integral sign equal zero. Thus the E-L equation for the unconstrained twist optimization problem is found as equation (4.24).

$$C_P\frac{\partial T_c}{\partial \beta} - C_T\frac{\partial P_c}{\partial \beta} = 0 \tag{4.24}$$

The twist distribution, $\beta(x)$, that satisfies this equation will give the maximum propulsive efficiency at the specified operating condition. In order to solve equation (4.24) the derivatives

of the thrust and power coefficient integrands with respect to the twist function, β, need to be determined. These derivatives will be considered in the sub-section following the next.

4.3.2 Constrained Optimization

The goal of constrained propeller twist optimization is to maximize the efficiency at some specified operating condition where either a prescribed power or a prescribed thrust is required from the propeller. There are a variety of ways to define the problem in order to reach this goal. The following six approaches all lead to the same objective of maximizing the efficiency:

1. Maximize the thrust coefficient at a constant power coefficient.
2. Minimize the power coefficient at a constant thrust coefficient.
3. Minimize the power loss coefficient at a constant thrust coefficient.
4. Minimize the power loss coefficient at a constant power coefficient.
5. Maximize the efficiency at a constant thrust coefficient.
6. Maximize the efficiency at a constant power coefficient.

The first four of these problems will be considered here. Problem 1 states that the twist distribution, $\beta(x)$, is to be determined such that the thrust coefficient, equation (3.12), is maximized, subject to the constraint that the power coefficient, equation (3.19), remains constant. Following the procedure given in section 4.2 for solving a constrained variational problem, a function, X_1, in terms of the Lagrange multiplier, λ_1, is introduced as shown in equation (4.25).

$$X_1 = T_c - \lambda_1 P_c \tag{4.25}$$

This gives the new functional, I_1, defined by equation (4.26).

$$I_1 = \int_{x_{\text{hub}}}^{1} X_1(x, \beta) dx \tag{4.26}$$

Thus the problem has been altered into determining the twist function, $\beta(x)$, that maximizes the functional, I_1. The E-L equation for this problem is thus found as given by equation (4.27).

$$\frac{\partial X_1}{\partial \beta} = 0 = \frac{\partial T_c}{\partial \beta} - \lambda_1 \frac{\partial P_c}{\partial \beta} \tag{4.27}$$

Problem 2 states that the twist distribution that minimizes the power coefficient is to be found subject to a constraint of a constant thrust coefficient. Following the same procedure as above gives the E-L equation for Problem 2 as shown by equation (4.28).

$$\frac{\partial P_c}{\partial \beta} = \lambda_2 \frac{\partial T_c}{\partial \beta} \tag{4.28}$$

Similarly for Problems 3 and 4, the E-L equations are obtained as equations (4.29) and (4.30)

$$\frac{\partial P_{Lc}}{\partial \beta} = \lambda_3 \frac{\partial T_c}{\partial \beta} \tag{4.29}$$

$$\frac{\partial P_{Lc}}{\partial \beta} = \lambda_4 \frac{\partial P_c}{\partial \beta} \tag{4.30}$$

Before proceeding with finding the derivatives of the thrust, power, and power loss coefficient integrands, the relationships between the Lagrange multiplier, λ_1, λ_2, λ_3, and λ_4, will be examined. The relationships between the power, thrust, and power loss coefficient integrands are arrived at by recalling that the total power is the sum of the thrust power and the power loss. So the total power coefficient is then the thrust coefficient multiplied by the advance ratio plus the power loss coefficient. Since the integrals for arriving at these performance coefficients have the same limits, the relationship between the integrands is as given by equation (4.31).

$$P_c = JT_c + P_{Lc} \tag{4.31}$$

Taking the derivative of this equation with respect to β the relationship between the three derivatives is obtained as shown in equation (4.32).

$$\frac{\partial P_c}{\partial \beta} = J \frac{\partial T_c}{\partial \beta} + \frac{\partial P_{Lc}}{\partial \beta} \tag{4.32}$$

Using equations (4.27) to (4.30) along with equation (4.32) allows for arriving at the relationships among the Lagrange multipliers shown by equation (4.33).

$$\lambda_1 = \frac{1}{\lambda_2} = \frac{1}{J + \lambda_3} = \frac{1 - \lambda_4}{J} \tag{4.33}$$

4.3.3 Derivatives of the Performance Coefficient Integrands

The equations for the thrust, power, and power loss coefficient integrands were given in Chapter 3 as equations (3.13), (3.20), and (3.28), respectively. The small induced angle approximation was discussed in the preceding chapter; the result of this assumption when applied to equations (3.13), (3.20), and (3.28) is given by equations (4.34), (4.35), and (4.36).

$$T_c = \tau\left(C_L \cos\varphi - C_D \sin\varphi\right) \tag{4.34}$$

$$P_c = \xi\left(C_L \sin\varphi + C_D \cos\varphi\right) \tag{4.35}$$

$$P_{Lc} = \chi\left(\alpha_i C_L + C_D\right) \tag{4.36}$$

The derivatives of the integrands with the small induced angle approximation will be carried out first as the procedure for the full equations is exactly similar. Results from taking the derivative of the thrust, power, and power loss coefficient integrands where the small angle approximation was not made will be given at the end of this subsection. The differentiation procedure presented here follows the derivation given in reference [44].

The derivative of the thrust coefficient integrand, T_c, will be considered first. By making use of the product rule of differentiation equation (4.37) is obtained.

$$\frac{\partial T_c}{\partial \beta} = \tau\left(C_L \frac{\partial \cos\varphi}{\partial \beta} + \frac{\partial C_L}{\partial \beta}\cos\varphi - C_D \frac{\partial \sin\varphi}{\partial \beta} - \frac{\partial C_D}{\partial \beta}\sin\varphi \right) \tag{4.37}$$

This equation is simplified into equation (4.38) by making use of the chain rule and, for now, treating the drag coefficient, C_D, as a function of only the lift coefficient, C_L.

$$\frac{\partial T_c}{\partial \beta} = \tau\left(-C_L \frac{\partial \varphi}{\partial \beta}\sin\varphi + \frac{\partial C_L}{\partial \beta}\cos\varphi - C_D \frac{\partial \varphi}{\partial \beta}\cos\varphi - \frac{dC_D}{dC_L}\frac{\partial C_L}{\partial \beta}\sin\varphi \right) \tag{4.38}$$

In the following subsection where the derivative of the drag coefficient with respect to the lift coefficient is treated, the drag coefficient will again be set as a function of the angle of attack as was presented in Chapter 3. Equations (3.35) and (3.37) for the wake helix angle, φ, and the lift coefficient, respectively, are now recalled. They are repeated here for convenience.

$$\varphi = \varphi_0 + \alpha_i \tag{3.35}$$

$$C_L = \frac{8xG_0 \sin\varphi_0}{\sigma}\alpha_i = \frac{\alpha_i}{b} \tag{3.37}$$

The derivatives of these two equations with respect to the twist function are given by equations (4.39) and (4.40).

$$\frac{\partial \varphi}{\partial \beta} = \frac{\partial \alpha_i}{\partial \beta} \tag{4.39}$$

$$\frac{\partial C_L}{\partial \beta} = \frac{\partial C_L}{\partial \alpha_i}\frac{\partial \alpha_i}{\partial \beta} = \frac{1}{b}\frac{\partial \alpha_i}{\partial \beta} \tag{4.40}$$

Equations (4.39) and (4.40) are now combined and substituted into equation (4.38). After some simplification the final result for the derivative of the thrust coefficient integrand is obtained and shown as equation (4.41).

$$\frac{\partial T_c}{\partial \beta} = \tau \frac{\partial C_L}{\partial \beta}\left[(1 - bC_D)\cos\varphi - \left(bC_L + \frac{\partial C_D}{\partial C_L} \right)\sin\varphi \right] \tag{4.41}$$

Following this exact same procedure for the derivatives of the power and power loss coefficient integrands, equations (4.42) and (4.43) are obtained, respectively.

$$\frac{\partial P_c}{\partial \beta} = \xi \frac{\partial C_L}{\partial \beta}\left[\left(1 - bC_D\right)\sin\varphi + \left(bC_L + \frac{\partial C_D}{\partial C_L}\right)\cos\varphi\right] \tag{4.42}$$

$$\frac{\partial P_{Lc}}{\partial \beta} = \chi \frac{\partial C_L}{\partial \beta}\left(2bC_L + \frac{dC_D}{dC_L}\right) \tag{4.43}$$

These results, equations (4.41) to (4.43), can now be substituted into equations (4.24) and (4.27) to (4.30) to give the Euler-Lagrange equations for the unconstrained and four constrained problems. The results from the operation are given in equations (4.44) to (4.48).

Unconstrained Problem:

$$C_P\tau\left[\left(1 - bC_D\right)\cos\varphi - \left(bC_L + \frac{\partial C_D}{\partial C_L}\right)\sin\varphi\right] = C_T\xi\left[\left(1 - bC_D\right)\sin\varphi + \left(bC_L + \frac{\partial C_D}{\partial C_L}\right)\cos\varphi\right] \tag{4.44}$$

Problem 1:

$$\tau\left[\left(1 - bC_D\right)\cos\varphi - \left(bC_L + \frac{\partial C_D}{\partial C_L}\right)\sin\varphi\right] = \lambda_1\xi\left[\left(1 - bC_D\right)\sin\varphi + \left(bC_L + \frac{\partial C_D}{\partial C_L}\right)\cos\varphi\right] \tag{4.45}$$

Problem 2:

$$\xi\left[\left(1 - bC_D\right)\sin\varphi + \left(bC_L + \frac{\partial C_D}{\partial C_L}\right)\cos\varphi\right] = \lambda_2\tau\left[\left(1 - bC_D\right)\cos\varphi - \left(bC_L + \frac{\partial C_D}{\partial C_L}\right)\sin\varphi\right] \tag{4.46}$$

Problem 3:

$$\chi\left(2bC_L + \frac{dC_D}{dC_L}\right) = \lambda_3\tau\left[\left(1 - bC_D\right)\cos\varphi - \left(bC_L + \frac{\partial C_D}{\partial C_L}\right)\sin\varphi\right] \tag{4.47}$$

Problem 4:

$$\chi\left(2bC_L + \frac{dC_D}{dC_L}\right) = \lambda_4\xi\left[\left(1 - bC_D\right)\sin\varphi + \left(bC_L + \frac{\partial C_D}{\partial C_L}\right)\cos\varphi\right] \tag{4.48}$$

As was mentioned, the procedure for determining the derivatives of the integrands without the small induced angle approximation is exactly as given above except for two key differences. The first is the presence of the $\cos^2\alpha_i$ term which adds an extra step where the product rule of differentiation is to be used. The second difference, and the more important of

the two, is in the treatment of the derivative of the lift coefficient with respect to the induced angle that appeared in equation (4.40). Recall the full equation for the lift coefficient that was obtained from vortex theory, equation (3.33).

$$C_L = \frac{8x}{\sigma} G \tan\alpha_i \sin\varphi. \tag{3.33}$$

The derivative of this equation with respect to the induced angle is shown in equation (4.49).

$$\frac{\partial C_L}{\partial \alpha_i} = C_L\left[\cot\varphi + \frac{2}{\sin(2\alpha_i)} + \frac{\cos\varphi}{G}\frac{\partial G}{\partial \sin\varphi}\right] = \frac{1}{b_l} \tag{4.49}$$

In equation (4.40) the derivative of the lift coefficient with respect to the induced angle was replaced by b^{-1}. In order to maintain similarity between the small angle and full solution problems, the factor, b_l, is introduced in equation (4.49) as the "large angle" equivalent of b. Note, however, that the lift coefficient is not equal to the induced angle divided by the factor b_l, whereas in the small angle approximation case the lift coefficient is equal to the induced angle divided by the factor b. With these two key differences handled, the same procedure can be followed as for the small angle derivatives. The results from taking the derivatives and substituting them into equations (4.24) and (4.27) to (4.30) are shown in equations (4.50) to (4.54).

Unconstrained Problem:

$$\begin{aligned} C_P\tau\left[(1-b_l C_D)\cos\varphi - \left(b_l C_L + \frac{\partial C_D}{\partial C_L}\right)\sin\varphi - 2b_l \tan\alpha_i (C_L\cos\varphi - C_D\sin\varphi)\right] = \\ C_T\xi\left[(1-b_l C_D)\sin\varphi + \left(b_l C_L + \frac{\partial C_D}{\partial C_L}\right)\cos\varphi - 2b_l \tan\alpha_i (C_L\sin\varphi + C_D\cos\varphi)\right] \end{aligned} \tag{4.50}$$

Problem 1:

$$\tau\left[\left(1-b_l C_D\right)\cos\varphi-\left(b_l C_L+\frac{\partial C_D}{\partial C_L}\right)\sin\varphi-2b_l\tan\alpha_i\left(C_L\cos\varphi-C_D\sin\varphi\right)\right]=$$
$$\lambda_1\xi\left[\left(1-b_l C_D\right)\sin\varphi+\left(b_l C_L+\frac{\partial C_D}{\partial C_L}\right)\cos\varphi-2b_l\tan\alpha_i\left(C_L\sin\varphi+C_D\cos\varphi\right)\right] \tag{4.51}$$

Problem 2:

$$\xi\left[\left(1-b_l C_D\right)\sin\varphi+\left(b_l C_L+\frac{\partial C_D}{\partial C_L}\right)\cos\varphi-2b_l\tan\alpha_i\left(C_L\sin\varphi+C_D\cos\varphi\right)\right]=$$
$$\lambda_2\tau\left[\left(1-b_l C_D\right)\cos\varphi-\left(b_l C_L+\frac{\partial C_D}{\partial C_L}\right)\sin\varphi-2b_l\tan\alpha_i\left(C_L\cos\varphi-C_D\sin\varphi\right)\right] \tag{4.52}$$

Problem 3:

$$\chi\left[\left(1-b_l C_D\right)\sin\alpha_i+\left(b_l C_L+\frac{\partial C_D}{\partial C_L}\right)\cos\alpha_i-2b_l\tan\alpha_i\left(C_L\sin\alpha_i+C_D\cos\alpha_i\right)\right]=$$
$$\lambda_3\tau\left[\left(1-b_l C_D\right)\cos\varphi-\left(b_l C_L+\frac{\partial C_D}{\partial C_L}\right)\sin\varphi-2b_l\tan\alpha_i\left(C_L\cos\varphi-C_D\sin\varphi\right)\right] \tag{4.53}$$

Problem 4:

$$\chi\left[\left(1-b_l C_D\right)\sin\alpha_i+\left(b_l C_L+\frac{\partial C_D}{\partial C_L}\right)\cos\alpha_i-2b_l\tan\alpha_i\left(C_L\sin\alpha_i+C_D\cos\alpha_i\right)\right]=$$
$$\lambda_4\xi\left[\left(1-b_l C_D\right)\sin\varphi+\left(b_l C_L+\frac{\partial C_D}{\partial C_L}\right)\cos\varphi-2b_l\tan\alpha_i\left(C_L\sin\varphi+C_D\cos\varphi\right)\right] \tag{4.54}$$

4.3.4 Derivative of the Drag Coefficient

In taking the derivatives of the performance coefficient integrands the derivative of the drag coefficient with respect to the lift coefficient appeared. In order to evaluate this derivative, the drag model needs to be revisited. The incompressible drag coefficient, C_{Di}, was modeled as given by equation (4.55).

$$C_{Di}=\begin{cases}0.1\left[C_{L,\min C_D}-\left(A_1\alpha+A_2\right)\right]^4+C_{D,\min} & \alpha\le\alpha_{\text{switch}}\\ A_3\left(\alpha-\dfrac{\pi}{2}\right)^2+C_{D,\max} & \alpha>\alpha_{\text{switch}}\end{cases} \tag{4.55}$$

At low angles of attack, below the switch over angle, α_{switch}, the drag coefficient was modeled by a quartic equation with a minimum drag coefficient, $C_{D,\min}$, located close to zero degrees angle of

attack. At angles of attack greater than the switch over angle the model was a quadratic equation with a maximum located at 90 degrees angle of attack with a value equal to the maximum drag coefficient, $C_{D,\max}$. The Mach number dependence of the drag coefficient was modeled as given by equation (4.56), where the drag divergence Mach number, M_{DD}, was determined from the Korn equation, equation (3.40). This equation, which has a dependence on the lift coefficient is repeated here for reference.

$$C_D = \begin{cases} C_{Di} & M \le M_{DD} \\ C_{Di} + \nu\left(\dfrac{M - M_{DD}}{1 - M_{DD}}\right)^3 & M > M_{DD} \end{cases} \tag{4.56}$$

$$M_{DD} + \frac{C_L}{10} + \frac{t}{c} = \kappa \tag{3.40}$$

The derivative of the drag coefficient within the various ranges is thus given by equation (4.57).

$$\frac{dC_D}{dC_L} = \begin{cases} \left.\begin{cases} 0.4A_1\left[\left(A_1\alpha + A_2\right) - C_{L,\min C_D}\right]^3 \dfrac{\partial\alpha}{\partial C_L} & \alpha \le \alpha_{\text{switch}} \\ A_3\left(2\alpha - \pi\right) & \alpha > \alpha_{\text{switch}} \end{cases}\right\} & M \le M_{DD} \\ \dfrac{dC_{Di}}{dC_L} + 3\nu\dfrac{\left(M - M_{DD}\right)^2\left(1 - M\right)}{\left(1 - M_{DD}\right)^4} & M > M_{DD} \end{cases} \tag{4.57}$$

4.4 Implementation of Optimization

The discussion of this section includes some of the practical aspects related to the application of the optimization derived in the preceding section. Here the lift model is treated as purely linear to simplify the explanation of the solution process. Compressibility corrections are also neglected for now. Adding the full stall model and compressibility parameters does not change the solution process. In order to assess the correctness of the method of solution, results published by Lock, Pankhurst, and Fowler [44] were reproduced.

4.4.1 Method of Implementation

Unconstrained Problem

Studying equation (4.44) it is observed that though this equation gives the twist distribution, $\beta(x)$, it is not explicitly present. This is because the solution requires the coupling of this equation with equations (3.34) to (3.37). The approach taken here is to solve equation (4.44) for the wake helix angle, φ, first, and then determine the twist distribution. Rewriting equation (4.44) as shown in equation (4.58) the problem is set up for iteration.

$$\cos\varphi = \frac{1}{(1-bC_D)}\left\{\frac{C_T\xi}{C_P\tau}\left[(1-bC_D)\sin\varphi + \left(bC_L + \frac{\partial C_D}{\partial C_L}\right)\cos\varphi\right] + \left(bC_L + \frac{\partial C_D}{\partial C_L}\right)\sin\varphi\right\} \qquad (4.58)$$

The solution procedure, which is illustrated in Figure 4.1, starts by initializing the twist distribution as a linear function with a negative slope. This twist distribution is used to determine initial values for the thrust and power coefficient using the aerodynamic model described in Chapter 3. For each blade element the helix angle, φ_0, is known, and the induced angle, α_i, is initialized to the values obtained in the process of determining the initial thrust and power coefficient values. With this information the initial wake helix angle and lift coefficient is determined using equations (3.35) and (3.37); the factor b is also calculated in this step. Knowledge of the lift coefficient allows for determining the angle of attack from equation (3.34), which is used in turn to determine both the drag coefficient and its derivative with respect to the lift coefficient. All the quantities on the right hand side of equation (4.58) are now determined so a new wake helix angle can be calculated. This new wake helix angle gives a new induced angle. The procedure is repeated to update the values that go into the right hand side of equation (4.58). This procedure is continued until the wake helix angle converges; the method of successive over relaxation is used in the iterating process. With the wake helix angle and the angle of attack found, the blade angle, β, for the element under consideration is thus known from

equation (3.36). Once the blade angle is calculated for each blade element, a new thrust and power coefficient is calculated. So the process repeats itself until the differences between the current and previous values of the thrust coefficient are less than a prescribed tolerance. The final blade angle distribution that is obtained is the twist that maximizes the efficiency at the specified operating condition.

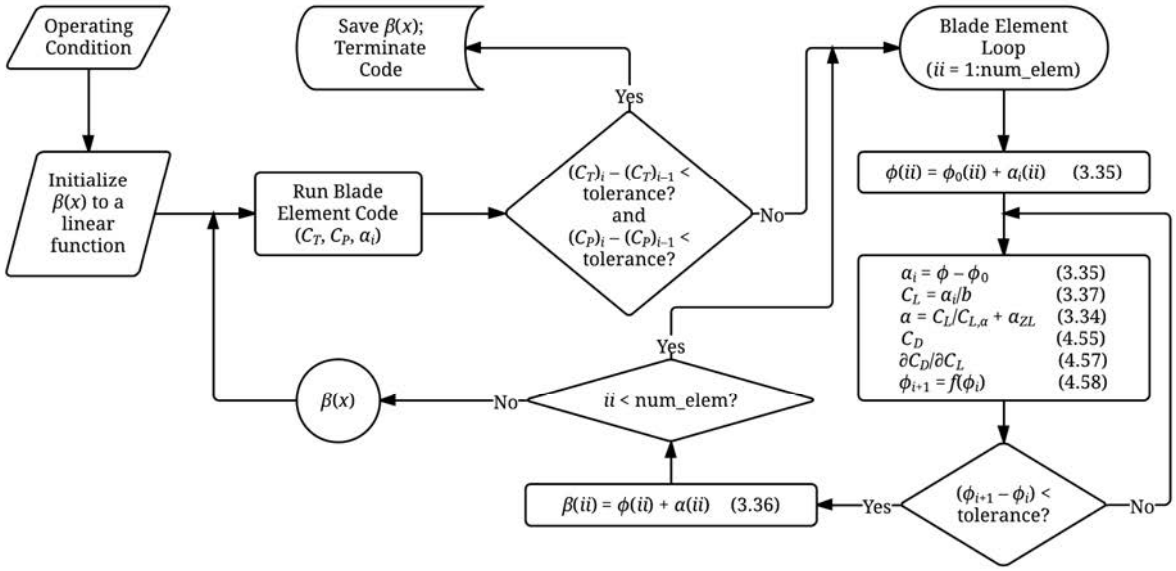

Figure 4.1. Flowchart of the solution procedure for the unconstrained problem.

Constrained Problem

In the constrained problems additional variables are present – these are the Lagrange multipliers whose values need to be determined from the constraint, generically defined as C_0. The same procedure for determining the Lagrange multiplier values is followed for all four problems. Depending on which of the four problems is being solved, one of the E-L equations in the form given by equations (4.59) to (4.62) is solved.

$$\varphi = \arccos\left\{ \frac{\dfrac{\lambda_1 \xi}{\tau}\left[\left(1 - bC_D\right)\sin\varphi + \left(bC_L + \dfrac{\partial C_D}{\partial C_L} \right)\cos\varphi \right] + \left(bC_L + \dfrac{\partial C_D}{\partial C_L} \right)\sin\varphi}{\left(1 - bC_D\right)} \right\} \tag{4.59}$$

$$\varphi = \arccos\left\{ \frac{\dfrac{\lambda_2 \tau}{\xi}\left[\left(1 - bC_D\right)\cos\varphi - \left(bC_L + \dfrac{\partial C_D}{\partial C_L} \right)\sin\varphi \right] - \left(bC_L + \dfrac{\partial C_D}{\partial C_L} \right)\cos\varphi}{\left(1 - bC_D\right)} \right\} \tag{4.60}$$

$$bC_L = \alpha_i = \varphi - \varphi_0 = \frac{\lambda_3 \tau}{2\chi}\left[\left(1 - bC_D\right)\cos\varphi - \left(bC_L + \frac{\partial C_D}{\partial C_L} \right)\sin\varphi \right] - \frac{1}{2}\frac{\partial C_D}{\partial C_L} \tag{4.61}$$

$$\varphi = \frac{\lambda_4 \xi}{2\chi}\left[\left(1 - bC_D\right)\sin\varphi + \left(bC_L + \frac{\partial C_D}{\partial C_L} \right)\cos\varphi \right] - \frac{1}{2}\frac{\partial C_D}{\partial C_L} + \varphi_0 \tag{4.62}$$

The constrained solution procedure starts off by initially setting the Lagrange multiplier equal to zero. Again the method of successive over relaxation is used to iterate for the wake helix angle, φ, and the same method of iterating for this angle is used here as was described for the unconstrained problem. Once the wake helix angle is known, the blade angle is found and the elemental thrust and power coefficients are calculated. The contribution by each element to the total thrust and power coefficients is added up to give the thrust and power coefficients. Since the desired result is the Lagrange multiplier value that causes the difference between either the power or thrust coefficient and the constraint to be equal to zero, depending on the problem being solved, the problem is one of finding the root of this difference function (($C_T - C_0$) or ($C_P - C_0$)). The method used for finding this root is bisection. Once a power or thrust coefficient value based on a Lagrange multiplier value is determined, the Lagrange multiplier is incremented and the procedure is repeated. This is continued until a sign change in the difference function occurs, at which point the bisection procedure is started. The results obtained from this

procedure are the Lagrange multiplier value that satisfies the constraint and the blade angle distribution, $\beta(x)$. The described solution procedure is shown in the flowchart in Figure 4.2.

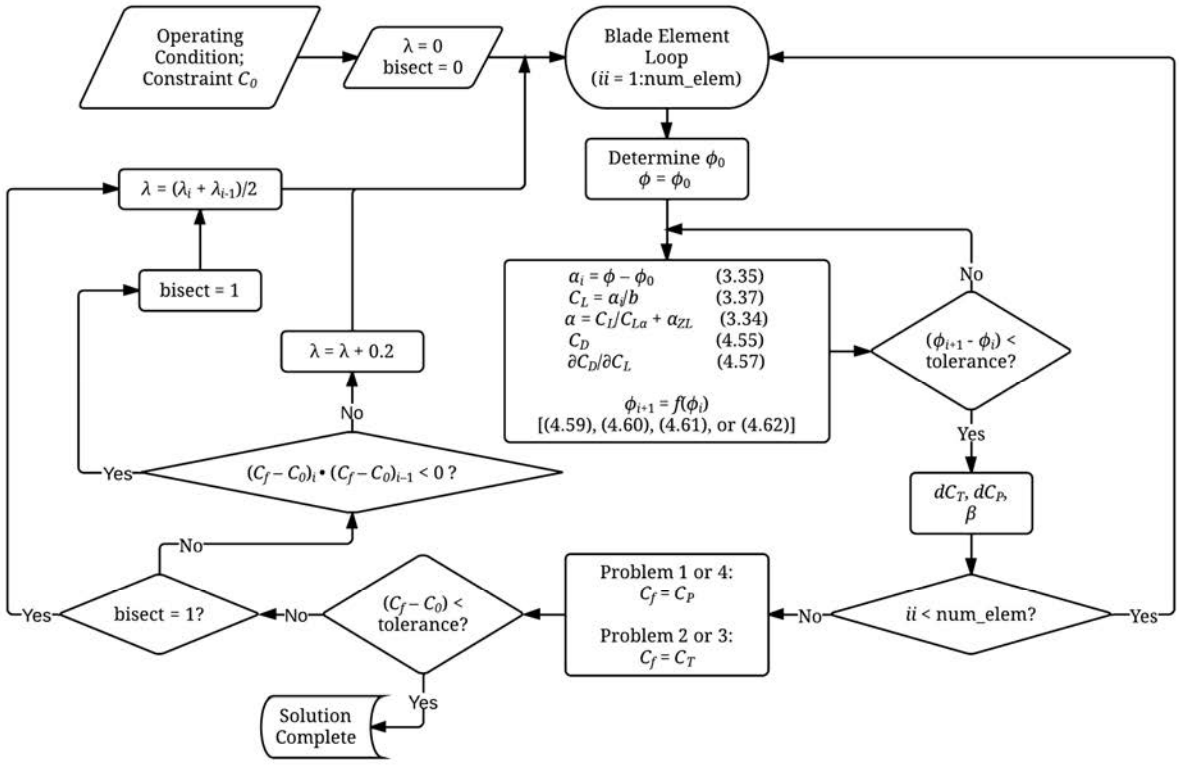

Figure 4.2. Flowchart of the constrained problem solution procedure.

4.4.2 Validation of Method

In order to validate the procedure used here to iterate for the wake helix angle, results from a similar optimization procedure published by Lock, Pankhurst, and Fowler [44] was reproduced. The propeller blade airfoil model used in reference [44] was a Clark Y airfoil. Sufficient information regarding the airfoil performance can be found in references [44] and [128-130] so that the results were reproducible. The only difficulty, and likely source of error, was that many of the airfoil performance parameters were given in graphic form and had to be converted to tables for use in the computer program. The compressibility corrections were also

different than those presented in Chapter 3, but again these corrections were clearly presented in the Lock, Pankhurst, and Fowler paper.

In reference [44] the authors solved for the optimum twist of a propeller blade using Problem 3, but the definition for the power and power loss coefficients were different than those used here. The power coefficient of Lock et al. needs to be multiplied by 2π in order to obtain the power coefficient as defined here. Accordingly, the Lagrange multiplier of Lock et al., λ_L, needs to be multiplied by 2π to arrive at the equivalent Problem 3 Lagrange multiplier, λ_3, as shown in equation (4.63).

$$\lambda_3 = 2\pi\lambda_L \tag{4.63}$$

With the relationships given by equation (4.33) the equivalent Lagrange multipliers for each of the four problems can be determined and then the results compared to the results published by Lock.

The comparisons presented in Table 4.1 used the Lagrange multiplier published by Lock et al. to solve for the optimum twist. This twist distribution was then used to determine the torque coefficient and efficiency. These two values are compared with the results from Lock et al. in the tables below. Perhaps not too surprising, all four problems produced the exact same torque coefficient and efficiency when the equivalent Lagrange multipliers were used. Thus only the results from Problem 3 are shown in the tables below.

Agreement between the results from the present method and that of Lock was very good, with the percent differences in the efficiencies being for the most part less than 2%. This difference can be attributed to the tabulation of graphical airfoil data, and perhaps also to a difference in rounding while doing calculations by hand. Reference [44] was published in 1942

so the calculations were likely carried out by hand. The disparities, however, are very small and it can safely be said that the method used for determining the wake helix angle is satisfactory.

TABLE 4.1

COMPARISON OF PROBLEM 3 RESULTS WITH REFERENCE [44] (CONTINUED)

v_∞ = 352 mph, J = 1.95, Altitude = 21,000 ft.				
Lagrange Multiplier, λ_L	**Method**	**C_Q**	**η**	**% Difference (η)**
0.010	Ref. [44]	0.0085	0.8390	1.63
	Problem 3	0.0090	0.8253	
0.020	Ref. [44]	0.0149	0.8890	0.90
	Problem 3	0.0150	0.8810	
0.039	Ref. [44]	0.0252	0.9000	0.14
	Problem 3	0.0254	0.8987	
0.058	Ref. [44]	0.0330	0.8980	0.55
	Problem 3	0.0334	0.8930	
0.085	Ref. [44]	0.0407	0.8790	0.20
	Problem 3	0.0405	0.8808	
v_∞ = 428 mph, J = 2.62, Altitude = 21,000 ft.				
Lagrange Multiplier, λ_L	**Method**	**C_Q**	**η**	**% Difference (η)**
0.049	Ref. [44]	0.0353	0.8940	0.29
	Problem 3	0.0356	0.8914	
0.070	Ref. [44]	0.0456	0.8900	0.06
	Problem 3	0.0448	0.8905	
0.092	Ref. [44]	0.0526	0.8830	0.22
	Problem 3	0.0518	0.8849	
0.113	Ref. [44]	0.0574	0.8760	0.20
	Problem 3	0.0572	0.8778	
0.133	Ref. [44]	0.0616	0.8690	0.28
	Problem 3	0.0612	0.8714	
0.160	Ref. [44]	0.0666	0.8590	0.30
	Problem 3	0.0665	0.8616	

TABLE 4.1

COMPARISON OF PROBLEM 3 RESULTS WITH REFERENCE [44] (CONCLUDED)

v_∞ = 528 mph, J = 4.05, Altitude = 21,000 ft.				
Lagrange Multiplier, λ_L	**Method**	**C_Q**	**η**	**% Difference (η)**
0.049	Ref. [44]	0.0436	0.8150	3.16
	Problem 3	0.0429	0.7893	
0.097	Ref. [44]	0.0605	0.8390	1.55
	Problem 3	0.0600	0.8260	
0.187	Ref. [44]	0.0867	0.8370	0.80
	Problem 3	0.0862	0.8303	
0.268	Ref. [44]	0.1062	0.8200	0.74
	Problem 3	0.1054	0.8139	
0.340	Ref. [44]	0.1222	0.8010	0.45
	Problem 3	0.1217	0.7974	
0.403	Ref. [44]	0.1359	0.7850	0.35
	Problem 3	0.1354	0.7822	

4.5 Twist Optimization Results

Three operating conditions were defined for studying the optimum twist of a propeller. Once the optimum twist for a particular operating condition was obtained the performance of the propeller at the other two design points were analyzed to compare the three twist distributions. The advance ratio, propeller angular speed, altitude, and thrust coefficient associated with the three design conditions of takeoff, climb, and cruise are given in Table 4.2. The airspeed associated with the takeoff condition is the airspeed at takeoff rotation. The values in Table 4.2 were determined from reference [131] in which the operating environment of the propellers on Beech 1900D airliners were defined. These aircraft were fitted with four bladed, 110 inch diameter constant speed propellers. Thus the geometry of the propellers optimized here has these two parameters in common with the Beech 1900D propellers. Other parameters such as the chord lengths and thicknesses were estimated – a constant chord length of 9 inches was used for the entire blade span, and the blade was given a thickness that varied from 40% at the root to 5% at

the tip. The propeller geometry used here is shown in Figure 4.3 where the normalized thickness and chord distribution along the blade span is plotted.

TABLE 4.2

DEFINITION OF THE PROPELLER OPERATING CONDITIONS

Operating Condition	J	RPM	Altitude (ft)	$C_{T,0}$
Takeoff	0.7173	1725	0	0.1792
Climb	1.2603	1580	7500	0.1637
Cruise	2.0663	1480	15000	0.1595

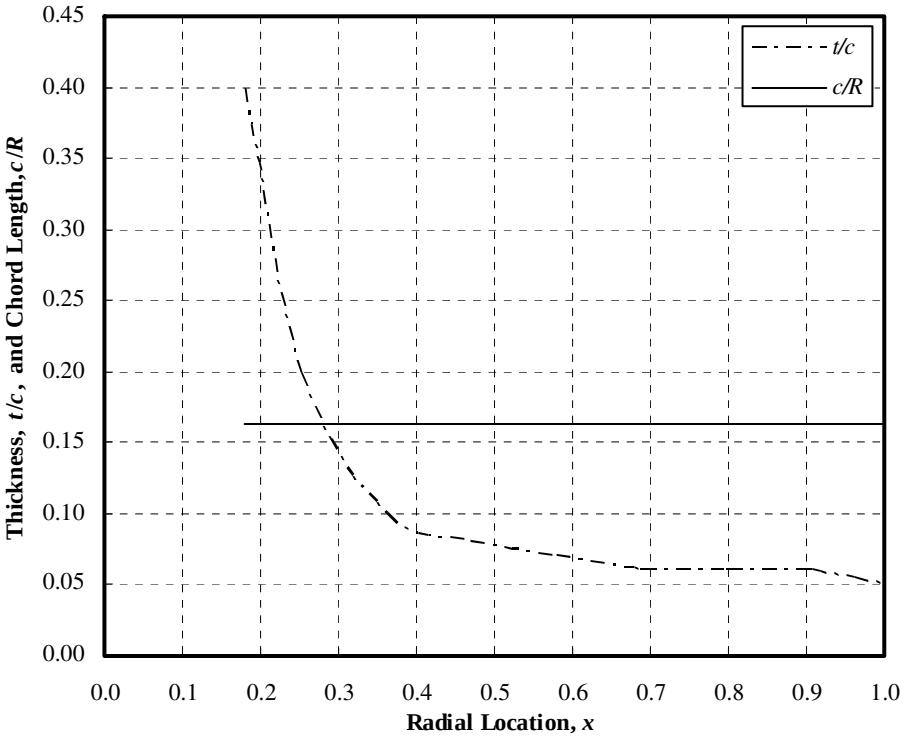

Figure 4.3. Chord and thickness distributions along the span.

Unconstrained optimization at the advance ratios, angular speeds, and altitudes specified in Table 4.2 will be discussed first. This will be followed by the constrained optimization results where the physical meaning of the Lagrange multiplier will also be explained. The final subsection will then be focused on a special aircraft mission where a variable twist propeller could provide a performance benefit.

4.5.1 Unconstrained Optimization Results

The unconstrained problem produces a twist distribution that maximizes the efficiency of the propeller without regard to the thrust and power coefficients at which this maximum efficiency occurs. So the thrust coefficient coincident with the maximum efficiency was not expected to match that given in Table 4.2. In fact, Table 4.3 shows that the thrust coefficients obtained from the unconstrained optimization were significantly lower at all three advance ratios. This suggests that whenever a propeller of fixed solidity is required to either produce more thrust or absorb more power at a specific operating condition, the efficiency deteriorates.

TABLE 4.3

UNCONSTRAINED OPTIMIZATION RESULTS

	Takeoff	**Climb**	**Cruise**
C_T	0.0727	0.0867	0.1093
C_P	0.0648	0.1258	0.2550
η	0.8047	0.8689	0.8856

In Figure 4.4 the twist distributions that resulted from the unconstrained optimization is shown. In generating this plot the blade angles at the tips were all set equal to zero in order to compare the twist in the respective blades apart from the blade pitch angles, $\beta_{.75}$. All three operating conditions resulted in blades that had between 40 to 45 degrees of twist in them, but the distribution of the twist varied significantly. This difference can be explained by considering the span-wise variation of the helix angle. Generally speaking, the helix angle will be large at the blade root due to the small rotational velocity component and comparatively large forward velocity. Thus, for all three cases, large blade angles are seen at the blade root. Moving further outboard on the blade, the rotational velocity component becomes larger and the helix angle decreases. The rate at which the helix angle decreases depends on the advance ratio (i.e. the magnitude of the forward speed relative to the rotational component). At low advance ratios the

helix angle decreases rapidly near the root, but out towards the tip the rate of decline is much reduced. As the advance ratio increases, the variation of the helix angle approaches linear behavior. Figure 4.4 clearly shows that the optimum blade twists followed the span-wise variation of the helix angle. The low advance ratio case showed about a 24 degree decrease in blade angle inboard of the 40% tip radius location and only about 18 degrees over the outboard portion. Examining the high advance ratio case, on the other hand, it is seen that the change in blade twist over the blade portion inboard of the 0.4*R* location was only about 17 degrees whereas the change over the outboard portion was about 24 degrees. The blade twist at the advance ratio at which the aircraft climbed lay in between the cruise and takeoff advance ratio cases.

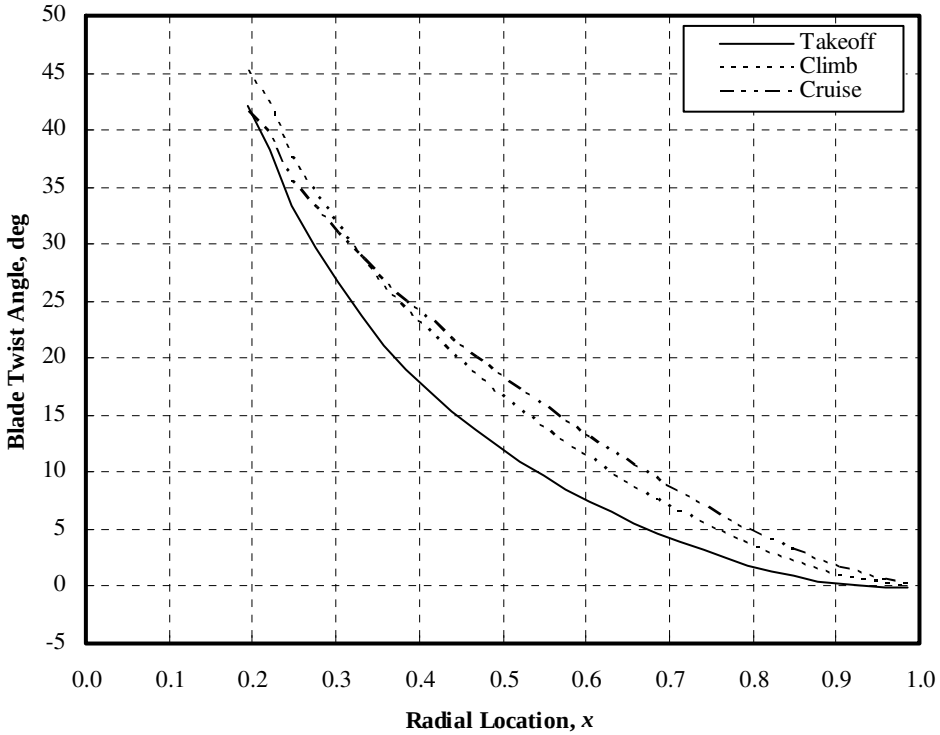

Figure 4.4. Unconstrained twist distributions.

In closing this subsection, the two most important aspects of the results shown here are pointed out. The first is that the optimum blade twist distribution varies considerably with

advance ratio, though the total amount of twist in a blade remains almost the same. The second point is that the thrust coefficients associated with the maximum efficiency state are considerably lower than the thrust coefficients at which the propeller will be required to operate at the specified design conditions. These points will be considered when defining a mission for a variable twist propeller.

4.5.2 Constrained Optimization Results

Since the constraints given in Table 4.2 are for the thrust coefficient, only Problems 2 and 3 were valid for the optimization considered in this section. In studying the results from these two approaches it was found that either method of optimization produced the same results. For this reason, only results from Problem 3 are presented in this subsection.

Physical Interpretation of the Lagrange Multiplier

For the case of Problem 3 it was observed that both the thrust and power coefficients increased with the Lagrange multiplier. This suggested that the Lagrange multiplier had a direct influence on the blade pitch angle. Figure 4.5 is a plot of the resulting blade pitch angles and twists due to different Lagrange multiplier values. As can be seen here, as well as in Figure 4.6, the primary effect of an increasing Lagrange multiplier was an increasing blade pitch angle. The secondary effect was a change in the amount of twist in the propeller blade as well as altering the twist distribution. In considering these results it can be concluded that the Lagrange multiplier controls the blade pitch angle.

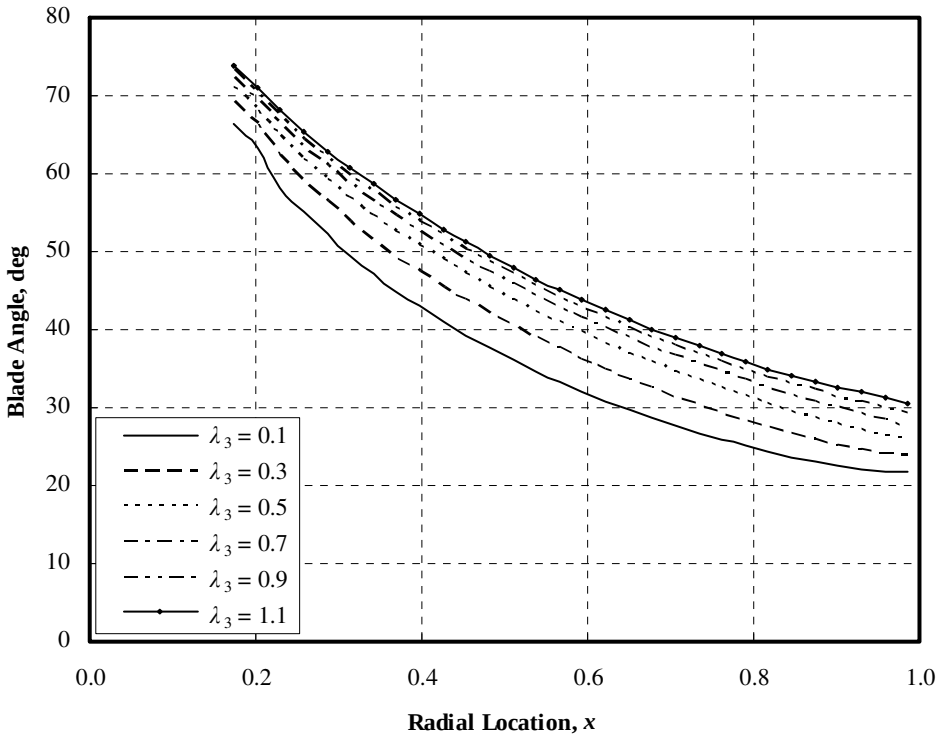

Figure 4.5. Plot showing the effect of λ_3 on $\beta(x)$.

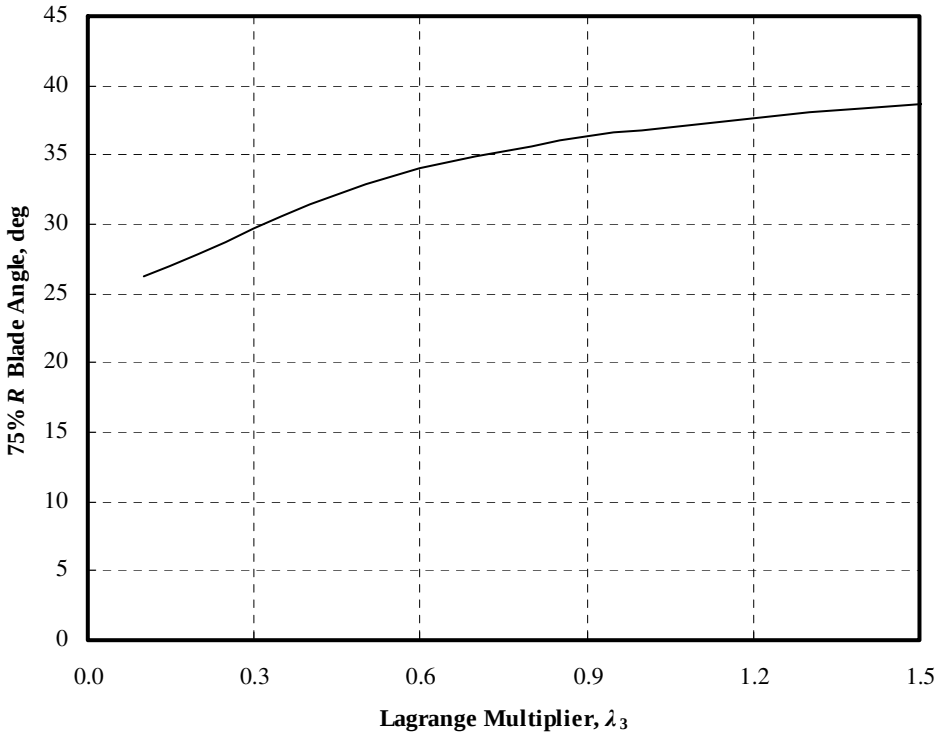

Figure 4.6. Plot of the $\beta_{.75}$ pitch angle as a function of λ_3.

An alternate interpretation of the Lagrange multiplier is also possible if the unconstrained problem is compared with either Problem 1 or 2. Consider equations (4.24) and (4.27), repeated here for convenience.

$$C_P \frac{\partial T_c}{\partial \beta} - C_T \frac{\partial P_c}{\partial \beta} = 0 \tag{4.24}$$

$$\frac{\partial T_c}{\partial \beta} = \lambda_1 \frac{\partial P_c}{\partial \beta} \tag{4.27}$$

Seeing these two equations written side-by-side suggests that the Lagrange multiplier, for the case of Problem 1, could be considered as the ratio of the thrust coefficient to the power coefficient. But this relationship was found to only be true for the case when the optimization was constrained to the power coefficient that resulted from unconstrained optimization. Thus the alternate interpretation of the value of the Lagrange multiplier, λ_1, is that if this parameter equals the ratio of the thrust coefficient to the power coefficient, the absolute maximum propeller efficiency at the specified operating condition is obtained. For any other case the efficiency will be lower. Comparing Problem 2 (equation (4.28)) with the unconstrained problem, it can be observed that the relationship was now just the inverse of Problem 1.

$$\frac{\partial P_c}{\partial \beta} = \lambda_2 \frac{\partial T_c}{\partial \beta} \tag{4.28}$$

Now the condition for absolute maximum efficiency is that the Lagrange multiplier, λ_2, be equal to the ratio of the power to the thrust coefficient. It can also be shown that for Problems 3 and 4 the condition of absolute maximum efficiency is given by equations (4.64) and (4.65).

$$\lambda_3 = \frac{C_{PL}}{C_T} \tag{4.64}$$

$$\lambda_4 = \frac{C_{PL}}{C_P} \tag{4.65}$$

Twist Optimization Results

For each of the design conditions specified in Table 4.2 the resulting blade twist that was obtained from the constrained optimization is plotted in Figure 4.7. Again the total amount of twist in the propeller blade was between 40 to 45 degrees. The span-wise distribution of this twist was still different for each operating condition, but the difference was significantly less than what was seen in the unconstrained problem results. Outboard of the 40% tip radius location the twist in the climb prop was almost identical to that for the cruise prop. It was only in the inboard portion where a difference was observed. The takeoff optimized propeller again showed the greatest amount of twist over the first 25% of the blade, but compared to Figure 4.4 the inboard section did not have an equally large change in the twist angle.

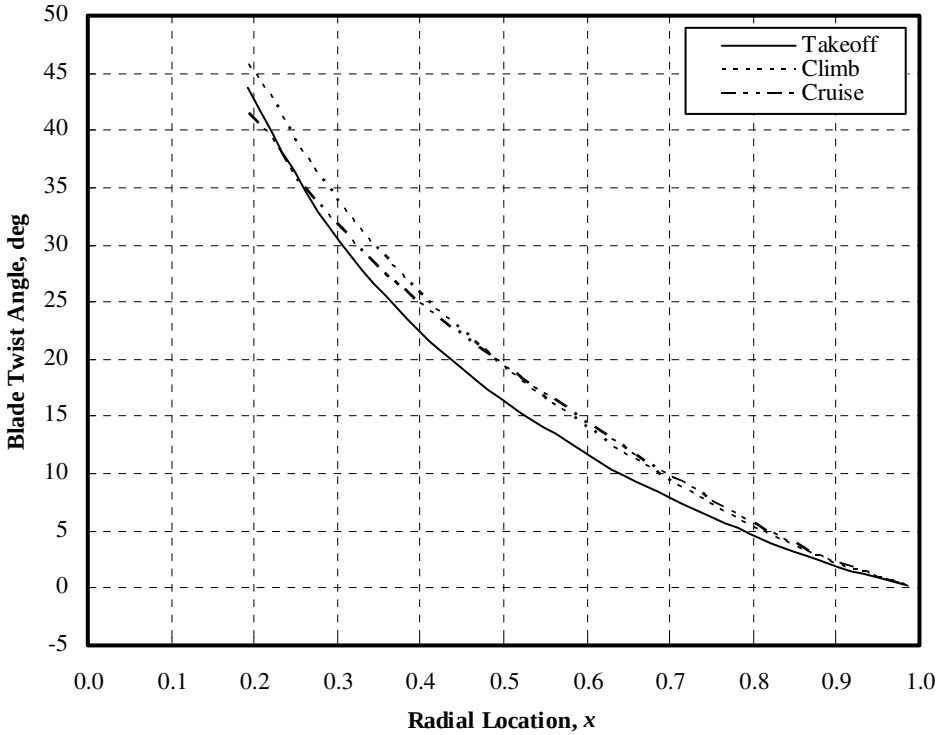

Figure 4.7. Constrained twist distributions.

Though the three twist distributions shown in Figure 4.7 were more alike than the unconstrained results, there still was a significant difference between the three blades. So it was

expected that the performance of each blade at each of the design conditions would be significantly different. Surprisingly this was not the case. The performance results are shown in Table 4.4.

TABLE 4.4

CONSTRAINED OPTIMIZATION PERFORMANCE RESULTS

	C_P	Optimized for:		
		Takeoff	**Climb**	**Cruise**
Operating at:	**Takeoff**	0.1741	0.1749	0.1748
	Climb	0.2454	0.2446	0.2449
	Cruise	0.3771	0.3767	0.3756
	η	**Takeoff**	**Climb**	**Cruise**
Operating at:	**Takeoff**	0.7383	0.7351	0.7354
	Climb	0.8407	0.8435	0.8423
	Cruise	0.8739	0.8749	0.8774

Each column represents the condition for which the propeller was optimized, and the rows are the condition at which the propeller was being operated. Since the thrust coefficient was the constraint, it is not shown in this table. Notice that the power coefficients in each row do not vary much, and similarly, there is not much change in the efficiency in each row. The highest efficiency in each row is coincident with the condition for which it was optimized, but the differences are not significant. This is indeed a very interesting observation. It suggests that when a propeller is required to produce a lot of thrust (or absorb a lot of power) the efficiency simply will not be very high, and the twist does not have a major influence on the performance. So, if an aircraft's mission is a typical one of takeoff, climb, and a long cruise portion, the best compromise would be to twist the propeller for maximum efficiency in cruise as it will not have a considerable effect on takeoff and climb performance.

Considering now the idea of active twist control, the analysis suggests the performance benefit for such a typical aircraft mission as has been considered here would be almost nonexistent, even though the optimum twist at takeoff is considerably different than in cruise. However, looking back at the unconstrained results though, an interesting observation can be made. Comparing the thrust and power coefficients and the efficiencies from the unconstrained optimization results with those given Table 4.4 shows that the unconstrained efficiency at the takeoff advance ratio was considerably higher than that shown for the constrained case and the thrust and power coefficients were also quite a bit lower. As it was already mentioned, the maximum efficiency occurs at lower thrust and power. This suggests that if an aircraft's mission consists of extended loitering segments where the aircraft would be operating at very low power settings mixed with maximum speed dash segments, a variable twist propeller may be viable.

4.5.3 Analysis of a Loiter-Dash Mission

For this analysis, an aircraft similar in size and performance to the Daher-Socata TBM 850 was considered. Some specifications of this aircraft and its propeller are given in Table 4.5 [132].

TABLE 4.5

DAHER-SOCATA TBM 850 SPECIFICATIONS [132]

Dimensions	Length (ft)	34.92
	Height (ft)	14.29
	Wing Area (ft^2)	193.75
	Aspect Ratio	8.216
Power Plant	Pratt & Whitney Canada PT6A – 66D	
	Shaft Horse Power	850
Propeller	No. of Blades	4
	Diameter (in)	91
	Speed (*RPM*)	2000
Performance	Maximum Takeoff Weight (lb)	7394
	Maximum Cruise Speed (kts)	320

The propeller that was evaluated here had the normalized thickness and chord length distributions used in the preceding section (Figure 4.3) and had the same number of blades, but the diameter was set equal to that given in Table 4.5. The analysis started by defining the high speed cruise operating condition. The true airspeed, angular speed, and power constraint for this case are shown in Table 4.6.

TABLE 4.6

DEFINITION OF THE DASH AND LOITER OPERATING CONDITIONS

	v_∞ (kts)	*RPM*	*J*	C_P	C_T	$C_{D,\text{tot}}$	$C_{D,i}$	$C_{D,0}$
Dash	300.00	2000	2.003	0.2118	0.0930	0.0138	0.0008	0.0130
Loiter	112.09	2000	0.748	0.0467	0.0491	0.0520	0.0390	0.0130

These values were used to optimize the propeller twist for the dash phase and obtain the associated thrust for this flight condition. This thrust value was assumed to be the thrust required in order to maintain the desired high cruising speed. The thrust required value was considered to be the total aircraft drag at this condition. With this information, as well as the aircraft weight, assumed to be the maximum takeoff weight, the induced drag and aircraft parasite drag coefficients could be estimated. Equation (4.66) was used to estimate the induced drag, which was then used in equation (4.67) to obtain the aircraft parasite drag. The Oswald efficiency, *e*, was assumed equal to 0.8.

$$C_{D,i} = \frac{C_L^2}{\pi e \text{AR}} \tag{4.66}$$

$$C_{D,\text{tot}} = C_{D,0} + C_{D,i} \tag{4.67}$$

The loitering condition of an aircraft is the speed that gives the maximum endurance. The lift to drag coefficient relationship that defines this condition is a combination that maximizes equation (4.68).

$$\left(\frac{C_L^{3/2}}{C_D} \right)_{\max} \tag{4.68}$$

This condition can be estimated as given by equation (4.69).

$$\frac{C_L^2}{\pi e \mathrm{AR}} = 3C_{D,0} \tag{4.69}$$

The parasite drag coefficient was obtained from the dash analysis so equation (4.69) thus estimated the lift coefficient at the loiter condition. Since the aircraft weight was known the loiter airspeed could be estimated. At this point the drag force at loiter could also be calculated so that the thrust required to maintain level flight at the loitering airspeed was known. The loiter propeller was optimized using this required thrust as the constraint. One of the results of this optimization is the propeller power coefficient during loiter, which is the value shown in Table 4.6.

With the operating environment for the dash and loiter flight conditions defined and an optimized twist distribution for each case obtained, the performance of each propeller was evaluated. As was described in the analysis, in the dash propeller optimization the power coefficient was used as a constraint in order to determine the thrust required for this condition. However, when analyzing the propellers the thrust coefficients shown in Table 4.6 were used as a constraint so that the required power in each case could be compared. Table 4.7 shows the results of the performance evaluation, where the performance of a propeller with a generic $1/r$ twist distribution is also given just as a reference point. A propeller optimized for the loitering flight condition, and operating at this state, showed a significantly lower power requirement to produce the required thrust compared to the dash optimized propeller. The efficiency of the loiter propeller was also about 4.3% higher in loiter than the dash propeller. Considering the high speed dash operating state, it can be observed that the power required to produce the

necessary thrust was lower for the dash optimized propeller than the loiter propeller, and the efficiency of the dash propeller was about 3.7% higher. The difference in the performance of the two propellers can be more appreciated when considering the shaft horse power required in order to deliver the requisite thrust for each flight state. The dash propeller was estimated to need about 11 additional horsepower to produce the necessary loitering thrust, but in the high speed cruise case the dash propeller would need about 38 horsepower less than the loiter propeller.

TABLE 4.7

PERFORMANCE RESULTS OF THE LOITER/DASH MISSION ANALYSIS

	C_T	Optimized for:		Generic 1/*r* Twist
		Loiter	**Dash**	
Operating at:	**Loiter**	0.0491	0.0491	0.0491
	Dash	0.0930	0.0930	0.0930
	C_P	**Loiter**	**Dash**	
Operating at:	**Loiter**	0.0467	0.0494	0.0474
	Dash	0.2211	0.2117	0.2332
	η	**Loiter**	**Dash**	
Operating at:	**Loiter**	0.7866	0.7429	0.7757
	Dash	0.8430	0.8804	0.7992
Horsepower		**Loiter**	**Dash**	
Operating at:	**Loiter**	187.44	198.48	190.07
	Dash	887.44	849.70	936.13

The analysis clearly suggests that there is potential to improve an aircraft's performance by means of a variable twist propeller when the mission is of the loiter-dash type. The reader is reminded that the observed difference between the two propellers are within the capability of the aerodynamic model as discussed at the end of Section 3.3 It is also important to consider the optimum twists for the two operating states to know how large a change in blade twist would be necessary to realize the performance gains discussed. Figure 4.8 is a plot of the two resulting blade twists. There is quite a large difference between the two twist distributions, with the maximum difference of around eight degrees being found at the 0.4*R* location. The difference in the twists is not considered to be prohibitively large for the proposed variable blade twist concept, but once again, it rules out the use of many of the smart materials discussed earlier.

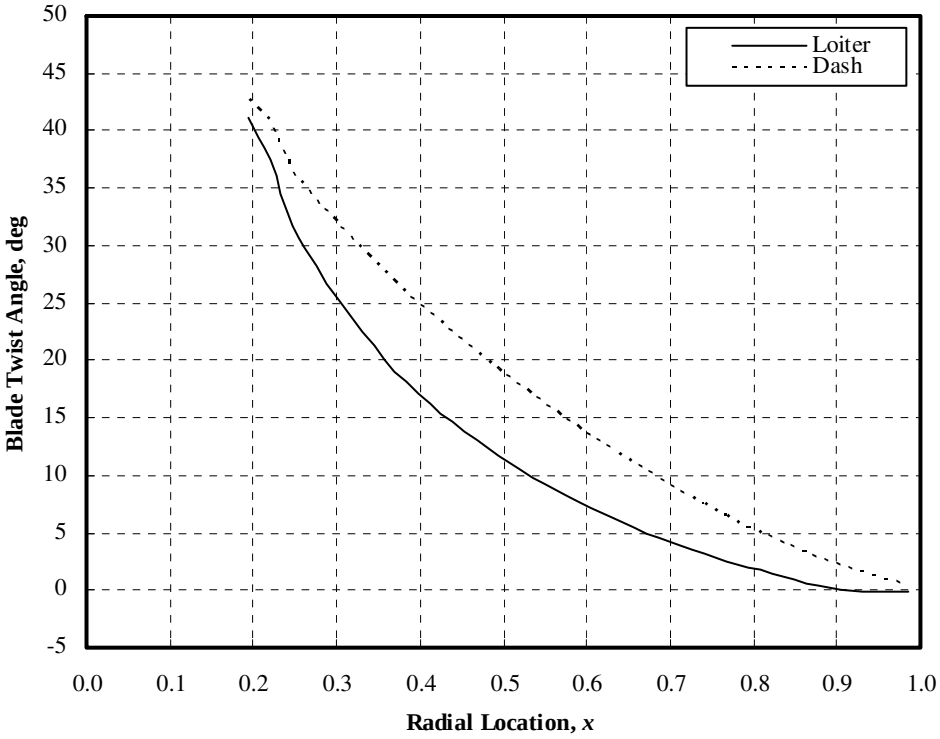

Figure 4.8. Loiter and dash twist distributions.

4.6 Chapter Summary

This chapter covered constrained and unconstrained propeller blade twist optimization. The method for solving for the blade twist distribution, $\beta(x)$, was validated against previously published results. Evaluation of the results from both the unconstrained and constrained optimization suggested a mission profile for which active blade twist control would be viable. Based on the observations made in the results sections, a loiter-dash mission profile was selected as a potential candidate for such a technology. The results of the low speed loiter and high speed dash analyses were very promising. It was noted that the difference in the optimum twists between the two optimized propellers could potentially be attained by an active twist control mechanism.

CHAPTER 5

STRUCTURAL AND POWER CONSIDERATIONS

5.1 Introduction

The purpose of this chapter is to introduce some practical considerations associated with a morphing blade structure. The first of these considerations is a structural analysis of two blade morphing concepts proposed at the close of the literature review given in Chapter 2. The objective of the structural analysis is simply to show that the induced strain capabilities of shape memory alloys are sufficient to give the desired amount of shape change. The second consideration is the power that would be required to actuate a morphing propeller. Power requirements will be combined with the optimization results of Chapter 4 to assess whether a morphing propeller would still offer a performance benefit with actuation costs included. This chapter then closes with a summary of the findings of the structural and thermal analyses.

5.2 Structural Analysis

In the literature review of morphing structures presented in Chapter 2, it was concluded that either the entire section camber morphing concept or a tension-torsion coupled blade structure are possible solutions for a morphing propeller blade. In this section these two concepts will be evaluated more closely. A simplified analysis of the entire section camber morphing concept will first be presented, followed by a more detailed presentation of results published in the literature for tension-torsion coupled structures. The latter discussion of published results is done in lieu of designing and analyzing a tension-torsion coupled blade since the goal is to establish the viability of the concept for propeller blade morphing.

5.2.1 Entire Section Camber Morphing Analysis

The particular arrangement of the entire section camber morphing concept to be evaluated in this subsection is one with a shape memory alloy strip bonded to the bottom of the airfoil. When the SMA is heated it contracts, causing an increase in the blade camber. Now, in order to achieve the desired change in blade twist by means of camber variation, only the trailing portion of the blade will have the SMA bonded to it. The schematic in Figure 2.5 is given to clarify how a trailing edge deflection achieves a change in blade twist. In this figure the desired change in the local blade angle is given as an effective change in angle of attack, $\Delta\alpha$. To get this desired change in the angle of attack, the trailing edge will need to deflect through some angle, θ_{flap}. The first part of the analysis of the camber morphing concept is thus to determine this required flap angle along the span of the blade. This angle is needed because the structural part of the analysis will focus on assessing whether the desired flap angle can be achieved by a shape memory alloy bonded to the propeller blade.

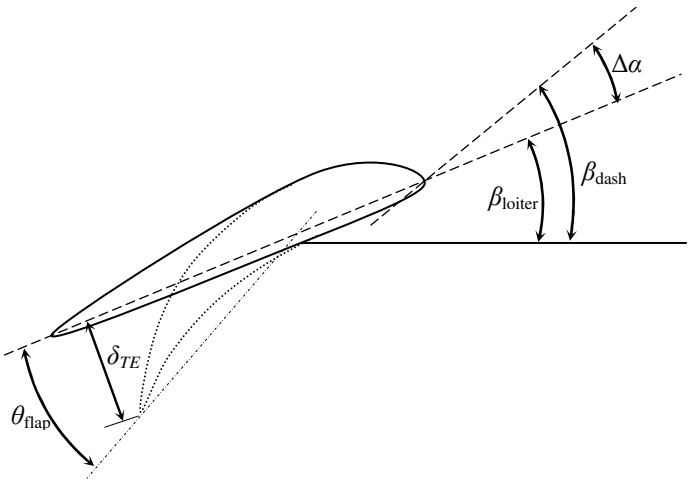

Figure 5.1. Schematic of a trailing edge deflection for a twist change.

Method of Analysis – Flap Deflection Angle

The increment in the lift coefficient due to a trailing edge flap deflection can be predicted by thin-airfoil theory as presented in reference [133]. The effective change in the angle of attack

can then be determined from this lift coefficient increment if the airfoil lift-curve slope, $C_{L,\alpha}$, is known. Equation (3.37) is the thin-airfoil theory result given in reference [133] with the lift increment written in term of an angle of attack increment.

$$C_{L,\alpha}\,\Delta\alpha = \left[2(\pi - \xi_h) + 2\sin\xi_h\right]\theta_{\text{flap}} \tag{5.1}$$

The angle, ξ_h, denotes the location of the flap hinge along the airfoil chord; the angle, ξ, is related to a chord-wise coordinate, ζ, by equation (5.2). The coordinate, ζ, is defined to be zero at the leading edge and increases towards the trailing edge of the airfoil.

$$\zeta = \frac{1}{2}c(1 - \cos\xi) \tag{5.2}$$

The change in angle of attack, $\Delta\alpha$, is taken to be equal to the difference between the loiter and dash blade twist angles at a particular radial location. Thus, if the chord-wise flap hinge location is known, the flap deflection angle can be calculated.

For the structural analysis it is more convenient to use the displacement of the trailing edge perpendicular to the chord-line, δ_{TE}. This displacement, which is illustrated in Figure 2.5, is determined from the deflected flap geometry as given by equation (5.3).

$$\delta_{TE} = (1 - \zeta_h)\sin\theta_{\text{flap}} \tag{5.3}$$

Trailing Edge Deflection

For the arrangement considered here the flap hinge was assumed to be located at the 40% chord point, and the change in angle of attack was determined from the results presented in Figure 4.8. Figure 5.2 is a plot of the desired change in angle of attack along the span of the blade, the flap deflection angle required to achieve this angle of attack increment, and also the required displacement of the trailing edge. The maximum required trailing edge displacement was at the 0.44*R* radial location with a magnitude of 21.86 mm. The objective of the structural

analysis is to determine if it is possible for a shape memory alloy bonded to the surface of a propeller blade to cause a trailing edge deflection of equal magnitude.

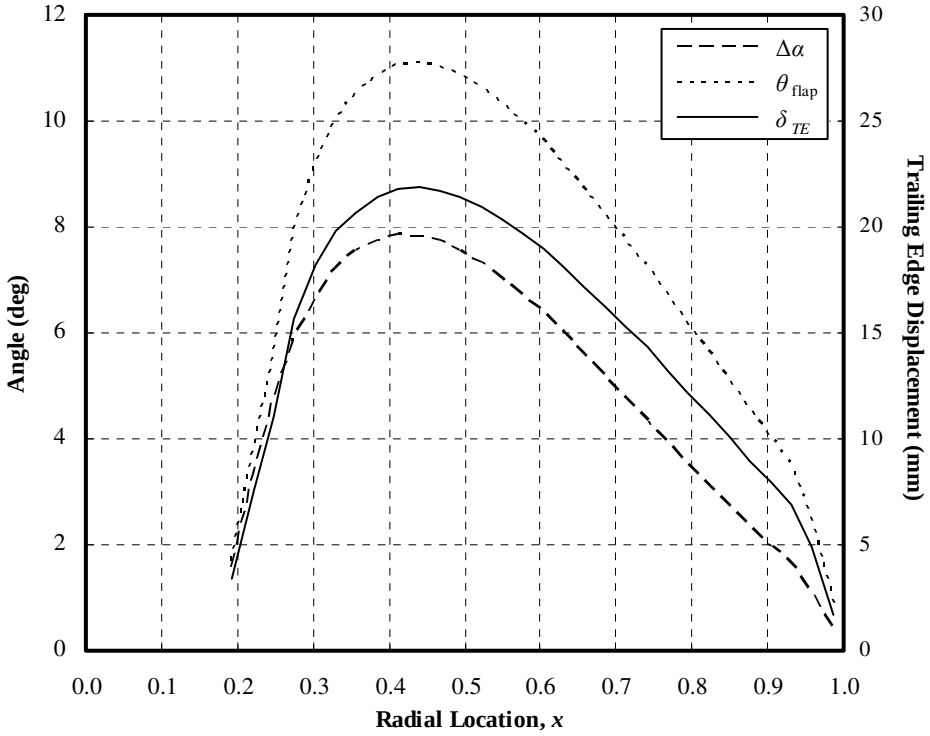

Figure 5.2. Desired flap angle and trailing edge displacement.

Structural Analysis – Problem Setup

As was already mentioned, the structural analysis performed here is aimed to simply show that the strain capabilities of shape memory alloys are sufficient to produce the desired trailing edge deflections. To simplify the analysis the geometry of the propeller is reduced to that of a flat plate with dimensions corresponding to the loiter-dash propeller blade optimized in the previous chapter. The length of this plate is equal to the distance from the blade hub to tip, and the width equal to 0.6 of the blade chord. This width is equal to the chord length of the flap used to determine the necessary trailing edge deflections. The thickness of the plate is set equal to two-thirds of the blade thickness at the radial location of maximum deflection. The reason for using a thickness less than the actual blade thickness is to account for the tapering of the airfoil

thickness towards the trailing edge. The geometry of the propeller blade and flat plate discussed here is illustrated in Figure 5.3 (a) and (b).

The boundary conditions for the flat plate analysis are also shown in Figure 5.3 (b). At the blade root, and along the side of the plate that connects to the leading edge portion of the blade, clamped boundary conditions are enforced. The other two sides of the plate are treated as free edges. Figure 5.3 (c) shows the geometry of the plate cross-section, showing a SMA sheet bonded to the bottom surface. The total thickness of the plate is fixed in the analysis, but the fraction of the total thickness taken up by the SMA is variable. This is therefore a parameter that needs to be evaluated to determine a sufficient SMA thickness to attain the desired trailing edge deflection. An excessive SMA thickness would make the camber morphing concept impractical.

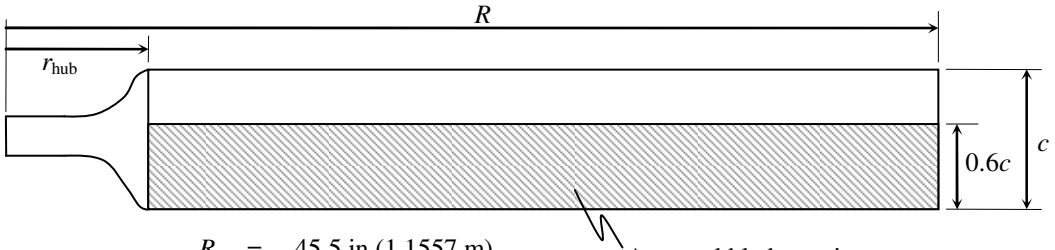

R = 45.5 in (1.1557 m)
r_{hub} = 8.17 in (0.2075 m)
c = 7.45 in (0.1891 m)

(a) Propeller blade geometry

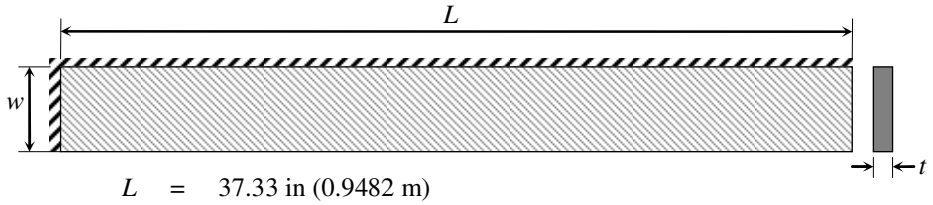

L = 37.33 in (0.9482 m)
w = 4.47 in (0.1135 m)
t = 0.425 in (0.0108 m)

(b) Plate geometry

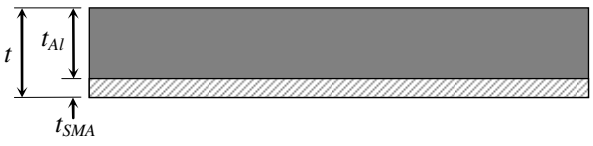

(c) Plate cross-section

Figure 5.3. Propeller blade, plate, and plate cross section geometry.

The propeller blade is assumed to be constructed from aluminum. The reason for using aluminum for the analysis rather than considering a composite laminate is, firstly, to hold with the objective of a simple analysis to demonstrate the sufficiency of the strain capability of SMA. Another reason is the amount of variability that is possible in the layup of laminated structures which can greatly affect the material properties in the various coordinate directions. Since the goal is not to design a composite laminate propeller blade, as would be needed to be able to perform a structural analysis, considering a laminated structure for the present analysis is seen as unnecessary. The physical properties of the aluminum and Nickel-Titanium SMA in the Austenite phase that is used in the analysis are given in Table 5.1.

TABLE 5.1

MATERIAL PROPERTIES

Material	Young's Modulus ksi (GPa)	Poison's Ratio
Aluminum	10.5 (72.4)	0.33
Nickel-Titanium	12.0 (83)	0.33

Structural Analysis – Finite Element Model

Analysis of the described flat plate problem makes use of the finite element method. Nastran is used for the finite element analysis and the flat plate is modeled in Patran. Shell elements are used to model the two layers of the plate. The neutral axis of the aluminum plate is placed on the *x-y* plane, and the neutral axis of the SMA plate is offset from the *x-y* plane by half of the total thickness. This offset places the SMA sheet such that it is in contact with the aluminum plate but does not overlap with it. To prevent Nastran from treating the elements in the two layers as separate unconnected entities, the two shell element layers have to share nodes. If each layer has its own set of nodes, the two layers will deform independently from one another under an applied load.

Modeling of the strain response of SMA when it is heated to above the Austenite finish temperature is accomplished by applying a uniform thermal load to the flat plate along with artificial coefficients of thermal expansion. The aluminum plate is given coefficient of thermal expansion equal to zero, while the coefficient of thermal expansion of the SMA is set equal to −0.005 /ºC. This artificial expansion coefficient for the SMA was calculated such that a 5% compressive strain would result when a uniform thermal load of 10 ºC above a reference temperature is applied. Shape memory alloys are capable of generating induced strains of up to 7%, so a 5% strain is within the material's capabilities. It should be clearly noted that the actual response of an SMA to heating is not modeled here. This described model is simply a manner in which to apply a compressive strain to the SMA in the finite element model.

Structural Analysis - Results

Before presenting the finite element results from the described model, results from a validation run will first be given. For validation, the deflection and the radius of curvature of a simply supported bimetallic beam were evaluated analytically and numerically and compared. An analytical result was obtained from the bimetal theory introduced by Timoshenko in 1925 [134]. In the bimetal theory two dissimilar metals are assumed to be bonded to one another and subjected to a thermal load. Due to the differences in the metals' coefficients of thermal expansion a bending moment is generated causing the beam to bend. The manner in which the thermal load enters the analysis is by means of a thermal strain. So, for the arrangement of a SMA bonded to the bottom surface of an aluminum beam, the deflection and radius of curvature were determined by assigning a 5% compressive thermal strain to the SMA and zero thermal strain to the aluminum. In the finite element modeling of this bimetal beam the same method was used as described for the flat plate; the only difference was that 1-D beam elements were

used instead of the 2-D shell elements. The beam dimensions corresponded to the flat plate geometry: the length of the beam was set equal to the width of the plate, and the combined (aluminum and SMA) height of the beam equaled the total thickness of the plate. The beam was given a unit width, and the thickness fraction of the SMA was set to be 10% of the total thickness.

Table 5.2 shows the model validation results where the maximum deflection and radius of curvature obtained from the two solutions are compared. For the simply supported beam with a pin support at one end and a roller support at the other, the maximum deflection occurred at the mid-point. As can be seen in the table the finite element solution agreed closely with the analytical one, with difference of approximately 6%. Equally close agreement in the radius of curvature results are also observed. The finite element model was therefore considered to be validated and the results from the flat plate analysis were considered to be reliable.

TABLE 5.2

COMPARISON BETWEEN ANLYTICAL AND FINITE ELEMENT BEAM SOLUTIONS

Solution Type	Maximum Deflection (mm)	Radius of Curvature (mm)
Analytical	4.416	366.63
Finite Element	4.389	368.80

For the flat plate analysis the desired result was a trailing edge deflection that was close to the maximum required at a span-wise location of 0.44*R*. Thus it was first necessary to determine the thickness fraction of the SMA that would give this deflection. A 10% SMA thickness fraction was found to be sufficient and produced a deflection of 22.85 mm at a position corresponding to the 0.44*R* radial location. Figure 5.4 is a plot of the deflections of the trailing edge of the plate due to a compressive induced strain in the SMA of 5%. The desired trailing

edge displacement from Figure 5.2 is also plotted in Figure 5.4 to compare with the results of the flat plate analysis.

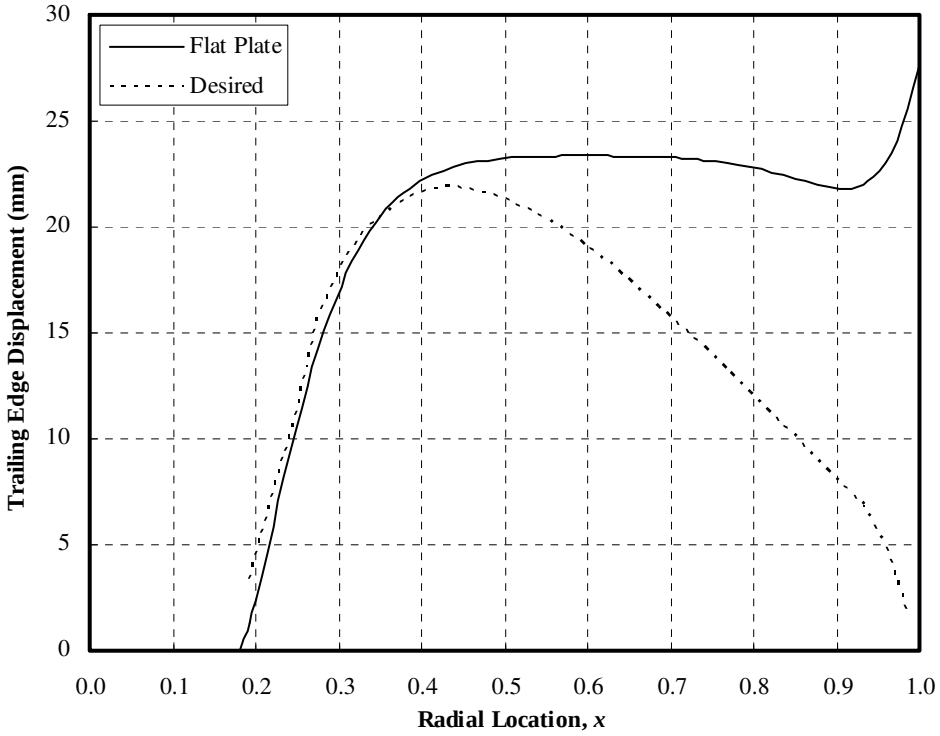

Figure 5.4. Trailing edge displacement of flat plate.

As can be seen in the figure above, the strain capabilities of the SMA was more than sufficient to attain the desired trailing edge deflections. With just a 10% thickness fraction, the maximum desired deflection was exceeded. In fact, outboard of the 0.44*R* radial location, the flat plate analysis shows that the thickness fraction of the SMA can be greatly reduced since the predicted deflections far exceeded what was required. The portion of the flat plate inboard of the location of the desired maximum showed a steep slope from a zero deflection at the plate boundary. This slope agreed well with the desired inboard deflections, though not too much can be drawn from this agreement due to the much simplified geometry of the flat plate compared to the complex blade geometry. Near the free edge of the plate corresponding to the blade tip, the results a showed a decrease in the deflection followed by a sharp increase toward the blade tip.

This result is believed to be an artifact of the modeling of the SMA as a continuous sheet. The flat sheet model generates a compressive strain along both the width and length of the plate instead of only along the plate width as is desired. Though this is a modeling inaccuracy, it only shows up near the free edge of the plate. Away from the free edge at the blade tip the strain along the plate length does not contribute to the trailing edge deflection, and at these locations it is clear that SMA can generate sufficient induced strain to give the desired trailing edge deflections.

At this point the objective of the camber morphing analysis to show that shape memory alloys generate sufficient strain has been satisfied. The results clearly show that the desired trailing edge deflections can be achieved. However, an issue that was encountered in the analysis needs to be discussed. This issue has to do with the stresses generated in the plate. Obviously a 5% strain is a very large strain for the material to which the SMA is bonded to sustain, and although the stiffness of the aluminum plate prevents the SMA from achieving the full 5% strain, the strains generated in the aluminum were still very high, resulting in excessively large stresses. What this result suggests is that simply bonding the SMA to a solid aluminum blade is not a realistic solution. Instead, a compliant trailing edge structure will need to be designed specifically for a morphing propeller blade to prevent such high stresses. Such a design is, however, beyond the scope of the present research. This issue with the large stresses also does not invalidate the previous conclusion that SMA generates sufficient strains, it only shows that careful and innovative design will be needed for a morphing propeller blade.

5.2.2 Tension-Torsion Coupled Blades

A propeller blade structure with anisotropic material characteristics, designed in such a way that tensile forces induce twisting moments, is evaluated in this section. As was mentioned

earlier, a structural analysis of this concept is not performed. In order to accurately assess a tension-torsion coupled propeller blade it is necessary to define the composite laminate material layup. Such design of a propeller blade is currently beyond the scope of the research. As such, the evaluation of this concept instead relies on published experimental and analytical results to assess the amount of twist that one might expect to achieve from tension-torsion coupling. Some of the published works discussed here have already been described in the literature review of Chapter 2, but the focus in this section is on the quantitative results obtained by these researchers rather than describing the blade morphing methods.

In one of the previously discussed papers, Bernhard and Chopra [85] considered an active rotor blade tip actuated by a tension-torsion coupled beam housed inside the blade structure. This concept was evaluated on a hover test stand at an angular speed of 930 RPM. The rotor diameter was 1.83 m and the length of the active beam was 0.546 m. At an actuation frequency of two-per-revolution the amplitude of the blade tip deflection was 1.8 degrees. At higher frequencies approaching the torsional natural frequency of the beam of about five-per-revolution, the tip deflection increased. At four-per-revolution excitation a deflection amplitude of 2.25 degrees was achieved. The results from this paper are summarized in Table 5.3 where the maximum measured deflection per unit length is given. Results from two other studies that are discussed below are also shown in this table.

Bernhard and Chopra only considered vibratory excitation, so steady one-way twist deflection results were not given. Chandra [86], on the other hand, set out to determine the steady state twist deflection that could be obtained from a bending-torsion coupled beam. This beam was actuated by two SMA strips trained to memorize a bending shape.

TABLE 5.3

PUBLISHED TENSION-TORSION RESULTS

Paper	Case	Max. Twist, deg/m (deg/in)	Max. Twist Frequency, Hz	Actuator
Bernhard & Chopra [85]	–	4.12 (0.105)	62	Piezo
Chandra [86]	Gr/E[a], 15º, Experiment	4.11 (0.104)	0	SMA
	K/E[b], 15º, Analytic	11.41 (0.290)	0	SMA
	K/E, 22.5º, Analytic	13.69 (0.348)	0	SMA
Büter, et al. [92]	–	1.40 (0.036)	113	Piezo

[a]Graphite-epoxy [b]Kevlar-epoxy

For a graphite-epoxy beam with a fiber orientation of 15 degrees from the longitudinal axis and an actuated length of 17.25 in, a twist deflection at the end of the beam of about 1.8 degrees was obtained. Analytical results agreed very well with the experimental twist results away from the end of the beam, but the predicted twist deflection at the tip was off by about 0.4 degrees. Analytical predictions for a Kevlar-epoxy beam with a fiber orientation of 22.5 degrees showed a tip twist of about 6 degrees. A drawback of the setup studied by Chandra, from the perspective of direct use for a propeller blade, is that the beam had to bend to achieve the twist deformation. The slopes of the deformed beams were roughly equal to the amount of twist in each case considered. The results from the study performed by Chandra are shown in Table 5.3.

The final paper shown in Table 5.3 was published by Büter et al. [86] in which a variety of blade morphing concepts were considered. A tension-torsion coupled blade was among the concepts considered, and for this case the authors constructed and tested a rotor blade actuated by a piezo stack actuator. The blade was tested at high actuation frequencies in a stationary, non-rotating state but was not run on a test stand. The intended application was for rotor vibration control where high frequency actuation is desired. Results were given for the blade actuated at its torsional-natural frequency since the authors suggested that a tension-torsion

coupled blade should be designed with a torsional natural frequency equal to the desired actuation frequency in order to maximize twist deflections. At the natural frequency of 113 Hz a twist deflection of ±1.9 degrees was measured. This result is also shown in Table 5.3. The size of the blade used in the experiment was, however, not clearly defined in the paper so the length of the blade used to normalize the twist deflection to a per unit length measure was estimated from the authors' description.

To evaluate applicability of the above results to the present case, the desired amount of twist is first reviewed. The maximum increase in blade twist angle was about 7.8 degrees and occurred at the 0.44*R* radial location. This corresponded to a distance of roughly eleven inches from the blade root. From this location outboard, the twist in the blade decreased to about zero at the blade tip. Thus the blade would need to be twisted in one direction over the inboard eleven inches, and then in the opposite direction over the remaining 25 inches by an equal amount. Of the methods discussed above, the first two are considered the most reliable since the geometry of the active members were given in the papers. Both the results published by Bernhard and Chopra and the experimental results of Chandra showed a twist capability of 4.1 degrees per meter, or 0.1 degrees per inch. The amount of twist that would be possible over the first 11 inches of the propeller blade is thus about 1.1 degrees. This is much less than required. It is therefore concluded that the twist deformations required for the performance benefits predicted by the optimization method cannot be realized using a tension-torsion blade structure alone. The required geometry change per unit length is too large. A possibility still remains, however, for combining the tension-torsion coupling with the camber morphing concept. Doing so would reduce the required trailing-edge deflections, but this adds complexity to the design. Of the two

concepts considered here, camber morphing appears to be the best candidate for propeller morphing.

5.3 Thermal Analysis

The optimization results presented in Chapter 4 indicated that a propeller optimized for the loiter flight condition would have a power requirement of 11 hp less than a propeller optimized for the dash flight phase while operating at the low speed loiter condition. Similarly, a reduction of 37 hp in the dash phase of flight could be realized if the blade twist was optimized for this high speed flight condition. These results did not include the power requirements of a blade actuation mechanism. However, to assess the feasibility of a morphing propeller the actuation cost needs to be included. This is the purpose of the thermal analysis section. Here a heat transfer analysis of the camber morphing concept will be presented to assess more accurately the power reductions that a variable geometry propeller blade would offer. The arrangement considered in the analysis is similar to that presented in the structural analysis of the camber morphing concept with an SMA strip bonded to the lower airfoil surface. Shape memory alloys are thermally actuated, and in order for this metal to remain in the actuated state its temperature must be maintained above the Austenite finish temperature. Thus the heat transfer problem is one of determining the power required to maintain a desired SMA temperature, T_S, with heat being lost to the surrounding fluid medium through convection. In the following subsection an explanation of the heat transfer analysis is presented along with a description of the problem setup. This subsection will be followed with a presentation of the results from this analysis.

5.3.1 Method of Analysis

The convective heat transfer problem considered here is aimed to determine the rate of heat flow to the surrounding atmosphere when the temperature of the SMA is kept at some constant value. This is a steady-state heat transfer problem and the rate of heat loss is thus equal to the power required to maintain the desired SMA temperature. With the arrangement considered here the SMA strip is exposed to the flow on the lower airfoil surface, so heat is directly transferred to the fluid. On the upper surface the heat is first conducted through the blade before being transfer to the atmosphere. Before presenting the method for calculating the heat transfer rates from the upper and lower blade surfaces, the geometry and flow conditions are first defined.

Two important factors need to be considered when defining the blade flow conditions. The first is the flow velocity which depends on the advance ratio and radial location along the blade and the second is the atmospheric conditions in which the propeller is operating. Since the flow velocity varies greatly from blade root to tip a similar approach to the blade element method is taken in the heat transfer analysis. The blade is divided into a number of strips along the span, and for each strip the flow velocity is approximated as the velocity at the mid-point. The atmospheric conditions also need to be defined in order to be able to perform the heat transfer calculations. The parameters that are needed are temperature, pressure, and density and can be defined based on pressure altitude from a standard atmosphere table or a prescribed temperature at a particular pressure altitude. The ideal gas law allows for calculating the density based on air pressure and temperature.

The blade cross-sectional geometry is approximated as a flat plate at zero angle of attack. A sketch of the arrangement is presented in Figure 5.5. The plate length, c, and thickness, t, is

related to the blade geometry, the length being equal to the blade chord at the radial location under consideration and the thickness of the plate is equal to two-thirds of the local blade thickness. In keeping with the structural analysis, only the aft 60% of the plate has the SMA bonded to it. The thickness of the SMA strip, t_S, is equal to 10% of the total plate thickness; the remaining blade thickness is denoted by t_B. The unheated length of the plate is indicated by the symbol ξ, and the chord-wise coordinate is denoted as ζ.

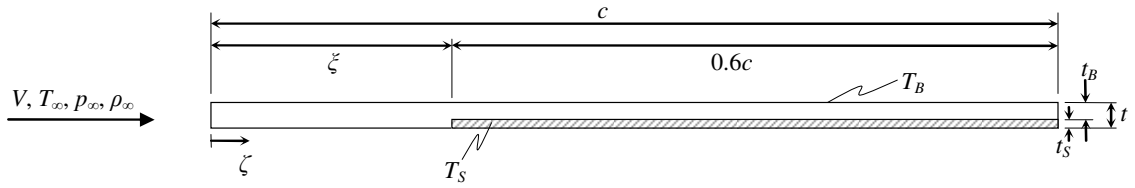

Figure 5.5. Sketch of plate geometry for heat transfer analysis. (Not to scale)

Approximating the blade cross-section as a flat plat is done mainly because empirical heat transfer relationships are readily available for this geometry. A literature search for experimental heat transfer data from airfoils turned up a few reports, but none of these studies matched the geometry of the problem considered here. In one study the authors were only interested in the heat transfer from the leading edge portion of an airfoil [135], and in another they considered the heat transfer over the entire surface of a 21% thick airfoil [136]. Neither of these studies was applicable to thin airfoils with unheated starting lengths. The airfoils over the major portion of the blade span are very thin, so the flat plate approximation is also not far removed from the actual cross-section geometry.

With the problem geometry defined, the method for calculating the rate of heat transfer from the plate is now presented. Standard heat transfer equations are used as would be found in a basic textbook on the subject such as reference [137]. Over both the upper and lower plate surfaces convective heat transfer takes place, thus the discussion begins with convection. The local heat flux, q'', can be determined from knowledge of the local convection coefficient, h,

local surface temperature, T, and the free stream temperature, T_{∞}. The relationship for calculating the heat flux is expressed by equation (5.4).

$$q'' = h(T - T_{\infty}) \tag{5.4}$$

Heat flux has units of power per unit area (i.e. $W \cdot m^{-2}$), and the convection coefficient has units of power per unit area per unit temperature (i.e. $W \cdot m^{-2} \cdot K^{-1}$). Two things need be determined in order to calculate the local heat flux – the surface temperature and the convective heat transfer coefficient. For the lower plate surface, aft of the unheated portion, the surface temperature is predefined as the desired SMA temperature. The surface temperature over the upper surface has to be calculated using convection and conduction relationships. The convection coefficient is determined from flow conditions over the plate using empirical relationships. The condition of the boundary layer, whether turbulent or laminar, greatly influences the convection coefficient. In Chapter 3 a turbulent boundary layer was assumed from the blade leading edge, and the reasons for this assumption were also given.

With the boundary layer defined, the manner in which the analysis proceeds is to first obtain the local Nusselt number from empirical relationships. Nusselt number is the ratio of the convection coefficient to the thermal conductivity, k, of the fluid and is defined in equation (5.5).

$$Nu_{\zeta} = \frac{h\zeta}{k_f} \tag{5.5}$$

The subscript, f, on the thermal conductivity indicates that this parameter is to be determined based on the film temperature, T_f, which is taken to be the average of the surface and freestream temperatures, equation (5.6).

$$T_f = \frac{T + T_{\infty}}{2} \tag{5.6}$$

The local Nusselt number for a turbulent boundary layer is as given by equation (5.7).

$$Nu_\zeta = 0.0296\,\mathrm{Re}_\zeta^{4/5}\,\mathrm{Pr}^{1/3} \tag{5.7}$$

The Nusselt number depends on the Prandtl number, Pr, and the Reynolds number, Re_ζ, defined by equation (5.8).

$$\mathrm{Re}_\zeta = \frac{\rho_f V \zeta}{\mu_f} \tag{5.8}$$

In this equation the subscript, *f*, again indicates that the parameters are to be evaluated at the film temperature. The Prandtl number is determined from tabulated air properties and has a strong dependence on air temperature and a weak dependence on pressure.

The Nusselt number given by equation (5.7) is based on the assumption that the entire plate surface is heated so that the thermal boundary layer develops from the leading edge onwards. In the case considered here the thermal boundary layer only begins to develop from the point where the SMA strip starts. To account for the unheated starting length, a correction is applied to equation (5.7). The corrected Nusselt number is given by equation (5.9).

$$Nu_\zeta = \frac{Nu_\zeta\big|_{\xi=0}}{\left[1-(\xi/\zeta)^{9/10}\right]^{1/9}} \tag{5.9}$$

Once the local Nusselt number is calculated the local convection coefficient is found from equation (5.5). This allows for the calculation of the local heat flux. To find the heat transfer rate from the blade strip under consideration, the local heat flux has to be integrated over the heat transfer area of the strip. This area integral, given by equation (5.10), is simplified by recalling that all the geometric and flow properties are approximated as being constant across the width of the blade strip. So, the integral only has to be taken over the length of the heated portion of the plate. This integral is evaluated numerically.

$$q = \int_{A_p} h(T - T_\infty)\,dA_p = w\int_\xi^c h(T - T_\infty)\,d\zeta \tag{5.10}$$

The surface temperature, T, over the lower surface is equal to the predefined desired SMA temperature, T_S, but the surface temperature over the upper surface, T_B, needs to be determined before the heat transfer rate from the upper surface can be calculated. For this the heat conduction through the plate has to be considered. The one-dimensional heat flux is expressed by equation (5.11).

$$q'' = \frac{k}{t_B}(T_s - T_B) \tag{5.11}$$

The heat flux through the blade has to be balanced by the heat flux to the atmosphere; therefore, equations (5.4) and (5.11) are equal to one another as given by equation (5.12).

$$h(T_B - T_\infty) = \frac{k}{t_B}(T_s - T_B) \tag{5.12}$$

From this equation the upper surface temperature, T_B, is solved for and the result is shown by equation (5.13).

$$T_B = \frac{kT_S + ht_B T_\infty}{k + ht_B} \tag{5.13}$$

Substituting this equation into equation (5.4) gives the local heat flux from the upper surface in terms of the SMA and freestream temperatures, equation (5.14).

$$q'' = kh\left(\frac{T_S - T_\infty}{k + ht_B}\right) \tag{5.14}$$

Equation (5.14) is integrated over the heated upper surface area of the plate to determine the heat transfer rate from the blade element under consideration. Thus, at this point the heat transfer rates from both the upper and lower surfaces of the plate are known. The sum of these two values gives the total heat transfer rate from the blade strip under consideration. As described above, the heat transfer rate from each blade strip is calculated and then summed to determine the heat transfer rate from the entire blade. To find the total heat transfer rate from the

propeller the rate of heat transfer from one blade is multiplied by the number of blades in the propeller.

5.3.2 Results and Discussion

To be able to calculate the heat transfer rates a few parameters had to be defined first. These were the SMA temperature, T_S, the flight condition (advance ratio) in which the blades were to be actuated, the blade material and conductivity, and the atmospheric conditions. The phase transition temperatures of an SMA depend on the exact chemical make up of the metal, with the possibility of varying this temperature from below freezing to as high as 110 ºC. Thus the desired SMA temperature to use in the thermal analysis offered some flexibility and was thus a variable. The phase transition temperature needs to be high enough so that an undesirable passive actuation would be unlikely and the controllability of the blade shape could be maintained. An excessively high phase transition temperature is also undesirable as it would increase the power requirement. For the present analysis the SMA temperature was varied from 60 to 85 ºC.

The flight condition in which the blade was to be actuated was assumed to be the high speed dash phase. The reason for this was two-fold. Firstly, the power reduction offered by an optimized twist was greater in the dash phase thus providing more available power for actuating the propeller blade while maintaining a performance benefit. Secondly, more time was assumed to be spent in the loiter phase so an actuated blade in this flight phase would lead to a higher overall energy consumption.

The blade material properties that were used in the analysis were those of Kevlar [138] which has a thermal conductivity of 0.04 $W \cdot m^{-1} \cdot K^{-1}$. Kevlar is a common aerospace material, and propellers are also commonly manufactured as laminated composites using Kevlar fibers.

The atmospheric conditions in which a propeller operates vary over a wide range of temperatures and altitudes. Therefore, the required power was estimated over a range of altitudes using the standard atmosphere model to determine pressure, temperature, and density, and then also over a range of freestream temperatures at sea level pressure. Figure 5.6 is a plot of the estimated actuation power for altitudes from sea level to 35,000 ft and for different SMA temperatures.

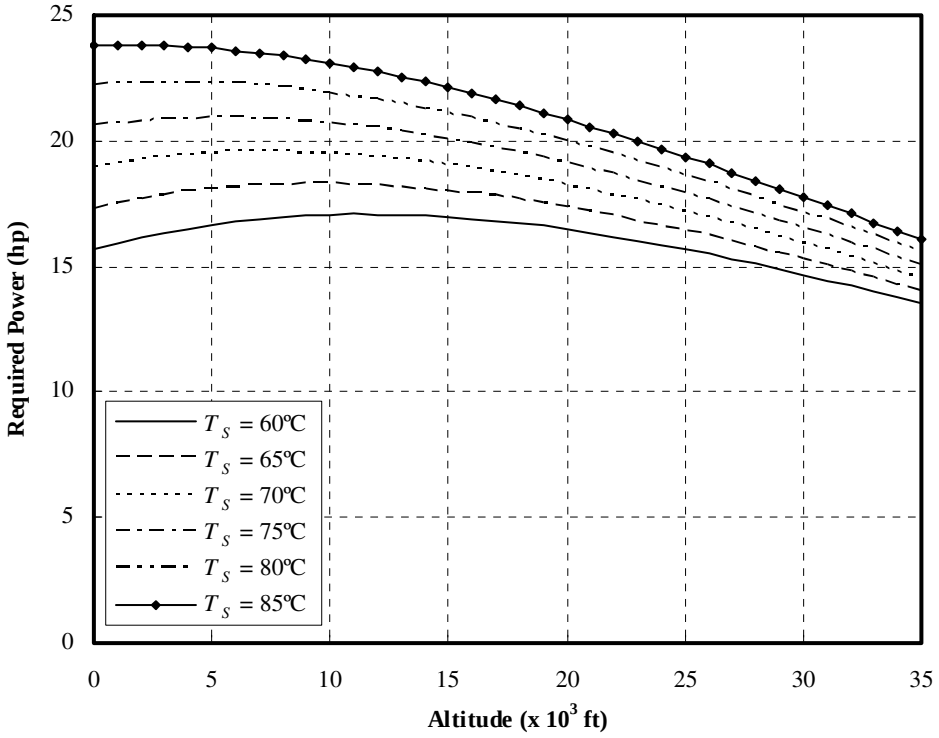

Figure 5.6. Altitude and SMA temperature effect on required power.

As was expected, increasing the SMA temperature increased the required power. The altitude at which the maximum power requirement occurred also depended on the SMA temperature. With the SMA maintained at a temperature of 60 ºC, a maximum power requirement of 17.1 hp occurred at 11,000 ft, whereas for an SMA temperature of 85 ºC the maximum power required was 23.8 hp at 1,000 ft. It is interesting to note that the power requirement decreased with increasing altitude above 11,000 ft for cases. The reason for this is the rapid decrease in air

density with altitude resulting in a decreasing Reynolds number and, by equation (5.7), a decreased Nusselt number. Under standard atmospheric conditions, and for all the SMA temperatures considered, the required power was less than the 37 hp performance benefit predicted in Chapter 4.

Figure 5.7 is a plot of the estimated required power over a range of freestream temperatures at sea level pressure. Freestream temperature had a large effect on the actuation power requirements, with the required power increasing with larger temperature differences between the SMA and the freestream. The worst case scenario in terms of required power for actuation was cold temperatures at low altitudes. At a temperature of 30 ºC below zero at sea level the required power was 37.6 hp to maintain an SMA temperature of 75 ºC. A temperature of −30 ºC in the standard atmosphere occurs at about 23,000 ft. At this altitude, with an SMA temperature of 75 ºC, the required power was only 18.4 hp. The reason for the significantly higher power requirement at low altitudes was a higher air density. The results shown in Figure 5.7 clearly indicate that at extreme cold temperatures the actuation cost could be equal to, and even exceed, the performance benefit offered by a morphing propeller. However, such extreme temperatures are not commonly encountered at sea level. At temperatures above the extremely cold values, the results indicate that the required power would be less than the power benefit from an actuated propeller blade.

The following example is given as an illustration. The results presented in Chapter 4 indicated that a propeller optimized for the loiter flight phase would require 887 hp to produce sufficient thrust to propel the aircraft to 300 kts in the dash phase. If the blade was optimized for high speed flight 850 hp would have been sufficient to reach 300 kts.

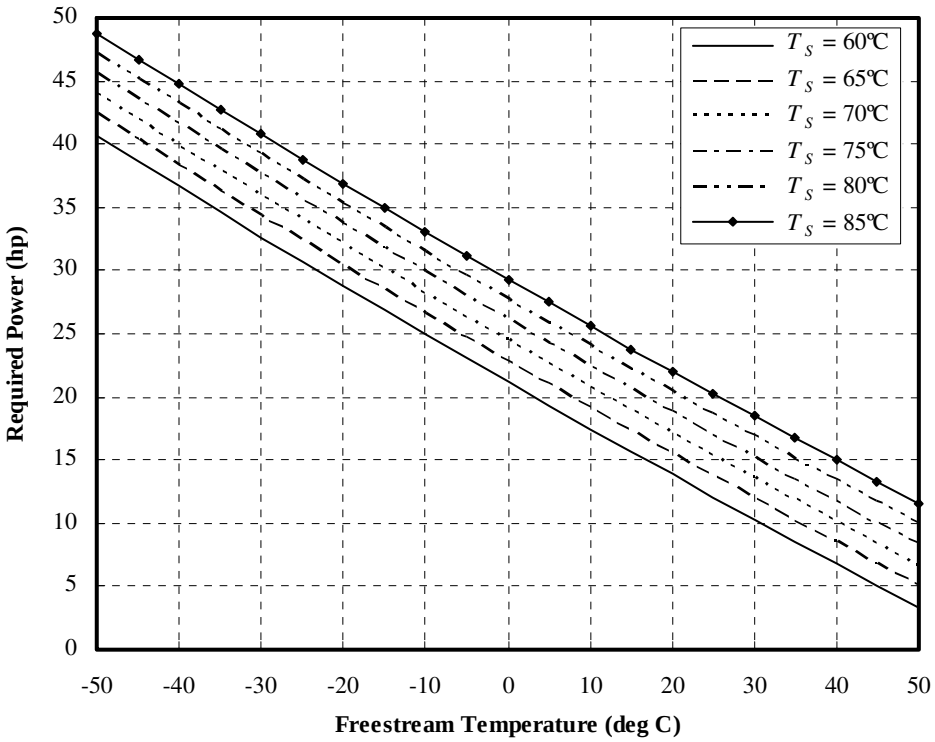

Figure 5.7. Freestream and SMA temperature effect on required power.

If the loiter optimized propeller could be morphed into the dash optimized propeller shape, the power required to fly at 300 kts would be equal to 850 hp plus the actuation power requirement. With the aircraft operating at 20,000 ft under standard atmospheric conditions, and an SMA temperature of 75 ºC, the actuation power was estimated to be 19.1 hp. Thus the total power required to propel the aircraft at 300 kts would be approximately 869 hp, 18 hp less than an un-actuated loiter optimized propeller. This 18 hp power reduction means a reduced energy consumption which directly translates into a fuel savings. The specific fuel consumption of a typical turbine engine, such as the Pratt and Whitney Canada PT-6A-64, is about 0.52 lb/hp/hr [139]. The 18 hp power reduction thus translates into a fuel savings of 9.4 lb/hr, or 1.4 gal/hr, over a fixed geometry propeller.

Naturally the question of why not just use a dash optimized propeller that does not have morphing capabilities arises, since only 850 hp would be needed to fly at 300 kts compared to

869 hp for a morphing propeller. The reason is that this would incur a power penalty of 11 hp during the flight phase in which the aircraft would be operating for the majority of its time in the air. This 11 hp penalty leads to an increased fuel consumption of 5.7 lb/hr (0.85 gal/hr). These power and fuel burn numbers are summarized in Table 5.4 Now, there would be a break-even point, where if the aircraft spent a large enough portion of the flight time operating at high speed it would be better to have a dash optimized propeller without the capability to vary its geometry. This was estimated by noting that a morphing propeller would require 19 additional horsepower, or consume 9.9 lb/hr (1.48 gal/hr) more fuel in the dash phase of flight. The break-even point was thus estimated to occur at a loiter time of 63 % of the total flight time. As long as the aircraft spends more than 63 % of its flight time in the loiter phase a reduced overall fuel consumption could be realized with a morphing propeller.

TABLE 5.4

MORPHING PROPELLER PERFORMANCE COMPARISON

Operating State	Loiter Propeller		Dash Propeller		Morphing Propeller	
	Power Req. (hp)	Fuel Burn (gal/hr)	Power Req. (hp)	Fuel Burn (gal/hr)	Power Req. (hp)	Fuel Burn (gal/hr)
Loiter	187.44	14.53	198.48	15.38	187.44	14.53
Dash	887.44	68.77	849.70	65.85	868.80	67.33

In conclusion then, the thermal analysis results indicated that the power required to maintain the SMA above the actuated Austenite finish temperature is less than the power reduction offered by a morphing propeller over the majority of operating conditions. Only at extremely low temperatures at low altitudes does the actuation power approach, and become greater than, the power reduction due to morphing blades. A further interpretation of the heat transfer results showed that a morphing propeller would offer a reduced fuel consumption as long as more than 63 % of the total flight time is spent loitering. The heat transfer analysis thus

showed a morphing propeller is a feasible concept from an energy and fuel consumption standpoint.

5.4 Chapter Summary

The purpose of this chapter was to investigate some practical aspects relating to a morphing aircraft propeller. The first consideration was the blade structure where the goal was to assess whether shape memory alloys could provide sufficient induced strain to produce the desired amount of shape change. Two morphing concepts were considered – morphing the entire section camber and the tension-torsion coupled blade structure. For the camber morphing concept it was assumed that the trailing 60 % of the blade chord would have an SMA bonded to it to induce a trailing edge deflection. The objective of the finite element analysis of this arrangement was to show that the desired trailing edge deflections would be possible with the strain capabilities of SMA, and the results were found to be in the affirmative. The results did, however, show the stresses induced in the blade to be excessively large, leading to the conclusion that the simple concept of bonding an SMA to a blade not specifically designed to allow for trailing edge deflections is not a viable solution.

The tension-torsion coupled blade structure analysis drew from results published in the literature to assess this concept. Published results showed that an induced twist of about 4.1 deg/m is possible. Using this result it was shown that the desired amount of twist change would not be possible with a tension-torsion coupled blade structure alone. This concept would have to be combined with another shape change method to produce the desired amount of shape change.

Finally, a thermal analysis was performed in order to estimate the actuation power requirements of a morphing propeller. The results indicated that the power requirements to actuate a shape change in a propeller would be less than the power reduction offered by a

propeller with a shape optimized for high speed flight. This was true for most atmospheric conditions other than extreme cold temperatures at low altitudes. The final result of the thermal analysis estimated that as long as an aircraft spent more than 63 % of its total flight time loitering, a morphing propeller could reduce fuel consumption.

CHAPTER 6

CONCLUSIONS AND FUTURE WORK

6.1 Conclusions

The object of this research was to assess the feasibility of morphing aircraft propeller blades with the primary focus being the aerodynamic performance benefits that such technology would offer. The majority of the research focused on the development and implementation of a propeller performance prediction tool and a blade optimization scheme. The aerodynamic model used for performance prediction was the blade element method. This classical method was chosen due to its accuracy and small computer resource requirement. Much attention was given to the development of an airfoil aerodynamic model since it was found that the accuracy of airfoil performance parameters directly affect the accuracy of blade element predictions. The airfoil aerodynamic model developed in the process of this research is what sets this propeller aerodynamic model apart from other similar approaches. The airfoil model included the full post stall behavior of both the lift and drag coefficients up to 90 degrees angle of attack. Compressibility corrections were also included. Comparisons between predictions and experimental data showed that the model accurately predicted propeller performance, and also captured blade stall behavior well. A tip Mach number limitation was identified, though, due to compressibility corrections behaving asymptotically at sonic velocities. At helical tip Mach numbers above 0.9 the performance predictions were unreliable.

The validated aerodynamic model formed the backbone of the optimization scheme. For this calculus of variations was used, and Euler-Lagrange equations for both unconstrained and constrained blade twist optimization problems were derived. This same derivation procedure can be followed in order to arrive at the appropriate Euler-Lagrange equations for optimization of

other propeller geometric variables such as blade chord or airfoil camber. The method of solution for the blade twist angle and the Lagrange multipliers from the Euler-Lagrange equations was validated against previously published results. Both the unconstrained and constrained optimizations were applied to a four-bladed propeller with a conventional mission profile of takeoff, climb, and prolonged cruise. The results of the unconstrained twist optimization study showed that for each operating condition (takeoff, climb, and cruise) the maximum efficiency occurred at power coefficients that were significantly lower than what the propeller would be operating at. This suggested that it is simply not possible to attain high efficiencies during high power events such as takeoff unless the blade solidity (chord length or number of blades) is increased. Results from the constrained optimization supported this claim where it was seen that the takeoff efficiency was significantly lower than the climb and cruise efficiencies. Although the twist distributions obtained from the constrained optimization for each of the three operating conditions were significantly different, it was shown that the effect on performance was insignificant. This led to the conclusion that a variable twist propeller would not offer a noteworthy boost to performance and the concept would therefore not be beneficial for a typical aircraft mission.

Taking the unconstrained and constrained optimization results together, however, a mission profile where such a variable twist concept may be beneficial was presented. This mission profile consisted of extended loitering periods where the aircraft would be operating at a very low power setting in order to maximize endurance. But, mixed in with the loitering phases were high speed dash phases where the aircraft would operate at maximum speed. Such a mission profile was analyzed, and it was shown that a significant performance boost could be realized if a propeller had a variable twist capability. Specifically, it was shown that a propeller

optimized for loitering flight required 37 hp more to propel an aircraft to 300 kts than a propeller optimized for the high speed flight phase. Thus, if it were possible to morph a propeller into the optimum high speed shape, a power savings could be realized. On the other end of the spectrum it was shown that a dash optimized propeller required 11 hp more to operate in the loiter phase as compared to a loiter optimized propeller.

Although the optimization results by themselves seemed promising, the predicted power savings did not include the blade actuation cost. A thermal analysis was thus performed to determine the power needed to maintain the actuator material, Nickel-Titanium shape memory alloy, at a desired active temperature. The arrangement considered in the analysis was a shape memory alloy bonded to the lower airfoil surface but the airfoil geometry was simplified to that of a flat plate. A variety of atmospheric conditions were considered in the analysis and it was found that for all but extreme cold temperatures at sea level pressure the actuation cost would be less than the possible power savings. For a particular operating condition it was also shown that as long as an aircraft spent more than 63 % of the total flight time loitering, a fuel savings could be realized with a morphing propeller blade. This power requirement result along with the results from optimization showed that from the standpoint of performance a morphing propeller is indeed a viable concept.

The final consideration of this research was to look into the structural and actuation aspects of blade morphing. For this a literature survey was first performed to find a candidate smart material for actuation and also to review past work in the field of morphing structures. A number of possible concepts were identified as viable solutions for propeller blade morphing, and it was also concluded that shape memory alloys would be the best candidates for actuation material. Further study into a simple camber morphing concept was performed. The results

from a finite element analysis of a shape memory alloy strip bonded to a flat plate showed that the induced strain capability of shape memory alloys would be sufficient to provide the desired shape change. Published results of tension-torsion coupled structures were also studied to gauge the possibility of employing such a structure in a propeller blade. The analysis, however, showed the desired twist changes to be more than what would be possible for a tension-torsion coupled blade structure.

From all the aspects considered in this research, final conclusions as to the feasibility of morphing propeller blade can now be drawn. Firstly, from a structural and actuation point of view it was seen that shape memory alloys could provide the necessary displacements to achieve the desired shape change. Thus the technology is available in order for a morphing blade concept to work. The challenge in this regard will be to design a propeller blade to allow for shape changes while retaining thrust and centrifugal load carrying capability. From a performance standpoint, which was the main focus of this research, it is concluded that morphing propeller blades are viable. However, the operating profiles where such a propeller would offer a power reduction are limited to those such as a loiter-dash mission. Considering all the results together, it is therefore finally concluded from this research that morphing aircraft blades are indeed feasible.

6.2 Future Work

The research that has been performed has the potential for much future extension and development in a number of disciplines. In the area of optimization, a first step forward would be to apply calculus of variations to the problem of maximizing efficiency by varying the blade camber distribution. In so doing the optimum camber distribution would be obtained. A further extension could be to simultaneously optimize multiple design variables that could conceivably

be varied in flight using smart materials such as shape memory alloys. Further validation of the optimization results by fabricating and testing of fixed geometry propeller blades should also be performed in the future.

In the blade structure area much analysis work is needed in order to design a propeller blade structure that is compliant to the desired deformations yet stiff enough to support the operating loads. Part of the challenge would be the incorporation of shape memory alloys into the blade structure including wiring for electrical power supply. A defined internal blade structure will also allow for higher-order thermal analyses to improve the accuracy of the power requirement estimations.

Blade designs will also need to be constructed and tested in the future. At first the design, fabrication, and testing should focus on a blade airfoil section to validate designs in two-dimensions. Successful completion of this step would give much information and insight into designing an entire morphing propeller blade. Such a propeller would first have to be statically tested. Once a successful design is realized, testing of a full propeller with morphing capabilities on a ground-based test stand can be done.

Clearly there is much potential for future research stemming from this work. The ultimate goal of the continued research would be to see a variable geometry propeller flying on an aircraft in the future.

REFERENCES

REFERENCES

[1] Kinney, J. R., "Frank W. Caldwell and Variable Pitch Propeller Development, 1918-1938," *Journal of Aircraft*, Vol. 38, No. 5, 2001, pp. 967-976.

[2] Rankine, W. J. M., "The Mechanical Principles of the Action of Propellers," *Transactions of the Royal Institution of Naval Architects*, Vol. 6, 1865, pp. 13-30.

[3] Froude, R. E., "On the Part Played in Propulsion by Differences of Fluid Pressure," *Transactions of the Royal Institution of Naval Architects*, Vol. 30, 1889, pp. 390-405.

[4] Drzewiecki, S., "Des Hélices Propulsives," *Bulletin de l'Association Technique Maritime*, No. 11, 1900, pp. 89-116.

[5] Wald, Q. R., "The Wright Brothers Propeller Theory and Design," *37th AIAA/ASME/SAE/ASEE Joint Propulsion Conference & Exhibit*, AIAA paper 2001-3386, Salt Lake City, UT, 8-11 July, 2001.

[6] Wald, Q. R., "The Aerodynamics of Propellers," *Progress in Aerospace Sciences*, Vol. 42, No. 2, 2006, pp. 85-128.

[7] McCormick, B. W., *Aerodynamics, Aeronautics, and Flight Mechanics*, Wiley, New York, 1979.

[8] Whitmore, S. A. and Merrill, R. S., "Nonlinear Large Angle Solutions of the Blade Element Momentum Theory Propeller Equations," *Journal of Aircraft*, Vol. 49, No. 4, 2012, pp. 1126-1134.

[9] Phillips, W. F., "Propeller Momentum Theory with Slipstream Rotation," *Journal of Aircraft*, Vol. 39, No. 1, 2002, pp. 184-187.

[10] Gur, O. and Rosen, A., "Comparison Between Blade-Element Models of Propellers," *The Aeronautical Journal*, Vol. 112, No. 1138, 2008, pp. 689-704.

[11] Glauert, H., "Airplane Propellers," *Aerodynamic Theory*, edited by W. F. Durand, Vol. 4, Div. L, Springer, Berlin, 1935.

[12] Betz, A., "Schraubenpropeller mit Geringstem Energieverlust," *Nachrichten der Königlichen Gesellschaft der Wissenschaften zu Göttingen, Mathematisch-Physikalische Klasse*, Akademie der Wissenschaften in Göttingen, Göttingen, Germany, 1919, pp. 193-217.

[13] Prandtl, L. and Betz, A., *Vier Abhandlungen zur Hydrodynamik und Aerodynamik: (Flüssigkeit mit kleiner Reibung; Traflügeltheorie, I. und II. Mitteilung; Schraubenpropeller mit geringstem Energieverlust)*, Selbstverlag des Kaiser Wilhelm-Instituts für Strömungsforschung, Göttingen, Germany, 1927.

[14] Goldstein, S., "On the Vortex Theory of Screw Propellers," *Proceeding of the Royal Society London, Series A*, Vol. 123, No. 792, 1929, pp. 440-465.

[15] Lock, C. N. H., "The Application of Goldstein's Theory to the Practical Design of Airscrews," *Aeronautical Research Committee*, R&M No. 1377, London, November, 1930.

[16] Lock, C. N. H., Pankhurst, R. C. and Conn, J. F. C., "Strip Theory Method of Calculation for Airscrews on High-Speed Aeroplanes," *Aeronautical Research Committee*, R&M No. 2035, London, October, 1945.

[17] Theodorsen, T., "The Theory of Propellers. I: Determination of the Circulation Function and the Mass Coefficient for Dual-Rotating Propellers," NACA Report 775, 1944.

[18] Theodorsen, T., "The Theory of Propellers. II: Method for Calculating the Axial Interference Velocity," NACA Report 776, 1944.

[19] Theodorsen, T., "The Theory of Propellers. III: The Slipstream Contraction with Numerical Values for Two-Blade and Four-Blade Propelllers," NACA Report 777, 1944.

[20] Theodorsen, T., "The Theory of Propellers. IV: Thrust, Energy, and Efficiency Formulas for Single- and Dual-Rotating Propellers with Ideal Circulation Distribution," NACA Report 778, 1944.

[21] Theodorsen, T., *Theory of Propellers*, McGraw-Hill, New York, 1948.

[22] Crigler, J. L., "Application of Theodorsen's Theory to Propeller Design," NACA Report 924, 1949.

[23] Larrabee, E. E., "Practical Design of Minimum Induced Loss Propellers," *SAE Business Aircraft Meeting and Exposition*, SAE Technical Paper 790585, Wichita, KS, April, 1979.

[24] Adkins, C. N. and Liebeck, R. H., "Design of Optimal Propellers," *Journal of Propulsion and Power*, Vol. 10, No. 5, 1994, pp. 676-682.

[25] Hepperle, M., "Inverse Aerodynamic Design Procedure for Propellers Having a Prescribed Chord-Length Distribution," *Journal of Aircraft*, Vol. 47, No. 6, 2010, pp. 1867-1872.

[26] Runyan, H. L., "Unsteady Lifting Surface Theory Applied to a Propeller and Helicopter Rotor," Ph.D. Thesis, Department of Transport Technology, Loughborough University of Technology, Loughborough, UK, 1973.

[27] Hanson, D. B., "Compressible Helicoidal Surface Theory for Propeller Aerodynamics and Noise," *AIAA Journal*, Vol. 21, No. 6, 1983, pp. 881-889.

[28] Hanson, D. B., "Compressible Lifting Surface Theory for Propeller Performance Calculation," *Journal of Aircraft*, Vol. 22, No. 1, 1985, pp. 19-27.

[29] Schulten, J. B. H. M., "Advanced Propeller Performance Calculation by a Lifting Surface Method," *Journal of Propulsion and Power*, Vol. 12, No. 2, 1996, pp. 477-485.

[30] Burger, C., "Propeller Performance Analysis and Multidisciplinary Optimization Using a Genetic Algorithm," Ph.D. Dissertation, Department of Aerospace Engineering, Auburn University, Auburn, AL, 2007.

[31] Palmiter, S. M. and Katz, J., "Evaluation of a Potential Flow Model for Propeller and Wind Turbine Design," *Journal of Aircraft*, Vol. 47, No. 5, 2010, pp. 1739-1746.

[32] Foley, W. M., "From Da Vinci to the Present - A Review of Airscrew Theory for Helicopters, Propellers, Windmills, and Engines," *9th AIAA Fluid and Plasma Dynamics Conference*, AIAA paper 76-367, San Diego, CA, 14-16 July, 1976.

[33] Conlisk, A. T., "The Fluid Dynamics of Rotor Wakes: Theory, Computation and Experiment," *30th AIAA Fluid Dynamics Conference*, AIAA paper 99-3421, Norfolk, VA, 28 June - 1 July, 1999.

[34] Bober, L. J., Chaussee, D. S. and Kutler, P., "Prediction of High Speed Propeller Flow Fields Using a Three-Dimensional Euler Analysis," *21st AIAA Aerospace Sciences Meeting*, AIAA paper 83-0188, Reno, NV, 10-13 January, 1983.

[35] Bousquet, J. M. and Gardarein, P., "Recent Improvements in Propeller Aerodynamic Computations," *18th AIAA Applied Aerodynamics Conference*, AIAA paper 2000-4124, Denver, CO, 14-17 August, 2000.

[36] Roosenboom, E. W. M., Stürmer, A. and Schröder, A., "Advanced Experimental and Numerical Validation and Analysis of Propeller Slipstream Flows," *Journal of Aircraft*, Vol. 47, No. 1, 2010, pp. 284-291.

[37] Westmoreland, W. S., Tramel, R. W. and Barber, J., "Modeling Propeller Flow-Fields Using CFD," *46th AIAA Aerospace Sciences Meeting*, AIAA paper 2008-402, Reno, NV, 7-10 January, 2008.

[38] Steurmer, A. and Yin, J., "Low-Speed Aerodynamics and Aeroacoustics of CROR Propulsion System," *15th AIAA/CEAS Aeroacoustics Conference*, AIAA paper 2009-3134, Miami, FL, 11-13 May, 2009.

[39] Yin, J., Steurmer, A. and Aversano, M., "Coupled uRANS and FW-H Analysis of Installed Pusher Propeller Aircraft Configurations," *15th AIAA/CEAS Aeroacoustics Conference*, AIAA paper 2009-3332, Miami, FL, 11-13 May, 2009.

[40] Sodja, F., Stadler, D. and Kosel, T., "Computational Fluid Dynamics Analysis of an Optimized Load-Distribution Propeller," *Journal of Aircraft*, Vol. 49, No. 3, 2012, pp. 955-961.

[41] Nallasamy, M., Yamamoto, O., Warsi, S. and Bober, L. J., "Large-Scale Advanced Propeller Blade Pressure Distributions: Prediction and Data," *25th AIAA/ASME/SAE/ASEE Joint Propulsion Conference*, AIAA paper 89-2696, Monterey, CA, 10-12 July, 1989.

[42] Steinhoff, J. and Underhill, D., "Modifcation of the Euler Equations for "Vorticity Confinement:" Application to the Computations of Interacting Vortex Rings," *Physics of Fluids*, Vol. 6, No. 8, 1994, pp. 2738-2744.

[43] Wie, S. Y., Im, D. K., Kwon, J. H. and Lee, D. J., "Numerical Simulation of Rotor Using Coupled Computational Fluid Dynamics and Free Wake," *Journal of Aircraft*, Vol. 47, No. 4, 2010, pp. 1167-1177.

[44] Lock, C. N. H., Pankhurst, R. C. and Fowler, R. G., "Determination of the Optimum Twist of an Airscrew Blade by the Calculus of Variations," *Aeronautical Research Committee*, R&M No. 2088, London, January, 1942.

[45] Moriya, T., "Formulae for Propeller Characteristics Calculation and a Method to Obtain the Best Pitch Distribution," *Selected Scientific and Technical Papers*, Moriya Memorial Committee, Department of Aeronautics, Faculty of Engineering, University of Tokyo, Tokyo, Japan, 1959, pp. 43-47.

[46] Davidson, R. E., "Optimization and Performance Calculation of Dual-Rotation Propellers," NASA TP-1948, 1981.

[47] Shaw, R. L., "Computerized Aerodynamic Optimization of Aircraft Propellers," M.Sc. Thesis, Department of Aeronautical Engineering, Naval Postgraduate School, Moterey, CA, 1970.

[48] Mendoza, J. P., "Propeller Design by Numerical Optimization," *SAE Business Aircraft Meeting*, SAE Technical Paper 770451, Wichita, KS, 29 May - 1 April, 1977.

[49] Chang, L. K. and Sullivan, J. P., "Optimization of Propeller Blade Twist by an Analytical Method," *AIAA Journal*, Vol. 22, No. 2, 1984, pp. 252-255.

[50] Chang, L. K. and Stefko, G. L., "Application of an Optimization Method to High Performance Propeller Designs," *20th AIAA/SAE/ASME Joint Propulsion Conference*, AIAA paper 84-1203, Cincinnati, OH, 11-13 June, 1984.

[51] Cho, J. and Lee, S. C., "Propeller Blade Shape Optimization for Efficiency Improvement," *Computers & Fluids*, Vol. 27, No. 3, 1998, pp. 407-419.

[52] Rizk, M. H., "The Single-Cycle Scheme: A New Approach to Numerical Optimization," *AIAA Journal*, Vol. 21, No. 12, 1983, pp. 1640-1647.

[53] Rizk, M. H. and Jou, W. H., "Propeller Design by Optimization," *AIAA Journal*, Vol. 24, No. 9, 1986, pp. 1554-1556.

[54] Rizk, M. H., "Aerodynamic Optimization by Simultaneously Updating Flow Variables and Design Parameters with Application to Advanced Propellers," NASA CR-182181, 1988.

[55] Lee, J. and Hajela, P., "Parallel Genetic Algorithm Implementation in Multidisciplinary Rotor Blade Design," *Journal of Aircraft*, Vol. 33, No. 5, 1996, pp. 962-969.

[56] Burger, C., Hartfield, R. J. and Burkalter, J., "Propeller Performance Optimization using Vortex Lattice Method and Genetic Algorithm," *44th AIAA Aerospace Sciences Meeting and Exhibit*, AIAA paper 2006-1067, Reno, NV, 9-12 January, 2006.

[57] Gur, O. and Rosen, A., "Multidisciplinary Design Optimization of a Quiet Propeller," *14th AIAA/CEAS Aeroacoustics Conference*, AIAA paper 2008-3073, Vancouver, BC, 5-7 May, 2008.

[58] Gur, O. and Rosen, A., "Optimization of Propeller Based Propulsion System," *Journal of Aircraft*, Vol. 46, No. 1, 2009, pp. 95-106.

[59] Marinus, B. G., "Multidisciplinary Optimization of Aircraft Propeller Blades," Ph.D. Dissertation, Department of Mechnical Engineering, Royal Military Academy, von Karman Institute for Fluid Dynamics, and Ecole Centrale de Lyon, 2011.

[60] Farassat, F., "Derivation of Formulations 1 and 1A of Farassat," NASA TM-2007-214853, 2007.

[61] Marinus, B. G., Roger, M. and Van Den Braembussche, R., "Aeroacoustic and Aerodynamic Optimization of Aircraft Propeller Blades," *16th AIAA/CEAS Aeroacoustics Conference*, AIAA paper 2010-3850, Stockholm, Sweden, 7-9 June, 2010.

[62] Leo, D. J., *Engineering Analysis of Smart Material Systems*, Wiley, Hoboken, NJ, 2007.

[63] Giurgiutiu, V., "Actuators and Smart Structures," *Encyclopedia of Vibration*, edited by G. B. Simon, Elsevier, Oxford, 2001, pp. 58-81.

[64] Culshaw, B., *Smart Structures and Materials*, Artech House, Boston, 1996.

[65] Banks, H. T., Smith, R. C. and Wang, Y., *Smart Material Structures: Modeling, Estimation and Control*, Masson, Paris, 1996.

[66] Etrema Products Inc., "Terfenol-D Data Sheet." http://www.etrema-usa.com/documents/Terfenol.pdf (cited 8 October 2013)

[67] Hodgson, D. E., Wu, M. H. and Biermann, R. J., "Shape Memory Alloys," *ASM Handbook*,*Vol. 2*, *Properties and Selection: Nonferrous Alloys and Special-Purpose Materials*, ASM International, 1990, pp. 897-892.

[68] Madden, J. D., "Actuator Selection for Variable Camber Foils," Proceedings of SPIE, Vol. 5385,*Smart Structures and Materials 2004: Electroactive Polymer Actuators and Devices (EAPAD)*, San Diego, CA, 2004, pp. 442-448.

[69] Madden, J. D. W., Schmid, B., Hechinger, M., Lafontaine, S. R., Madden, P. G. A., Hover, F. S., Kimball, R. and Hunter, I. W., "Application of Polypyrrole Actuators: Feasibility of Variable Camber Foils," *IEEE Journal of Oceanic Engineering*, Vol. 29, No. 3, 2004, pp. 738-749.

[70] Miller, A. E. and Salisbury, H. M., "Variable Camber Propeller," US Patent 1,886,289, 1932.

[71] Medisch, J. C. and Wright, C. B., "Variable Camber Propeller Blade," US Patent 3,181,615, 1965.

[72] Rosen, G., "Variable Camber Blading," US Patent 2,982,361, 1961.

[73] Chen, P. C. and Chopra, I., "Hover Testing of Smart Rotor with Induced-Strain Actuation of Blade Twist," *AIAA Journal*, Vol. 35, No. 1, 1997, pp. 6-16.

[74] Rodgers, J. P., Hagood, N. W. and Weems, D. B., "Design and Manufacture of an Integral Twist-Actuated Rotor Blade," *38th AIAA/ASME/ASCE/AHS/ASC Structures, Structural Dynamics, and Materials Conference*, AIAA paper 97-1264, Kissimmee, FL, 7-10 April, 1997.

[75] Wilkie, W. K., Wilbur, M. L., Mirick, P. H., Cesnik, C. E. S. and Shin, S. J., "Aeroelastic Analysis of the NASA/ARMY/MIT Active Twist Rotor," *American Helicopter Society 55th Annual Forum*, Montreal, Canada, 25-27 May, 1999.

[76] Cesnik, C. E. S., Shin, S. J. and Wilbur, M. L., "Dynamic Response of Active Twist Rotor Blades," *Smart Materials and Structures*, Vol. 10, No. 1, 2001, pp. 62-76.

[77] Shin, S. J., Cesnik, C. E. S., Wilkie, W. K. and Wilbur, M. L., "Design and Manufacturing of a Model-scale Active Twist Rotor Prototype Blade," *Journal of Intelligent Material Systems and Structures*, Vol. 19, No. 12, 2008, pp. 1443-1456.

[78] Park, J. S., Kim, S. H., Jung, S. N. and Lee, M. K., "Design and Analysis of Variable-Twist Tiltrotor Blades Using Shape Memory Alloy Hybrid Composites," *Smart Materials and Structures*, Vol. 20, No. 1, Article 015001, 2011.

[79] Mistry, M., Gandhi, F., Nagelsmit, M. and Gurdal, Z., "Actuation Requirements of a Warp-Induced Variable Twist Rotor Blade," *Journal of Intelligent Material Systems and Structures*, Vol. 22, No. 9, 2011, pp. 919-933.

[80] Mistry, M., Gandhi, F. and Chandra, R., "Twist Control of an I-beam through Vlasov Bimoment Actuation," *49th AIAA/ASME/ASCE/AHS/ASC Structures, Structural Dynamics, and Materials Conference*, AIAA paper 2008-2278, Schaumburg, IL, 7-10 April, 2008.

[81] Ben-Zeev, O. and Chopra, I., "Advances in the Development of an Intelligent Helicopter Rotor Employing Smart Trailing-Edge Flaps," *Smart Materials and Structures*, Vol. 5, No. 1, 1996, pp. 11-25.

[82] Straub, F. K., "A Feasibility Study of Using Smart Materials for Rotor Control," *Smart Materials and Structures*, Vol. 5, No. 1, 1996, pp. 1-10.

[83] Straub, F. K., Kennedy, D. K., Domzalski, D. B., Hassan, A. A., Ngo, H., Anand, V. and Birchette, T., "Smart Material-Actuated Rotor Technology – SMART," *Journal of Intelligent Material Systems and Structures*. Vol. 15, 2004, pp. 249-260.

[84] Woods, B. K. S., Kothera, C. S. and Wereley, N. M., "Wind Tunnel Testing of a Helicopter Rotor Trailing Edge Flap Actuated via Pneumatic Artificial Muscles," *Journal of Intelligent Material Systems and Structures*, Vol. 22, No. 13, 2011, pp. 1513-1528.

[85] Bernhard, A. P. F. and Chopra, I., "Hover Testing of Active Rotor Blade-Tips Using a Piezo-Induced Bending-Torsion Coupled Beam," *Journal of Intelligent Material Systems and Structures*, Vol. 9, No. 12, 1998, pp. 963-974.

[86] Chandra, R., "Active Shape Control of Composite Blades Using Shape Memory Actuation," *Smart Materials and Structures*, Vol. 10, No. 5, 2001, pp. 1018-1024.

[87] Amprikidis, M. and Cooper, J. E., "Development of Smart Spars for Active Aeroelastic Structures," *44th AIAA/ASME/ASCE/AHS Structures, Structural Dynamics, and MAterials Conference*, AIAA paper 2003-1799, Norfolk, VA, 7-10 April, 2003.

[88] Cooper, J. E., "Adaptive Stiffness Structures for Air Vehicle Drag Reduction," *NATO Science and Technology Organization Specialists' Meeting on Multifunctional Structures/ Integration of Sensors and Antennas*, RTO-MP-AVT-141 paper 15, Vilnius, Lithuania, 2-4 October, 2006.

[89] Ott, E. A., "Shape Changing Airfoil," NASA CR-2005-213971, 2005.

[90] Bilgen, O., Kochersberger, K. B., Inman, D. J. and Ohanian, O. J., III, "Macro-Fiber Composite Actuated Simply Supported Thin Airfoils," *Smart Materials and Structures*, Vol. 19, No. 5, Article 055010, 2010.

[91] Beauchamp, C. H. and Nedderman, W. H., Jr., "Controllable Camber Windmill Blades," US Patent 6,465,902 B1, 2002.

[92] Büter, A., Ehlert, U. C., Sachau, D. and Breitbach, E., "Adaptive Rotor Concepts - Direct Twist and Camber Variation," *Active Control Technology for Enhanced Performance Operational Capabilities of Military Aircraft, Land Vehicles and Sea Vehicles*, Braunschweig, Germany, 8-11 May, 2000.

[93] Strelec, J. K., Lagoudas, D. C., Khan, M. A. and Yen, J., "Design and Implementation of a Shape Memory Alloy Actuated Reconfigurable Airfoil," *Journal of Intelligent Material Systems and Structures*, Vol. 14, No. 4-5, 2003, pp. 257-273.

[94] Bil, C., Massey, K. and Abdullah, E. J., "Wing Morphing Control with Shape Memory Alloy Actuators," *Journal of Intelligent Material Systems and Structures*, Vol. 24, No. 7, 2013, pp. 879-898.

[95] Monner, H. P., Sachau, D. and Breitbach, E., "Design Aspects of the Elastic Trailing Edge for an Adaptive Wing," *NATO Research and Technology Organization Specialists' Meeting on Structural Aspects of Flexible Aircraft Control*, RTO-MP-36, Ottawa, Canada, 18-20 October, 1999.

[96] Poonsong, P., "Design and Analysis of Multi-Section Variable Camber Wing," M.Sc. Thesis, Department of Aerospace Engineering, University of Maryland, College Park, MD, 2004.

[97] Barbarino, S., Pecora, R., Lecce, L., Concilio, A., Ameduri, S. and Calvi, E., "A Novel SMA-based Concept for Airfoil Structural Morphing," *Journal of Materials Engineering and Performance*, Vol. 18, No. 5-6, 2009, pp. 696-705.

[98] Pecora, R., Barbarino, S., Concilio, A., Lecce, L. and Russo, S., "Design and Functional Test of a Morphing High-Lift Device for a Regional Aircraft," *Journal of Intelligent Material Systems and Structures*, Vol. 22, No. 10, 2011, pp. 1005-1023.

[99] Wang, Q., Xu, Z. and Zhu, Q., "Structural Design of Morphing Trailing Edge Actuated by SMA," *Frontiers of Mechanical Engineering*, Vol. 8, No. 3, 2013, pp. 268-275.

[100] Parker, H. F., "The Parker Variable Camber Wing," NACA Report No. 77, 1920.

[101] Baker, D. and Friswell, M. I., "Determinate Structures for Wing Camber Control," *Smart Materials and Structures*, Vol. 18, No. 3, Article 035014, 2009.

[102] Barbarino, S., Dettmer, W. G. and Friswell, M. I., "Morphing Trailing Edges with Shape Memory Alloy Rods," *21st International Conference on Adaptive Structures and Technologies*, University Park, PA, 4-6 October, 2010.

[103] Gandhi, F., Frecker, M. and Nissly, A., "Design Optimization of a Controllable Camber Rotor Airfoil," *AIAA Journal*, Vol. 46, No. 1, 2008, pp. 142-153.

[104] Campanile, L. F. and Sachau, D., "The Belt-Rib Concept: A Structronic Approach to Variable Camber," *Journal of Intelligent Material Systems and Structures*, Vol. 11, No. 3, 2000, pp. 215-224.

[105] Previtali, F. and Ermanni, P., "Performance of a Non-Tapered 3D Morphing Wing with Integrated Compliant Ribs," *Smart Materials and Structures*, Vol. 21, No. 5, Article 055008, 2012.

[106] Spadoni, A. and Ruzzene, M., "Numerical and Experimental Analysis of the Static Compliance of Chiral Truss-Core Airfoils," *Journal of Mechanics of Materials and Structures*, Vol. 2, No. 5, 2007, pp. 965-981.

[107] Spadoni, A. and Ruzzene, M., "Static Aeroelastic Response of Chiral-Core Airfoils," *Journal of Intelligent Material Systems and Structures*, Vol. 18, No. 10, 2007, pp. 1067-1075.

[108] Airoldi, A., Crespi, M., Quaranta, G. and Sala, G., "Design of a Morphing Airfoil with Composite Chiral Structure," *Journal of Aircraft*, Vol. 49, No. 4, 2012, pp. 1008-1019.

[109] Abbott, I. H. and von Doenhoff, A. E., *Theory of Wing Sections*, Dover Publications Inc., New York, 1959.

[110] Drela, M., "XFOIL: An Analysis and Design System for Low Reynolds Number Airfoils," *Lecture Notes in Engineering*, *Low Reynolds Number Aerodynamics*, edited by T. J. Mueller, Vol. 54, Springer Berlin Heidelberg, 1989, pp. 1-12.

[111] Sheldahl, R. E. and Klimas, P. C., "Aerodynamic Characteristics of Seven Symmetrical Airfoil Sections Through 180-Degree Angle of Attack for Use in Aerodynamic Analysis of Vertical Axis Wind Turbines," *Sandia National Laboratories*, SAND80-2114, March, 1981.

[112] Timmer, W. A., "Aerodynamic Characteristics of Wind Turbine Blade Airfoils at High Angles-of-Attack," *TORQUE 2010: The Science of Making Torque from Wind*, Crete, Greece, 20-30 June, 2010.

[113] Stivers, L. S., "Effects of Subsonic Mach Number on the Forces and Pressure Distributions on Four NACA 64A-Series Airfoil Sections at Angles of Attack as High as 28°," NACA TN-3162, 1954.

[114] Ladson, C. L., "Two-Dimensional Airfoil Characteristics of Four NACA 6A-Series Airfoils at Transonic Mach Numbers up to 1.25," NACA RM-L57F05, 1957.

[115] Daley, B. N. and Dick, R. S., "Effect of Thickness, Camber, and Thickness Distribution on Airfoil Charateristics at Mach Number up to 1.0," NACA TN-3607, 1958.

[116] Harris, C. D., "Two-dimensional aerodynamic characteristics of the NACA 0012 airfoil in the Langley 8-foot transonic pressure tunnel," NASA TM-81927, 1981.

[117] Boppe, C. W., "CFD Drag Prediction for Aerodynamic Design," *AGARD Fluid Dynamics Panel Technical Status Review on Drag Prediction and Analysis from Computational Fluid Dynamics: State of the Art*, Lisbon, Portugal, 5 May, 1988.

[118] Mason, W. H., "Chapter 7: Transonic Aerodynamics of Airfoils and Wings," *Configuration Aerodynamics*, Virginia Tech, Blacksburg, VA, 2006. http://www.dept.aoe.vt.edu/~mason/Mason_f/ConfigAero.html (cited 27 March 2014)

[119] Hoerner, S. F., *Fluid-Dynamic Drag*, 1958.

[120] D'Angelo, S., Berardi, F. and Minisci, E., "Aerodynamic Performances of Propellers with Parametric Considerations on the Optimal Design," *The Aeronautical Journal*, Vol. 106, No. 1060, 2002, pp. 313-320.

[121] Kaplan, C., "Effect of Compressibility at High Subsonic Velocities on the Lifting Force Acting on an Elliptic Cylinder," NACA TN-1118, 1946.

[122] Maynard, J. D. and Salters, L. B., Jr., "Aerodynamic Characteristics at High Speeds of Related Full-Scale Propellers Having DIfferent Blade-Section Cambers," NACA TR-1309, 1957.

[123] Evans, A. J. and Liner, G., "A Wind-Tunnel Investigation of the Aerodynamic Characteristics of a Full-Scale Supersonic-Type Three-Blade Propeller at Mach Number to 0.96," NACA TR-1375, 1958.

[124] Lindsey, W. F., Stevenson, D. B. and Daley, B. N., "Aerodynamic Characteristics of 24 NACA 16-Series Airfoils at Mach Numbers Between 0.3 and 0.8," NACA TN-1546, 1948.

[125] Stack, J., "Tests of Airfoils Designed to Delay the Compressibility Burble," NACA Report 763, 1943.

[126] Komzsik, L., *Applied Calculus of Variations for Engineers*, CRC Press, Boca Raton, 2009.

[127] Schechter, R. S., *The Variational Method in Engineering*, McGraw-Hill, New York, 1967.

[128] Pankhurst, R. C. and Fowler, R. G., "Calculations of the Performance of Two Airscrews for a High-speed Aeroplane," *Aeronautical Research Committee*, R&M No. 2021, London, April, 1941.

[129] Haines, A. B. and Monaghan, B. A., "High-speed Lift and Drag Data for Propeller Performance Calculations," *Aeronautical Research Committee*, R&M No. 2036, London, November, 1945.

[130] Pankhurst, R. C. and Haines, A. B., "Account of the Derivation of High-Speed Lift and Drag Data for Propeller Blade Sections," *Aeronautical Research Committee*, R&M No. 2020, London, August, 1945.

[131] Dorfling, J., "Flight Environment of the Propellers on Commuter Aircraft," M.Sc. Thesis, Department of Aerospace Engineering, Wichita State University, Wichita, KS, 2008.

[132] *TBM 850 Pilot's Information Manual*, Daher-Socata, 2012.

[133] Kuethe, A. M. and Chow, C. Y., *Foundations of Aerodynamics*, John Wiley & Sons, New York, 1986.

[134] Timoshenko, S., "Analysis of Bi-Metal Thermostats," *Journal of the Optical Society of America*, Vol. 11, No. 3, 1925, pp. 233-255.

[135] Newton, J. E., VanFossen, G. J., Poinsatte, P. E. and DeWitt, K. J., "Measurement of Local Heat Transfer Coefficients from a Smooth and Roughened NACA-0012 Airfoil: Flight Test Data," *26th AIAA Aerospace Sciences Meeting*, AIAA paper 88-0287, Reno, NV, 11-14 January, 1988, 1988.

[136] Wang, X., Naterer, G. F. and Bibeau, E., "Convective Heat Transfer from a NACA Airfoil at Varying Angles of Attack," *Journal of Thermophysics and Heat Transfer*, Vol. 22, No. 3, 2008, pp. 457-463.

[137] Incropera, F. P. and DeWitt, D. P., *Fundamentals of Heat and Mass Transfer*, 5th ed., John Wiley & Sons, 2002.

[138] Du Pont USA, "Technical Guide - Kevlar Aramid Fiber." www2.dupont.com/Kevlar/en.../KEVLAR_Technical_Guide.pdf (cited 27 May 2014)

[139] *Jane's Aero-Engines*, edited by B. Gunston, Jane's Information Group, Alexandria, VA, 1996.